UNIVERSITÀ DEGLI STUDI DI NAPOLI "FEDERICO II"

SCUOLA POLITECNICA E DELLE SCIENZE DI BASE

Dipartimento Di Ingegneria Chimica, Dei Materiali E Della Produzione Industriale

Ph.D. course in

Industrial Product and Process Engineering

Ph.D. thesis

Understanding the mechanisms of crossing delivery and targeting of nanostructures for brain theranostics

Coordinator:

Prof. Andrea D'Anna

Supervisors:

Prof. Enza Torino

Prof. Paolo Antonio Netti

Candidate:

Angela Costagliola di Polidoro

Table of contents

BACKGROUND AIM OF THE WORK AND MAJOR FINDINGS

The term "Nanomedicine" firstly appeared in the late 1970s and since 2005 it has been formally defined as the "*use of nano-sized tools for the diagnosis, prevention and treatment of disease and to gain increased understanding of the complex underlying patho-physiology of disease*" in the European Science Fundation (ESF)'s forward Look Nanomedicine[1]. Since that time extensive research has demonstrated that nanomedicines possess huge potentialities in improving the pharmacokinetics and enhancing the efficacy of many active agents with a direct impact on patients' quality of life[2,3].

Nanoparticles are extremely versatile platforms with several advantages over traditional medicines. They enable stable aqueous dispersions of active, but poorly water-soluble molecular agents, for delivery in the biological milieu. Different active agents can be incorporated within their bulk and/or pore network or can be attached to their surface. Their composition, size, shape, and surface properties can be exquisitely tailored so that they can protect the encapsulated agents from degradation, exhibiting no toxicity and being safely excreted from the body[4-6]. All these features contribute to define the *synthetic identity* of a carrier which is responsible for its functionalities. The proper selection of the nanoparticle synthetic identity makes the nanomedicine suitable for the most diverse applications moving from multimodal imaging to theranostics. However, the synthetic identity alone is not enough to assess how effectively the carrier will exploit these features in the biological environment and more in general *in vivo*. Indeed, every synthetic identity translates in a biological identity that establishes a unique structure-activity relation, determining the way the nanocarrier will interact with its target, exploiting its function. Every biological identity gives rise to specific nanotechnology-biology (*i.e.*, nano-bio) interactions that when not properly tackled may affect the effectiveness of the formulation regardless its diagnostic and therapeutic potential[7].

Decades of research produced a striking number of *in-vitro a*nd preclinically successful formulations exploring the most diverse nanoparticle designs leading to very different synthetic identities that contributed to introducing a significant scientific and technological advancement in nano-biomaterials production, characterization and pharmacokinetics[8-10].

In addition, many studies revealed that the fine tuning of nanoparticle properties can lead to the enhancement of the intrinsic properties of the active agents themselves elevating the nanoparticle from a carrier deputed to control the active agent delivery and biodistribution to an active participant to the diagnostic or therapeutic function of a probe with enhanced properties. As an example, Russo et al.[11-13], demonstrated that hydrogel matrices and in particular crosslinked hyaluronic acid nanoparticles (cHANPs), are able to boost the relaxometric properties of Gd-DTPA, one of the most common clinical contrast agent for MRI, up to 12 fold in a crosslinking-dependent manner through the effect of Hydrodenticity.

Differently, still few is known about how the well-understood synthetic identity of nanoparticles connects with its biological counterpart[14,15]. Indeed, the poor understanding of the mechanisms underlying the interaction that nanomaterials have with the biological environment is considered one the most important cause of poor nanoparticle clinical translation, with numerous publications that translate in few formulations entering the clinical trials and even fewer reaching the clinics[16]. This reveals that a much deeper comprehension of the biological fingerprint of nanocarriers is necessary in order to reduce the gap between the bench discoveries and their clinical success. In the recent literature nano-bio-interactions have been investigated at different levels: nanoparticle' stability in systemic circulation and protein corona[15,17-24], tissue permeability and diffusion[25-27], cell-nanomaterial interface and uptake mechanism and kinetic[28-35]. Each level has been investigated at different grades of detail and through models of carriers and biological environment of varying complexity.

The first level regards nanoparticle stability in the systemic circulation and protein corona formation, a field that has been extensively explored in the last ten years. Protein corona forms as NPs enter the systemic circulation where they are immediately exposed to high protein concentrations (60–80 g/L)[36] that cause the adsorption of proteins on the surface of the particle altering their colloidal stability and identity. The formation of protein corona has been referred as a dynamic process, with a material-dependent kinetic involving protein-protein interactions and thus it can be directly impacted by the NP synthetic identity[23,24].

The protein adsorption to the NP surface was long considered a detrimental phenomenon, leading to unwanted effects, such as particle early clearence, macrophages capture, off-target effects, and loss of specificity. For this reason, the scientific community aimed for long time to develop adsorption-resistant nanoparticles, covering their surface with specific materials such as polyethylene glycol (PEG)[18,37-40]. More recently, however, emerging evidences show how the NP surface functionalization triggering the absorption of some specific proteins might instead enhance the targeting ability of some formulations[22].

Nevertheless, the majority of the studies aiming to understand the formation and the kinetic of the protein corona involve standard nanoparticle models: polystyrene NPs, metal and particularly gold NPs[14], and inorganic as silica NPs[14]. The underlying reasons are easiness of production in a homogeneous fashion, well characterized physical-chemical properties and easy measurements and characterization of aggregation and corona composition. However, the relevance of these NP models in a clinical environment is still unclear since they have demonstrated prolonged circulation times, long-term accumulation in off-target organs and acute toxicity[41].

Interaction with the target tissue represents the second level of investigation of the impact that NP synthetic identity has on the in-vivo fate of NPs and in particular, on their targeting ability.

In this regard, Wilhelm et al.[4] collected and compared more than 200 studies about preclinical testing of NPs for treatment and diagnosis of solid tumours revealing the impact that each NP characteristic (composition, size, shape, surface charge and surface functionalization) has on the delivery efficiency of the formulation

defined as the percentage of the dose that accumulates in the target site with respect to the administered one. Interestingly, results showed that from 2005 to 2015 no improvements in the average delivery efficiency of both organic and inorganic formulations have been achieved, revealing a urgent need in deepening the understanding of the in-vivo biological identity of NPs, regardless the development of NPs with a more efficient synthetic identity. Secondly, the study demonstrated that each NP characteristic on the basis of the organic or inorganic nature of the formulation, influences its delivery efficiency at a different extent. This latter observation highlights how results obtained for a specific nanoparticle synthetic identity cannot be translated to other systems and thus how crucial the use of clinically relevant NP models in the study of nano-bio-interactions are in view of improving the clinical success of NPs.

Ideally, after reaching the systemic circulation, NPs should interact selectively with their specific target tissue guaranteeing a preferential accumulation triggered both by specific surface functionalization and in some cases increased tissue permeability (i.e. cancer)[42].

Extravasation and tissue targeting involve the crossing of the vessel endothelial layer and the diffusion through the tissue extracellular space (ECS). The crossing of the endothelial layer can occur passively, through simple membrane diffusion or inter-endothelial junctions and actively through receptor mediated transport, which allow molecule transfer from the lumen to the ablumen. Both transport routes strongly depend on the dimension, shape, surface charge and functionalization of the nanoparticle when it arrives at the endothelium. However, these characteristics may differ strongly from the designed one as the absorption of plasma protein at the surface of the particles contribute to modify them, and the acquired biological identity may hinder the intended transport contributing to decrease the delivery efficiency of the formulation.

Rakesh Jain, in 1987[43], formulated the overall flux across the tumour vasculature as the sum of the diffusive solute flux (J_s) and the net fluid flow at transcapillary wall (J_f):

$$J_s = PA(c_v - c_i)$$

where P represents the diffusive permeability in $\frac{cm}{s}$, A is the surface area in cm^2, $c_v \; and \; c_i$ the plasma and interstitial concentration of the solute in $\frac{g}{cm^3}$ respectively.

And,

$$J_f = L_p A[(p_v - p_i) - \sigma(\pi_v - \pi_i)]$$

where L_p represents the hydraulic conductivity in $\frac{cm}{s \cdot dyn}^3$, A is the surface area in cm^2, $p_v \; and \; p_i$ represents the hydraulic conductivity at the vascular and interstitial side in $\frac{dyn}{cm^2}$ respectively and $\pi_v \; and \; \pi_i$ the colloid vascular and interstitial osmotic pressure in $\frac{dyn}{cm^2}$.

After extravasation, to reach target cells NPs should diffuse deeply in the tissue and the extent of diffusion will depend on two main separate but linked factors: the diffusion coefficient of the formulation and tissue permeability.

Overall tissue permeability can be associated to a membrane permeability and defined as:

$$P = \frac{kD_{eff}}{\Delta x}$$

where k is the tissue partition coefficient, $D_{eff}$the effective diffusion coefficient of the formulation in the extracellular space (ECS) and Δx is the travelled length. Indeed, in order to predict the distribution of a substance in a complex tissue it is essential to know its effective diffusion coefficient in tissue as well as the relative importance of diffusion versus clearance processes that may remove that substance from the tissue. This means that nanoparticle diffusion coefficient in free medium should be corrected accounting for tissue anatomical composition by means of parameters such as ECS fraction volume α and tissue tortuosity λ which will account both for geometrical factors (λ_g) and other features of the internal milieu of the ECS[44].

These considerations highlight that in addition to NPs biological identity, the anatomy and physical characteristics of the tumour microenvironment play a fundamental role in determining NP transport properties in these environments. In preclinical settings, these features are strongly dependent on tumour implantation methodology, implantation site, developmental stage and if it is an orthotopic or xenograft model[45]. For this reason, the study of nanoparticle delivery efficiency and targeting ability has necessarily to rely on both well- defined NP biological identity and accurately selected tumour models.

The third level of nano-bio-interaction investigation is the cell-NP interface. Cell membrane is constituted by a phospholipid-based bilayer with transmembrane proteins and biomolecules resulting in an overall negative charge with few cationic domains and selective permeability to ions, biomolecules and NPs. NPs are internalized by cells through many different and highly regulated mechanisms. These mechanisms can be grouped in two main categories: direct NP internalization and endocytosis-based internalization[29]. Regarding direct cytoplasmic translocation of NPs, it is a route that has been widely explored for inorganic NPs (quantum dots, gold NPs) that have demonstrated the ability to diffuse directly through cell membrane when they have a maximum dimeter of 8 nm[28,46]. Another possibility is direct fusion of NPs with cell membrane, mechanism mainly demonstrated for lipid-based carrier as liposomes or natural vesicles as exosomes[47]. Finally, the use of cell-penetrating peptides (CPP) with a sequence of few up to 40 amino acids, has been demonstrated to allow direct access to cytoplasm to functionalized NPs with a still poorly clear mechanism. Examples of most commonly employed CPP are TAT, penatratin, arginine-rich sequences, TP10, pVEC, and MPG[48].

Endocytosis-based internalization is a much broader category, involving both passive and energy-dependent receptor mediated internalization mechanisms named clathrin-dependent and caveolin-dependent

endocytosis, clathrin- and caveolin-independent endocytosis, phagocytosis, and macropinocytosis. They involve the formation of intracellular vesicles such as endosomes, phagosomes, or macropinosomes, and therefore do not allow direct access to cell cytoplasm.

Endocytosis is the result of a complex balance of forces acting locally at the cell membrane which involves specific and unspecific interactions as demonstrated by Decuzzi and Ferrari[49]. These forces are both adhesive contributing to reduce the free-energy as ligand-receptor binding and attractive non-specific electrostatic forces, and resistive as bending of the cell membrane in a shape to accommodate the NP, diffusion of the receptors over the cell membrane and thermal fluctuations. They demonstrated that the extent of these forces depends on nanoparticle size, surface charge and ligand surface density and that it is possible to define a threshold size for endocytosis to occur as well as an optimal size range[49].

Regarding NP surface charge, it has been additionally proven that being the cell membrane negatively charged, positively charged NPs show strongly increased uptake compared with their negatively charged counterparts in different cancer cell types[50]. This observation has led to innovative 'charge-conversion' strategies as the use of zwitterionic compounds[51]. Zwitterions consist of equimolar cationic and ionic moieties resulting in an overall neutral charge. When in blood-circulation at the physiological pH of 7.4 zwitterions possess strong anti-adsorbing properties due to their hydrophilicity exerted by a strong dipole-ion interaction. When exposed at lower pH values of ~6.8 (typical of tumor microenvironment) or 5 to 5.5 (typical of endosomes), the anionic component of the surface is shed, leaving a positive surface charge on nanoparticles facilitating increased and site specific tumor cell entry or faster cargo release[52].

Despite the numerous studies attempting at the determination of NP internalization mechanism as consequence of different NP designs, the major challenge that the scientific community is currently facing is the standardization of the protocols applied for the study of cellular uptake of NPs. These protocols often involve the use of fluorescent NPs incubated with cells pre-treated with inhibitors to hinder specific internalization mechanisms, with flow cytometry and optical imaging being the most used methodology for particle uptake quantification and cellular localization. In this regard Francia et al.[53,54], demonstrated with a comprehensive study on HeLa cells how the use of specific inhibitors without appropriate controls and controlled serum conditions can introduce significant artifacts in particle uptake studies inducing changes in cellular physiology and toxicity. In addition, the same group highlighted the need for stable fluorescent labelling of NPs since free dye, being a fast-diffusing molecule, can significantly alter results about uptake kinetic. Furthermore, they highlighted through an interlaboratory study about flow cytometry measurement for particle uptake quantification, the necessity for standardized sample preparation protocols, unified measurement, analysis and interpretation of obtained results[33].

Overall, the presented review of the state of the art in the study of nano-bio-interactions revealed that the scientific community is still in an embryonal stage of comprehension of the mechanisms involved in the interaction of nanomaterial with the biological environment at all different levels, with most of the studies

involving scarcely reliable NPs and biological models. This translates directly in the development of poorly effective nanoformulations and consequently in their poor clinical translation. In this framework, my thesis work aimed to the study, characterization, and deep understanding of the connection existing between the synthetic and biological identity of Hyaluronic Acid (HA) - based NPs, as a clinically relevant NP model. Starting from a patented, microfluidic-based nanoprecipitation process to produce crosslinked Hyaluronic Acid Nanoparticles (cHANPs), a library of HA-based nanovectors with different synthetic identities was produced with a tight control over production process leading to highly homogeneous population of NPs with well-defined features. The choice of HA at different MW, the introduction of another polymer (polyethylene glycol – PEG) and the encapsulation of different active agents allowed to characterize the impact that these variables have on the thermodynamic of the processes of nucleation and growth, the crosslinking of the hydrogel matrix and encapsulation efficiencies, as presented in our work "*A Microfluidic Platform to design Multimodal PEG - crosslinked Hyaluronic Acid Nanoparticles (PEG-cHANPs) for diagnostic applications*" [55]. Secondly, the biological identity of these nanovectors was investigated in different biological sera assessing their colloidal stability, their antifouling ability and changes in surface properties due to protein absorption, as well as the impact that these changes have on the uptake and the uptake kinetic of NPs by cells. In addition, the ability of cHANPs of preserving structural stability was confirmed in an extremely complex biological environment, such as human atherosclerotic plaques (AP). After a specific surface functionalization (Ab-cHANPs), the ability of Ab-cHANPs in preserving the Hydrodenticity effect upon injection in this human complex tissue was assessed in a clinical 1.5 T MRI as described in our work "Targeting Nanostrategies for Imaging of Atherosclerosis" [57]. Furthermore, the impact that different NPs synthetic identity has on the diffusion in three-dimensional complex tissues was studied. The over-time diffusion of cHANPs was studied in Hep-G2 microtissues as a reliable model of liver tissue, recapitulating cell to cell connections, internalization mechanisms and tissue extracellular space[58]. cHANPs diffusion was compared to the diffusion of natural vesicles and complex hybrid lipid-polymer structures and the differences in the interaction that these different NPs has with the microtissues were highlighted. The study was performed in absence of serum to study directly the impact of the different NP synthetic identity on the interaction with the microtissue and the diffusion process. The acquired knowledge about nano-bio-interactions arising between hydrogel-based nanoparticles and the biological environment at different levels was applied to demonstrate the potential of the developed strategy in guiding the rational design of nanovectors for overcoming disease-specific biological barriers. Glioblastoma Multiforme was chosen as a case study, disease-specific biological barriers were identified and the potentialities of specifically designed theranostic cHANPs (Thera-ANG-cHANPs) to overcome these biological barriers, preserving the Hydrodenticity effect, and keeping unmodified their functionality, were assessed as presented in our publication *"Theranostic design of Angiopep-2 conjugated Hyaluronic Acid Nanoparticles (Thera-ANG-cHANPs) for dual targeting and boosted imaging of glioma cells"* [56]. Preliminary in-vivo studies were conducted for the setting up of a suitable protocol for nanoparticle testing

and preliminary assess nanoparticle biodistribution. As a final aim, the potential of pharmacokinetic modelling based on clinical data in investigating the role of nanoparticles in mediating nano-bio-interactions of active agents with the biological environment at different levels is unravelled.

References

1 Briefing, E. S. F. P. (2005).

2 Astruc, D. Introduction to Nanomedicine. *Molecules* **21**, doi:10.3390/molecules21010004 (2016).

3 Soares, S., Sousa, J., Pais, A. & Vitorino, C. Nanomedicine: Principles, Properties, and Regulatory Issues. *Frontiers in Chemistry* **6**, doi:10.3389/fchem.2018.00360 (2018).

4 Wilhelm, S. *et al.* Analysis of nanoparticle delivery to tumours. *Nature Reviews Materials* **1**, doi:10.1038/natrevmats.2016.14 (2016).

5 Kim, B. Y. S., Rutka, J. T. & Chan, W. C. W. Current Concepts: Nanomedicine. *New England Journal of Medicine* **363**, 2434-2443, doi:10.1056/NEJMra0912273 (2010).

6 Sindhwani, S. *et al.* The entry of nanoparticles into solid tumours. *Nature Materials*, doi:10.1038/s41563-019-0566-2.

7 Lazarovits, J., Chen, Y. Y., Sykes, E. A. & Chan, W. C. W. Nanoparticle-blood interactions: the implications on solid tumour targeting. *Chemical Communications* **51**, 2756-2767, doi:10.1039/c4cc07644c (2015).

8 Ma, Y. F., Huang, J., Song, S. J., Chen, H. B. & Zhang, Z. J. Cancer-Targeted Nanotheranostics: Recent Advances and Perspectives. *Small* **12**, 4936-4954, doi:10.1002/smll.201600635 (2016).

9 Li, X., Zhang, X. N., Li, X. D. & Chang, J. Multimodality imaging in nanomedicine and nanotheranostics. *Cancer Biology & Medicine* **13**, 339-348, doi:10.20892/j.issn.2095-3941.2016.0055 (2016).

10 Sonali. Vol. 2 (eds Rahul Pratap Singh Matte Kasi Viswanadh , Poornima Agrawal , Abhishesh Kumar Mehata , Datta Maroti Pawde , & and Madaswamy Sona Muthu Roshan Sonkar) 70-86 (Nanotheranostics, 2018).

11 Russo, M., Ponsiglione, A. M., Forte, E., Netti, P. A. & Torino, E. Hydrodenticity to enhance relaxivity of gadolinium-DTPA within crosslinked hyaluronic acid nanoparticles. *Nanomedicine* **12**, 2199-2210, doi:10.2217/nnm-2017-0098 (2017).

12 Russo, M., Bevilacqua, P., Netti, P. A. & Torino, E. A Microfluidic Platform to design crosslinked Hyaluronic Acid Nanoparticles (cHANPs) for enhanced MRI. *Scientific Reports* **6**, doi:10.1038/srep37906 (2016).

13 De Sarno, F. *et al.* Water-Mediated Nanostructures for Enhanced MRI: Impact of Water Dynamics on Relaxometric Properties of Gd-DTPA. *Theranostics* **9**, 1809-1824, doi:10.7150/thno.27313 (2019).

14 Boselli, L. *et al.* Classification and biological identity of complex nano shapes. *Communications Materials* **1**, doi:10.1038/s43246-020-0033-2 (2020).

15 Nguyen, V. H. & Lee, B. J. Protein corona: a new approach for nanomedicine design. *International Journal of Nanomedicine* **12**, 3137-3151, doi:10.2147/ijn.s129300 (2017).

16 Metselaar, J. M. & Lammers, T. Challenges in nanomedicine clinical translation. *Drug Delivery and Translational Research* **10**, 721-725, doi:10.1007/s13346-020-00740-5 (2020).

17 Tekie, F. S. M. *et al.* Controlling evolution of protein corona: a prosperous approach to improve chitosan-based nanoparticle biodistribution and half-life. *Scientific Reports* **10**, doi:10.1038/s41598-020-66572-y (2020).
18 Pozzi, D. *et al.* Effect of polyethyleneglycol (PEG) chain length on the bio-nano-interactions between PEGylated lipid nanoparticles and biological fluids: from nanostructure to uptake in cancer cells. *Nanoscale* **6**, 2782-2792, doi:10.1039/c3nr05559k (2014).
19 Almalik, A. *et al.* Hyaluronic Acid Coated Chitosan Nanoparticles Reduced the Immunogenicity of the Formed Protein Corona. *Scientific Reports* **7**, doi:10.1038/s41598-017-10836-7 (2017).
20 Bertrand, N. *et al.* Mechanistic understanding of in vivo protein corona formation on polymeric nanoparticles and impact on pharmacokinetics. *Nature Communications* **8**, doi:10.1038/s41467-017-00600-w (2017).
21 Shreffler, J. W., Pullan, J. E., Dailey, K. M., Mallik, S. & Brooks, A. E. Overcoming Hurdles in Nanoparticle Clinical Translation: The Influence of Experimental Design and Surface Modification. *International Journal of Molecular Sciences* **20**, doi:10.3390/ijms20236056 (2019).
22 Hajipour, M. J. *et al.* Personalized disease-specific protein corona influences the therapeutic impact of graphene oxide. *Nanoscale* **7**, 8978-8994, doi:10.1039/c5nr00520e (2015).
23 Yu, Q. H., Zhao, L. X., Guo, C. C., Yan, B. & Su, G. X. Regulating Protein Corona Formation and Dynamic Protein Exchange by Controlling Nanoparticle Hydrophobicity. *Frontiers in Bioengineering and Biotechnology* **8**, doi:10.3389/fbioe.2020.00210 (2020).
24 Hadjidemetriou, M., Al-Ahmady, Z. & Kostarelos, K. Time-evolution of in vivo protein corona onto blood-circulating PEGylated liposomal doxorubicin (DOXIL) nanoparticles. *Nanoscale* **8**, 6948-6957, doi:10.1039/c5nr09158f (2016).
25 Jain, R. K. & Stylianopoulos, T. Delivering nanomedicine to solid tumors. *Nature Reviews Clinical Oncology* **7**, 653-664, doi:10.1038/nrclinonc.2010.139 (2010).
26 Stylianopoulos, T. & Jain, R. K. Design considerations for nanotherapeutics in oncology. *Nanomedicine-Nanotechnology Biology and Medicine* **11**, 1893-1907, doi:10.1016/j.nano.2015.07.015 (2015).
27 Boucher, Y., Salehi, H., Witwer, B., Harsh, G. R. & Jain, R. K. Interstitial fluid pressure in intracranial tumours in patients and in rodents. *British Journal of Cancer* **75**, 829-836, doi:10.1038/bjc.1997.148 (1997).
28 Wang, T. T., Bai, J., Jiang, X. & Nienhaus, G. U. Cellular Uptake of Nanoparticles by Membrane Penetration: A Study Combining Confocal Microscopy with FTIR Spectroelectrochemistry. *Acs Nano* **6**, 1251-1259, doi:10.1021/nn203892h (2012).
29 Donahue, N. D., Acar, H. & Wilhelm, S. Concepts of nanoparticle cellular uptake, intracellular trafficking, and kinetics in nanomedicine. *Advanced Drug Delivery Reviews* **143**, 68-96, doi:10.1016/j.addr.2019.04.008 (2019).
30 Manzanares, D. & Cena, V. Endocytosis: The Nanoparticle and Submicron Nanocompounds Gateway into the Cell. *Pharmaceutics* **12**, doi:10.3390/pharmaceutics12040371 (2020).
31 Salvati, A. *et al.* Experimental and theoretical comparison of intracellular import of polymeric nanoparticles and small molecules: toward models of uptake kinetics. *Nanomedicine-Nanotechnology Biology and Medicine* **7**, 818-826, doi:10.1016/j.nano.2011.03.005 (2011).
32 Ibuki, Y. & Toyooka, T. in *Nanotoxicity: Methods and Protocols* (ed Joshua Reineke) 157-166 (Humana Press, 2012).
33 Salvati, A. *et al.* Quantitative measurement of nanoparticle uptake by flow cytometry illustrated by an interlaboratory comparison of the uptake of labelled polystyrene nanoparticles. *Nanoimpact* **9**, 42-50, doi:10.1016/j.impact.2017.10.004 (2018).

34 Jochums, A. *et al.* Revelation of Different Nanoparticle-Uptake Behavior in Two Standard Cell Lines NIH/3T3 and A549 by Flow Cytometry and Time-Lapse Imaging. *Toxics* **5**, doi:10.3390/toxics5030015 (2017).
35 Suzuki, H., Toyooka, T. & Ibuki, Y. Simple and easy method to evaluate uptake potential of nanoparticles in mammalian cells using a flow cytometric light scatter analysis. *Environmental Science & Technology* **41**, 3018-3024, doi:10.1021/es0625632 (2007).
36 Caracciolo, G., Farokhzad, O. C. & Mahmoudi, M. Biological Identity of Nanoparticles In Vivo: Clinical Implications of the Protein Corona. *Trends in Biotechnology* **35**, 257-264, doi:10.1016/j.tibtech.2016.08.011 (2017).
37 Roberts, M. J., Bentley, M. D. & Harris, J. M. Chemistry for peptide and protein PEGylation. *Advanced Drug Delivery Reviews* **64**, 116-127, doi:10.1016/j.addr.2012.09.025 (2012).
38 Jokerst, J. V., Lobovkina, T., Zare, R. N. & Gambhir, S. S. Nanoparticle PEGylation for imaging and therapy. *Nanomedicine* **6**, 715-728, doi:10.2217/nnm.11.19 (2011).
39 Russo, M. *et al.* PEGylated crosslinked hyaluronic acid nanoparticles designed through a microfluidic platform for nanomedicine. *Nanomedicine* **12**, 2211-2222, doi:10.2217/nnm-2017-0103 (2017).
40 Suk, J. S., Xu, Q. G., Kim, N., Hanes, J. & Ensign, L. M. PEGylation as a strategy for improving nanoparticle-based drug and gene delivery. *Advanced Drug Delivery Reviews* **99**, 28-51, doi:10.1016/j.addr.2015.09.012 (2016).
41 Soenen, S. J. *et al.* Cellular toxicity of inorganic nanoparticles: Common aspects and guidelines for improved nanotoxicity evaluation. *Nano Today* **6**, 446-465, doi:10.1016/j.nantod.2011.08.001 (2011).
42 Danhier, F. To exploit the tumor microenvironment: Since the EPR effect fails in the clinic, what is the future of nanomedicine? *Journal of Controlled Release* **244**, 108-121, doi:10.1016/j.jconrel.2016.11.015 (2016).
43 Jain, R. K. Transport of molecules across tumor vasculature.
44 Sykova, E. & Nicholson, C. Diffusion in brain extracellular space. *Physiological Reviews* **88**, 1277-1340, doi:10.1152/physrev.00027.2007 (2008).
45 Ireson, C. R., Alavijeh, M. S., Palmer, A. M., Fowler, E. R. & Jones, H. J. The role of mouse tumour models in the discovery and development of anticancer drugs. *British Journal of Cancer* **121**, 101-108, doi:10.1038/s41416-019-0495-5 (2019).
46 Verma, A. *et al.* Surface-structure-regulated cell-membrane penetration by monolayer-protected nanoparticles. *Nature Materials* **7**, 588-595, doi:10.1038/nmat2202 (2008).
47 van der Koog, L., Gandek, T. B. & Nagelkerke, A. Liposomes and Extracellular Vesicles as Drug Delivery Systems: A Comparison of Composition, Pharmacokinetics, and Functionalization. *Advanced Healthcare Materials*, doi:10.1002/adhm.202100639.
48 Bolhassani, A., Jafarzade, B. S. & Mardani, G. In vitro and in vivo delivery of therapeutic proteins using cell penetrating peptides. *Peptides* **87**, 50-63, doi:10.1016/j.peptides.2016.11.011 (2017).
49 Decuzzi, P. & Ferrari, M. The role of specific and non-specific interactions in receptor-mediated endocytosis of nanoparticles. *Biomaterials* **28**, 2915-2922, doi:https://doi.org/10.1016/j.biomaterials.2007.02.013 (2007).
50 Blanco, E., Shen, H. & Ferrari, M. Principles of nanoparticle design for overcoming biological barriers to drug delivery. *Nature Biotechnology* **33**, 941-951, doi:10.1038/nbt.3330 (2015).
51 Bevilacqua, P. *et al.* Antifouling Strategies of Nanoparticles for Diagnostic and Therapeutic Application: A Systematic Review of the Literature. *Nanomaterials* **11**, doi:10.3390/nano11030780 (2021).

52 Zhou, L. Y. *et al.* Novel zwitterionic vectors: Multi-functional delivery systems for therapeutic genes and drugs. *Computational and Structural Biotechnology Journal* **18**, 1980-1999, doi:10.1016/j.csbj.2020.07.015 (2020).

53 Francia, V., Reker-Smit, C., Boel, G. & Salvati, A. Limits and challenges in using transport inhibitors to characterize how nano-sized drug carriers enter cells. *Nanomedicine* **14**, 1533-1549, doi:10.2217/nnm-2018-0446 (2019).

54 Francia, V. *et al.* Corona Composition Can Affect the Mechanisms Cells Use to Internalize Nanoparticles. *Acs Nano* **13**, 11107-11121, doi:10.1021/acsnano.9b03824 (2019).

55 Tammaro, O., di Polidoro, A. C., Romano, E., Netti, P. A. & Torino, E. A Microfluidic Platform to design Multimodal PEG - crosslinked Hyaluronic Acid Nanoparticles (PEG-cHANPs) for diagnostic applications. *Scientific Reports* **10**, doi:10.1038/s41598-020-63234-x (2020).

56 di Polidoro, A. C. *et al.* Theranostic Design of Angiopep-2 Conjugated Hyaluronic Acid Nanoparticles (Thera-ANG-cHANPs) for Dual Targeting and Boosted Imaging of Glioma Cells. *Cancers* **13**, doi:10.3390/cancers13030503 (2021).

57 Costagliola di Polidoro Angela *et al.* Vol. Volume 2021 (Contrast Media & Molecular Imaging, 2021).

58 Corrado, B. *et al.* A three-dimensional microfluidized liver system to assess hepatic drug metabolism and hepatotoxicity. *Biotechnology and Bioengineering* **116**, 1152-1163, doi:10.1002/bit.26902 (2019).

I. CHAPTER 1 –SYNTHETIC IDENTITY OF HYALURONIC ACID-BASED NANOMATERIALS PRODUCED BY MICROFLUIDICS: CHARACTERIZATION OF NANOMATERIAL - ACTIVE AGENT INTERACTION

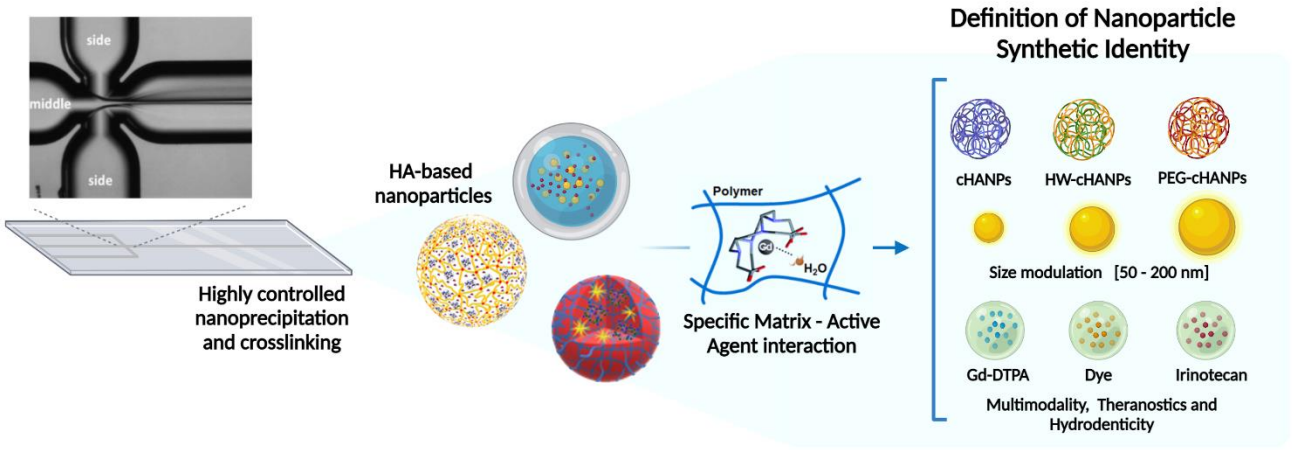

Graphical Abstract Chapter 1 – Exploitation of microfluidic HFF to study the interaction of active agents with the nanostructured polymer matrix and produce a library of nanoparticles with different synthetic identities.

I.I. Background

The implementation of a clinically relevant study about the connection existing between the synthetic identity and the biological identity of a nanocarrier, must pass through the choice of a fully biocompatible material and the implementation of a reliable, well-controllable production process to assure uniform and well-tailored products, as previously discussed.

Among polymer materials, the use of Hyaluronic Acid (HA) provides several advantages both biological and technological. HA is a biodegradable, biocompatible, non-toxic and non-immunogenic glycosaminoglycan with negative charge. Due to its strong hydrophilic character, it can absorb a large amount of water, up to 1000 times its solid volume. As normal constituent of the extracellular matrix, it plays an important biological role in modulation of inflammation following tissue injury[1-6]. Being widely used for clinical and cosmetic application, it represents a clinically promising material[3,7,8]. In the field of nanomedicine, it has been widely explored for the development of many different applications, being highly hydrophilic, it bears natural stealth properties[9,10] and it is a natural target for cancer tissue. Indeed, HA is the substrate of the CD44 receptors, overexpressed by many cancer cell type[7]. Although all these properties and therapeutic benefits are promising, exogenous HA is not stable in tissues for longer durations. This short residence time of unmodified HA results from its spontaneous and rapid degradation by HAdases, which specifically cleave the molecule at β 1,4 glycosidic bond[11].

Therefore, to obtain materials that are more mechanically and chemically robust, a variety of hydrophobic modifications and chemical cross-linking strategies have been explored to produce insoluble or gel-like HA materials. In the possibilities of modification of hydroxyl group present in the polymer backbone, HA crosslinking with divinyl sulfone (DVS) is very promising since the HA-DVS degradation products are non-toxic and FDA approved[5,12]. This reaction is performed at room temperature in high pH conditions (pH > 8). Technologically, hydrogels, and particularly HA, offer the unique possibility of boosting the relaxometric properties of Gd-based contrast agents up to 12-fold in a crosslinking-dependent manner, through the property of Hydrodenticity[5,13-15]. Hydrodenticity arises from a complex equilibrium formed by elastic stretches of the polymer chains, water osmotic pressure and the hydration degree of Gd-CAs. The ability of the Hydrodenticity to boost the relaxometric properties of Gd-chelates can, on one side, improve MRI performances of the CA and, on the other side, potentially reduce its administered dose keeping performances unmodified.

Regarding the choice of NP production processes, nanoprecipitation-based methodologies offer significant improvements with respect to other production techniques being less complicated and time consuming [16-19]. Despite these advantages, limitations such as high batch-to-batch variations, non-homogenous reaction environment and insufficient production rate reveal the need to move towards techniques providing a higher control in the production of nanosystems with well-defined features.

In this sense, the advent of microfluidics constituted a breaking point. This simple, cost-effective and scalable technology poses as an alternative way to implement consolidated production processes, strongly improving their controllability. Indeed, microfluidic-based production offers the possibility of tuning product composition and properties by simple process parameter adjustments [20-24], such as flow rate ratio, polymer concentration, pH and temperature. In addition, when microfluidic platforms are used as microreactors, they provide improved space-time yields (product formed per reactor volume and time), producing faster reactions than bulk counterparts. Moreover, the degree of control over local environmental conditions is such to guarantee homogeneous products[25-28].

The listed attributes contribute to the definition of microfluidics as a “disruptive technology” for the production of tailorable nanovectors and the acceleration of their clinical translation[26,29].

An efficient implementation of nanoprecipitation for particle production in microfluidics is the hydrodynamic flow focusing (HFF) regimen[4,5,24,30]. Indeed, as reported by Liu *et al*.[29] the HFF can be used to improve different component mixing and to induce nanoprecipitation.

One of the first examples is presented by Karnik and co-workers [31], who produced PLGA-PEG nanoparticles, studying the effect of the flow-rate ratio on particle size and polydispersity by micellization. Recently, Xu *et al*., proposed a continuous flow focusing–based strategy to improve the encapsulation efficiency (EE%) of Tamoxifen and Doxorubicin, a hydrophobic and a hydrophilic anticancer drug respectively, in PLGA NPs[32]. In this work, they demonstrated that an improved EE% translates into

a more controlled drug release. A homogeneous drug distribution in the particle core is, in fact, able to avoid the initial burst release due to superficial drug distribution.

In this chapter it is presented the production and characterization of a library of HA-based nanoparticles with different synthetic identities produced starting from a patented process for the microfluidic production of crosslinked Hyaluronic Acid Nanoparticles (cHANPs). Microfluidic nanoprecipitation was implemented and optimized for two different HA molecular weights (50kDa and 250kDa) and for a functionalized HA (thiolated HA, HA-SH) for direct one-step crosslinking and PEGylation (polyethylene glycol-vinyl sulfone, PEG-VS) of cHANPs. Different active agents involving both imaging agents and therapeutics have been encapsulated to explore the impact that they have on the processes of nucleation, growth and crosslinking of the NPs. The produced nanovectors have been characterized morphologically, structurally, for the Hydrodenticity property, and when simultaneous agents are encapsulated, for their multimodal imaging and theranostic capabilities.

I.II. Experimental Section

I.II.I. Materials

Hyaluronic Acid HA (Mw=50000 Da, 250000 Da), Thiolated Hyaluronate HA-SH (Mw=50000 Da; $Substitution\ degree$ (SD)=5%), Poly ethylene glycol – vinyl sulfone PEG-VS (Mw = 2000 Da, SD = 100% $linear\ chain$; Mw= 20000 Da, SD = 400% $four\ arm\ chain$) were purchased from Creative PEGWorks (USA). Divinyl Sulfone DVS also known as Vinyl Sulfone (contains <650 ppm hydroquinone as inhibitor; purity 97%; density 1,117 g/ml at 25°C (lit.); Mw=118,15 g/mol), Gadolinium - diethylenetriamine penta-acetic acid Gd-DTPA (Mw=547,43 g/mol), Acetone (CHROMASOLV, for HPLC, ≥99,8%; molecular formula $CH3COCH3$; Mw=58,08), Ethanol (ACS reagent, ≥99,5% (200 proof), absolute; molecular formula $CH3CH2OH$; Mw=46,07), Sodium Hydroxide NaOH (ACS reagent, ≥97,0%, Mw=40,00), ATTO 488 MW 804 g/mol (Ex/Em 488/520) and ATTO 633 MW 652 g/mol (Ex/Em 633/655) were purchased from Merck KGaA (Germany). The Water, used for synthesis and characterization, was purified by distillation, deionization, reverse osmosis (Milli-Q Plus) and finally filetered with a 0,22 µm cutoff filter.

I.II.II. Microfluidic HFF to produce HA-based nanoparticles

Microfluidics is a scalable and cost-effective technology based on the manipulation of very small amount of liquids in channels with miniaturized dimensions. This has a lot of implications: the specific Reynolds number (Re = ρvl/η) of liquid flowing in such microchannels is very small, typically smaller than 100. In such low Reynolds number regimes, turbulent mixing does not

occur, and hence diffusive species mixing dominates allowing a fine control over molecules interaction despite this is an inherently slow process. Being a continuous process, temporal control of reactions by adding reagent at precise time intervals during the reaction process and in situ monitoring of the progress of reaction through residence time-based resolution are possible. Those features make microfluidic reactors particularly appealing in the production and investigation of nanomaterials as compared with conventional macroscale reactors, especially in applications requiring control of reactions at the molecular scale. When coming to particle production, different chip geometry and flow regimes can be implemented depending on the desired final properties of the product. The most effective implementation of nanoprecipitation for nanoparticle production is the Hydrodynamic Flow Focusing (HFF). HFF is based on the use of a three-inlet microfluidic device. The middle stream is squeezed by lateral flows to a width related to the flow rate ratio (FR^2), defined as the ratio between the volumetric flow rate of the solvent phase (middle channel) and the non-solvent phase (side channels)[5]. Thus, tuning the FR^2, it is possible to reduce the τ_{mix} of the components improving the probability of reaction occurrence[22].

Many authors identify the mixing time (τ_{mix}) as the key parameter for controlling NP formation by nanoprecipitation. A short mixing ensures a homogeneous spatial environment which leads to uniform reaction conditions and particle formation kinetics. However, this short mixing is very difficult to achieve in batch preparations while in a microfluidic setting, the proper choice of chip geometry and process parameters, with particular reference to the flow rate ratio, allow to accurately tune the mixing time which is defined as:

$$\tau_{mix} \approx (w_f^2/4\mathrm{D})$$

where w_f is the width of the focused stream and D the solvent diffusion coefficient. In recent years, the literature showed a great interest in the use of HFF and effective mixing[22].

The modulation of the τ_{mix} can ensure uniform reaction condition and particle formation kinetics when $\tau mix < \tau agg$ (time for NPs aggregation). In fact, when this condition is verified, particles are smaller in size and more homogeneous.

In the focused stream, particles are formed via nanoprecipitation. It is based on the presence of two phases known as solvent (organic) and non-solvent (aqueous) phase. The solvent phase essentially consists of a solution in a solvent or in a mixture of solvents of the particle-forming substance which is injected in the middle channel; the non-solvent phase consists of a non-solvent or a mixture of non-solvents for the particle-forming substance and is injected in the two

side channels[16]. Nanoparticles are obtained as a suspension formed when the aqueous phase solvent extracts the organic phase one, leading the concentration of solute at a critical nucleation condition. This happens at the boundaries of the focused stream, where the two phases come in contact. At this point, nuclei form by condensation until they rich a critical size at which they are stable against dissolution. The nucleation phase proceeds until the concentration of the solute falls below the critical nucleation threshold, where new nuclei cannot be any longer formed. However, this concentration is still sufficient to allow the growth of the nuclei already formed. The growth phase proceeds until the concentration of the still-dissolved material has fallen to the equilibrium concentration (i.e. bulk solubility). The resulting size at the end of aggregation is strongly correlated with the polymer concentration and, consequently, the viscosity of the solution. The viscosity should be sufficiently low to suppress entanglements between the polymer chains, which, when present, are sufficient to fail the creation of nanoparticles.

I.II.III. Microfluidic set-up

The microfluidic set-up is composed by a quartz microfluidic chip "Droplet Junction Chip, 190 μm x 390 μm etch depth" purchased from Dolomite Centre Ltd. The device comprises both an X-junction and a T-junction, but the X-juction was exploited in this work. X-junction is made up by three inlet channels and a single outlet channel used to mix and induce the reaction of the reagents. Chip and its geometry and dimension are reported in the following Figure 1.1

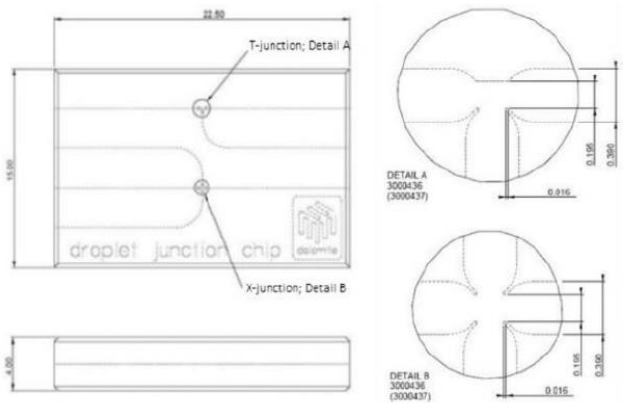

Figure 1.1 – Geometry and dimension of the Droplet junction chip

The device is connected to 5 and 10 mL glass syringes, purchased from Setonic GmBH to inject the solvent and non-solvent solutions respectively. Syringes are mounted on high-precision low-pressure syringe pumps (neMESYS 290N (CETONI)) with FEP tubing (1.16''×0.8mm) by means of ETFE two-ways valves, which allow to quickly start or stop flow streams. Tubes are connected to the device through a H-interface and PTFE linear connectors.

Nemesys PC user interface allows to select channels flow rates and syringe volumes; Flow rates of the lateral channels are set to an equal value, higher with respect to the central channel in order to keep HFF. Samples are collected in a glass petri dish in 25 mL of Acetone. Flow-focusing is observed using an Optical Fluorescent Microscope (Olympus IX71) with a 4 or 10 x scanning objective.

cHANPs, HW-cHANPs and PEG-cHANPs production process

Nanoparticles are produced in a microfluidic X-junction chip where the hydrodynamic flow focusing regime is used to implement a nanoprecipitation process.

For the production of cHANPs co-loaded with Gd-DTPA and a fluorophore, the solvent phase is made of HA (0,5% w/V), Gd-DTPA (0,1% w/V) and ATTO 488 or ATTO 633 (10 nmol/mL) and fed in the middle channel at 27 µL/min. The aqueous phase is made of acetone and Divinyl Sulfone (DVS) (4% V/V) and is fed in the side channels at 110 µL/min. The sample is collected in 20 mL of Acetone and wheel stirred overnight to promote DVS diffusion and complete the crosslinking reaction. The same process is implemented for the production of HW-cHANPs but a High-molecular weight hyaluronic acid (250kDa) is used at a concentration of 0.001% w/V and middle and side flow rates are set to 15 µL/min and 120 µL/min, respectively. For the production of multimodal HW-cHANPs, coloaded with Gd-DTPA and a fluorophore,), Gd-DTPA (0,1% w/V) and ATTO 633 (10 nmol/mL) are dissolved in the solvent phase. To produce theranostic cHANPs (Thera-cHANPs) a co-solvation strategy is implemented. The solvent solution is made of HA (0.05% w/V), Gd-DTPA (0.1% w/V), Irinotecan (0,025% w/V) and ethanol 10% V/V and is injected at 27 µL/min. The aqueous phase is made of acetone and Divinyl Sulfone (DVS) (4% V/V) and is fed in the side channels at 110 µL/min. In all cases, the pH of the solvent solution is adjusted at 12.2 by NaOH addition to promote the occurrence of the crosslinking reaction between HA and DVS. The sample is collected in 20 mL of Acetone and wheel stirred overnight to promote DVS diffusion and complete the crosslinking reaction.

The production of PEG-cHANPs occurs by the implementation of a similar process, however, the crosslinking reaction occurs simultaneously to the PEGylation by means of a Michael addition reaction between thiol groups of the HA-SH and vinyl sulfone moieties of PEG-VS. To this purpose, the solvent phase of HA-SH (0,05% w/V), PEG-VS (0,18% w/V), Gd-DTPA (0,1% w/V) and ATTO 633 or ATTO 488 (10 nmol/mL) is fed in the middle channel at 30 µL/min and the aqueous phase of pure acetone is fed in the side channels at 110 µL/min. In order to promote the occurrence of the Michael addition at the junction of the microfluidic chip and avoid a premature crosslinking prior injection, the solution and the syringe used for the injection are kept at 4°C at

which the velocity of the reaction is strongly reduced. The sample is collected in 20 mL of Acetone and wheel stirred overnight.

Nanoparticle purification

In all cases, purification is performed by two-step solvent gradient dyalisis, dropping the suspension in Spectra Por Cellulose Membrane 6 (MWCO 50 kDa). The first purification step is in ethanol and the second in water, through increasing gradient of acetone-ethanol (70/30% V/V, 50/50% V/V and 30/70% V/V) and ethanol-water respectively, as before. Diffusion is promoted by continuous stirring at 230 rpm and Room Temperature.

Chemical-physical characterization of cHANPs, HW-cHANPs and PEG-cHANPs

NP size, polydispersity and superficial charge are measured by dynamic light scattering (DLS, Zetasizer Nano ZS, Malvern UK). Typically, 1 mL of diluted sample is put in 12 mm square glass cuvettes for 90° sizing (Optical Cuvette, Sarstedt) and measured at least in triplicate. Zeta potential measurements are performed at room temperature on a Zetasizer Nano ZS (Malvern, UK), fitted with a high-concentration zeta potential cell. Nanoparticle morphology is assessed by Scanning and Transmission electron microscopy, SEM and TEM respectively. For SEM observations (Carl Zeiss Ultraplus Field Emission) 200 µL of purified samples are dropped on a polycarbonate Isopore membrane filter (different cut-offs 0.05, 0.1 and 0.2 µm) under vacuum ultrafiltration and let dry overnight. Prior the observation, 7 nm of Au are deposited on the sample. For TEM analysis (Cryo-TEM TECNAI by FEI) 20 µL of the purified sample are dropped on a Carbon Film membrane (Agar scientific) and let dry overnight.

Determination of cHANPs, HW-cHANPs and PEG-cHANPs Encapsulation Efficiency (EE%)

To quantify the content of Gd-DTPA in NPs, Inductively Coupled Plasma ICP-MS NexION 350 measurements, PerkinElmer Inc. (Waltham, Massachusetts, USA), are performed. Determination of Irinotecan, ATTO488 or ATTO633 content is performed through a Multiplate Reader Photometer Enspire Perkin-Elmer Inc. (Waltham, Massachusetts, USA), (Abs at 368 nm, λ ex/em 488-560 and 633-670 nm, respectively). The calibration curve to correlate absorbance and fluorescent intensity to drug and fluorophore concentration is obtained. For Gd-DTPA, Irinotecan and the fluorophore, the encapsulation efficiency (EE%) is calculated as

$$EE\% = \frac{C_M}{C_I} \cdot 100,$$

where C_M is the measured amount of substance in the purified sample and C_I its initial concentration.

Fluorescent imaging technique by SP5 Laser Scanning Confocal Microscope, Leica Microsystem (Germany) is used to localize the fluorophore inside nanoparticles by visualization of fluorescent spots.

cHANPs, HW-cHANPs and PEG-cHANPs relaxometric properties

To characterize NPs relaxometric properties, in vitro MR measurements on co-loaded cHANPs HW-cHANPs and PEG-cHANPs are performed and results are compared to Gd-DTPA solutions at similar concentrations. After vigorous stirring, 300 µL of the sample is dropped in a glass tubes and changes in longitudinal relaxation time (T1) at 1.5 Tesla and 37°C by Minispec Bench Top Relaxometer (Bruker Corporation) are measured.

FTIR measurement for crosslinking reaction occurrence

Fourier transform infrared spectra (FT-IR) were collected from Nicolett 6700 FT-IR spectrometer
(Thermo Scientific). IR spectra were collected for HA-SH, mPEG-VS, 4arms-PEG-VS and PEG-cHANPs at 0.09 cm-1 resolution with 2 min interval. Spectra were for signal assignation.

I.III. Results

Over years, the study of nano-bio-interactions relied on the use of inorganic NPs for their ease of production and characterization. However, as widely discussed in the previous sections, the clinical relevance of these systems is still unclear due to their unclear toxicity profile upon in-vivo injection. For this reason, few clinically relevant results have been achieved up to now. Herein, we proposed microfluidic hydrodynamic flow-focusing as a simple, scalable, highly controllable technique to produce fully biocompatible HA-based nanoparticles with well-defined features starting from a patented process of our research group.

I.III.I. Co-encapsulation of multiple active agents for cHANPs Multimodal Imaging and Theranostics

As described in the method section, crosslinked Hyaluronic Acid Nanoparticles (cHANPs) co-encapsulating Gd-DTPA and a fluorophore (ATTO 488 and ATTO 633 were tested), high molecular weight-cHANPs (HW-cHANPs), theranostic cHANPs (Thera-cHANPs) and pegylated-cHANPs (PEG-cHANPs) were produced by nanoprecipitation, according to the methodology previously described. A feasibility study on the platform led to the optimization of the process parameters in terms of polymer concentration, FR^2 defined as $\frac{middle\ flow\ rate}{side\ flow\ rate}$, pH and temperature of solvent solution injection.

cHANPs were produced both as a multimodal imaging probe by the co-encapsulation of Gd-DTPA and a standard dye (ATTO 633 or ATTO 488) and as a theranostic probe (Thera-cHANPs) by the co-encapsulation of the clinically approved camptothecin, irinotecan (CPT-11). Briefly, for the production of coloaded cHANPs, a solvent phase of HA (0.05% w/V), Gd-DTPA (0.1% w/V), ATTO 488 or ATTO 633 (10 nmol/mL) and NaOH (pH = 12.2) is injected in the middle channel at 27 µL/min. In the side channels, DVS (4% V/V) dissolved in acetone is injected at a flow rate of 110 µL/min. A schematic of the production process is presented in Figure 1.2

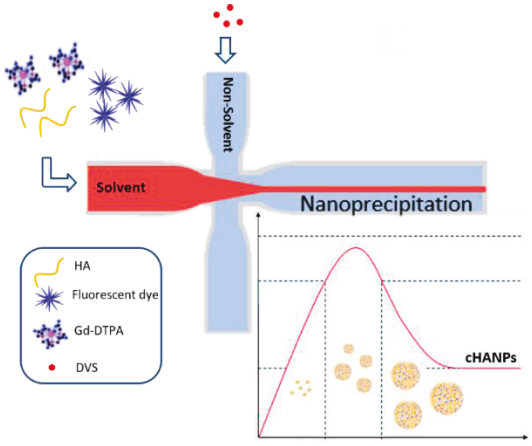

Figure 1.2 – Schematic representation of the microfluidic HFF production process of co-loaded cHANPs

As shown in Figure 1.3, the particle size distribution (PSD) of co-encapsulated cHANPs was measured by DLS and a mean size of 99,48 ± 33,93 nm was obtained, a value slightly higher than Gd-loaded cHANPs, previously reported[5]. This can be attributed to the presence of ATTO in the solvent solution which, being a water-soluble agent, interferes with water extraction from the solvent to the nonsolvent phase, in this way impacting the particle precipitation phase of nucleation.

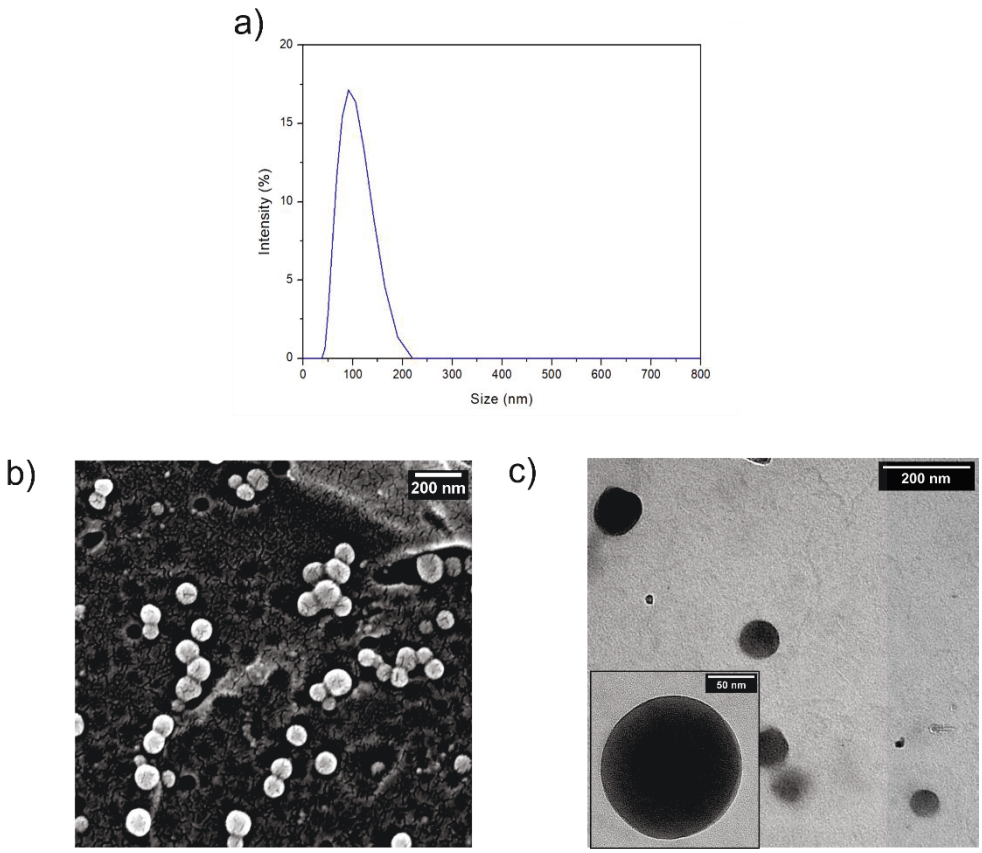

Figure 1.3 – Physical chemical characterization of co-loaded cHANPs. a) Particle Size Distribution (PSD) by DLS measurement; b) Scanning electron microscopy (SEM) images of co-loaded cHANPs; c) Transmission electron microscopy (TEM) images of co-loaded cHANPs.

Secondly, both Gd-DTPA and ATTO 633 EE% were measured, showing values of 3,59% and 16% respectively. Also in this case, a difference in the EE% due to the presence of ATTO in the core of NPs, was observed. To localize ATTO 633 inside NPs, fluorescent imaging was performed, and the presence of fluorescence spots as well as the absence of diffuse fluorescence confirmed both the successful encapsulation and purification from the non-entrapped dye, Figure 1.4a. Please note that the dimension of the fluorescent spots does not correlate with the real dimension of cHANPs due to the poor resolution of the optical light.

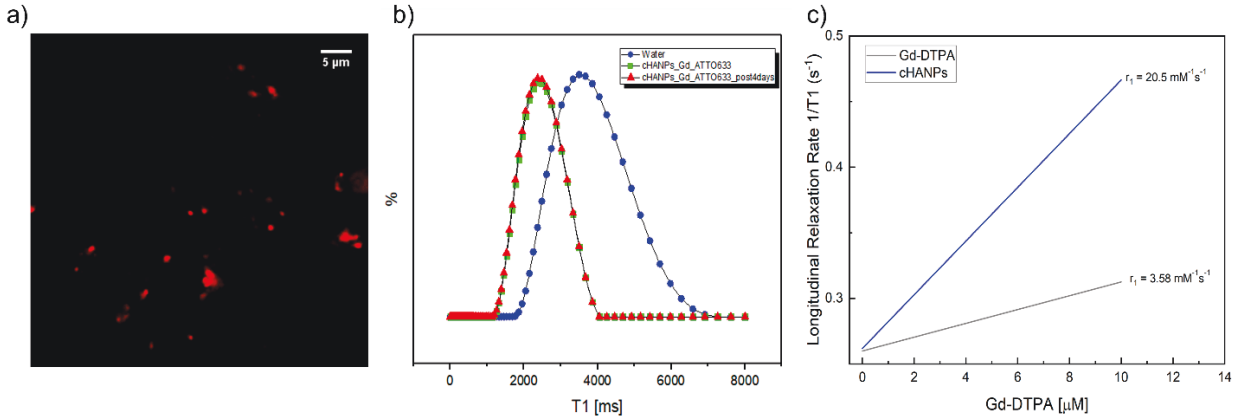

Figure 1.4 – Characterization of cHANPs co-encapsulation ability and Hydrodenticity property. a) Fluorescent imaging analysis of cHANPs; b) In-vitro longitudinal relaxation time of co-loaded cHANPs by Minispec Benchtop relaxometer; c) Comparison of co-loaded cHANPs and free Gd-DTPA relaxivity for quantification of Hydrodenticity boosting.

Then, longitudinal relaxation time (T1) of cHANPs was measured and Hydrodenticity was assessed by comparing the relaxivity of the coloaded particles with the relaxivity of the free Gd-DTPA at the same concentration. Results showed that cHANPs with a longitudinal relaxivity r_1 of 20.5 $mM^{-1}s^{-1}$ provided a boosting of about 5 times with respect to free Gd-DTPA (r_1=3,58 $mM^{-1}s^{-1}$). Comparing results with the previous finding of a crosslinking-dependent boosting of Gd-loaded cHANPs up to 12-times[13], it can be concluded that the presence of ATTO is interfering with the effect of Hydrodenticity and it can be hypothesized that this effect is due to a less efficient coordination of water molecules from the bulk of the particles with Gd-DTPA, with the overall effect of a reduced relaxivity.

When exploring the theranostic design, Irinotecan was chosen as a clinically approved drug for the treatment of many different solid tumors[33-35]. It is a slightly water-soluble chemotherapeutic prodrug, with a water solubility of 1 mg/mL but a good solubility in alcohols (i.e. ethanol and acetone). Initial Irinotecan concentration in the solvent solution was set at 0,005% *w/V*. In this way, a very low amount of drug (0,5 µM) was encapsulated inside nanoparticles, reaching an EE% of 1 – 2%. This very low EE% was probably determined by the fast diffusion of Irinotecan towards the lateral walls of the outlet channel, where acetone flows. In addition, these values are far away from therapeutic concentration values, reported to be in the range of 10-100 µM[34]. For this reason, a co-solvation strategy was explored to increase the amount of CPT-11 that could be dissolved in the solvent phase. To the purpose, 10 % V/V of ethanol was added to the solvent phase, and Irinotecan concentration was increased to 0,025% w/V. A schematic of the production process is presented in Figure 1.5.

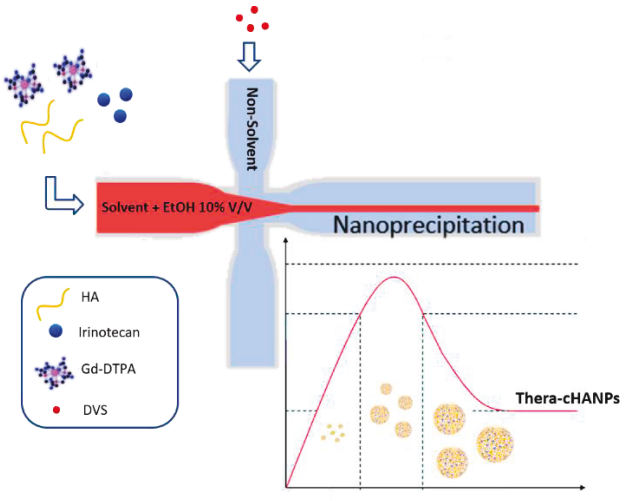

Figure 1.5 - Schematic representation of the microfluidic HFF production process of Thera-cHANPs

This process led to the formation of a uniform population of spherical particles with a mean dimension of 106,79± 46,33 nm as presented by SEM images and PSD in Figure 1.6a and b. In addition, thanks to cosolvation, a significantly higher concentration of drug was encapsulated, reaching a concentration of 17,5 µM, and an EE% of 4%. Concerning Gd-DTPA encapsulation, ICP-MS measurement revealed a content of 8,5 µM of Gd-DTPA and an EE% of 3%. As previously, for Thera cHANPs the comparison of the nanoparticle relaxivity and the relaxivity corresponding to free Gd-DTPA at the same concentration was performed and the analyses revealed a relaxivity boosting of 2,18 times, with Thera-cHANPs relaxivity r_1 = 9,09 $mM^{-1}s^{-1}$ as presented in Figure 1.6c. Results confirmed that the co-encapsulation of a second agent in the bulk of the particles reduced both the encapsulation efficiency and the Hydrodenticity mediated boosting as a consequence of a less efficient coordination of water molecules. In this case, the effect of relaxivity reduction is much pronounced, effect which might be attributed to the hydrophobic nature of Irinotecan drug.

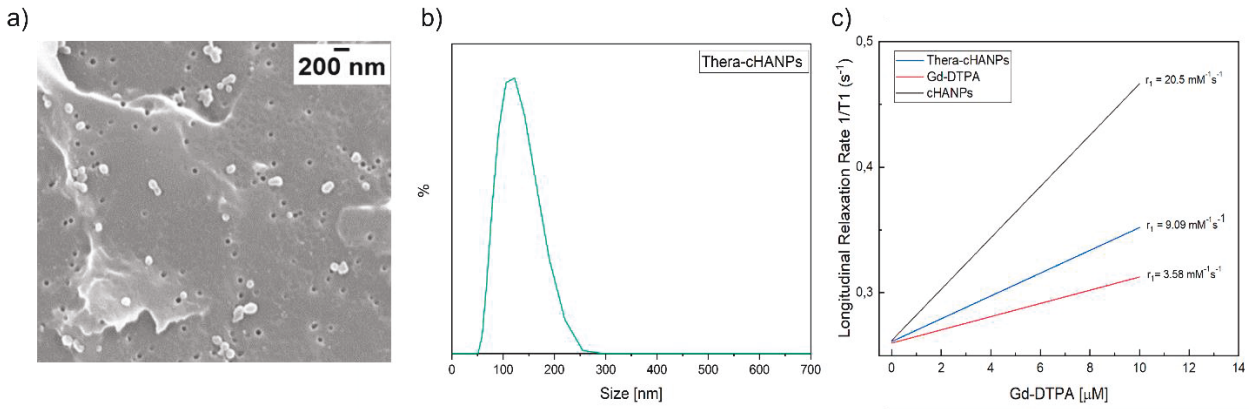

Figure 1.6 – Thera-cHANPs characterization. a) SEM images of Thera-cHANPs; b) PSD of Thera-cHANPs by DLS; Comparison of Thera-cHANPs, co-loaded cHANPs and free Gd-DTPA relaxivity for quantification of Hydrodenticity boosting.

I.III.II. High Molecular Weight HA for improved NP stability and encapsulation efficiency: HW-cHANPs

To study the impact of polymer MW on particle production, stability, and EE%, the same process was implemented for HA with a MW of 250 kDa. As a first step, a feasibility study was implemented exploring two different values of polymer concentration (0.005% w/V and 0.001% w/V), different FR^2 ranging from 0.125 to 0.32 and four different DVS concentrations from 1% V/V to 6% V/V, as reported in Figure 1.7 a and b. To control the precipitation of the polymer and specifically, to move the equilibrium of the production process from a growth-based to a nucleation-based one, which allows to obtain uniform and smaller particles, we choose as optimized condition the lower polymer

concentration, which is HA = 0.001% w/v. This choice allowed us to process less amount of polymer per unit time and assure a much faster and more homogeneous water extraction and polymer precipitation. In addition, the smaller FR^2 allowed to finely control the solvent extraction process and polymer concentration without any destabilization in the flow focusing standing the much higher viscosity of the solvent solution due to the higher polymer MW. For this reason, the smallest FR^2 was set as optimal condition, which is FR^2 = 0.125. In this condition a uniform population of spherical particles with a mean dimension of 118.6 ± 24 nm was obtained, as presented in Figure 1.7c and d.

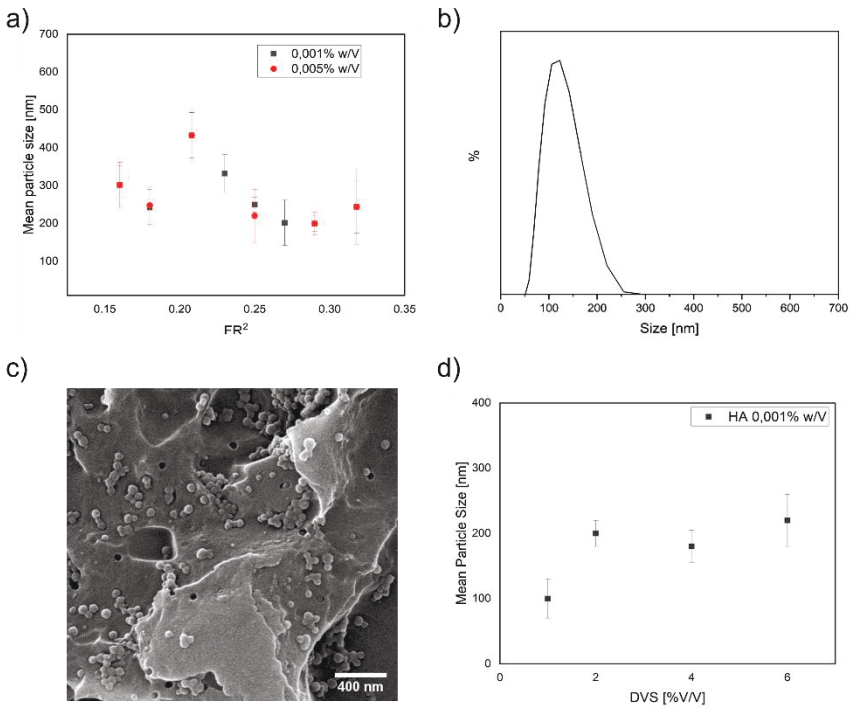

Figure 1.7 – Feasibility study for the production of High moleculear weight cHANPs (HW-cHANPs). a) Effect of FR^2 on nanoparticle size and polydispersity for two different polymer concentrations; b) PSD of the optimized condition of HA=0.001% w/V and FR2=0.125; c) SEM of HW-cHANPs d) Effect of DVS concentration on particle size and polydispersity

Regarding the crosslinking reaction, in the previously optimized condition of pH= 12.2, the DVS concentration of 4% V/V assured a uniform particle population of 200 ± 10 nm and thus was chosen as optimized condition. Indeed, despite it seems that in 1% V/V concentration a smaller and more uniform particle population was obtained, their stability over time could not be demonstrated. At 1 week analysis of particle size and morphology, DVS 4% V/V was the condition assuring the most uniform particle population with reduced swelling, as presented in Figure 1.8. This indirectly demonstrated the successful occurrence of the crosslinking reaction.

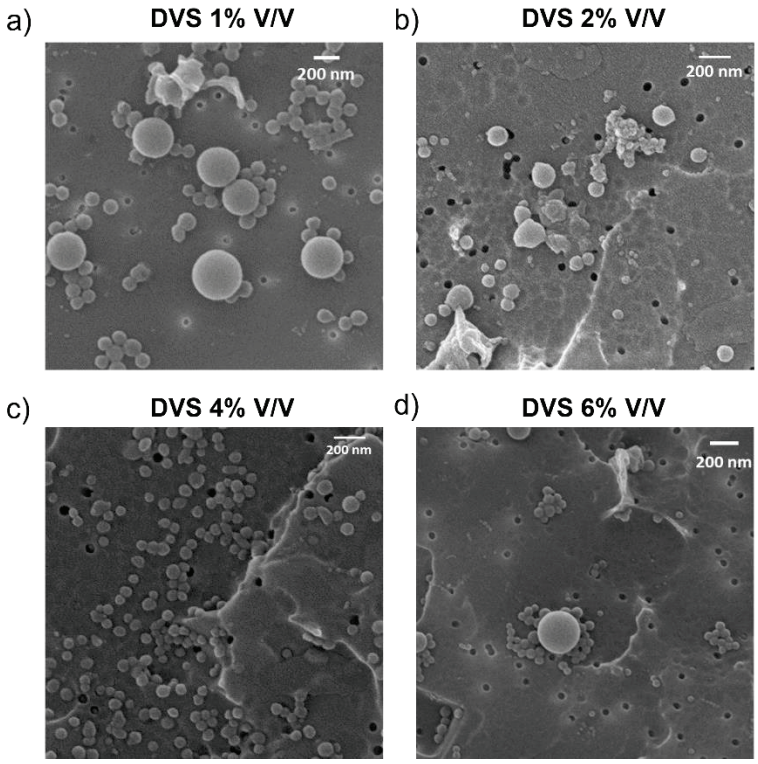

Figure 1.8 – SEM images of HW-cHANPs after 1 week in water for indirect evaluation of crosslinking reaction occurrence

Then, Gd-DTPA and ATTO 633 were co-encapsulated in HW-cHANPs and an EE% of 79% and 1% were achieved respectively. The very high encapsulation efficiency reached for Gd-DTPA revealed that the precipitation of HA chains was very fast, thus preventing Gd-DTPA diffusion in the outer stream, resulting in a very high amount of Gd entrapped in the polymer network. Differently, being the water solubility of Gd-DTPA higher than the ATTO one, this excluded most of the ATTO from the particles, leading to a much lower encapsulation efficiency for the dye. Measurement of HW-cHANPs relaxivity and comparison with relaxivity of free Gd-DTPA at the same concentration showed that no Hydrodenticity-based boosting was present, Figure 1.9b.

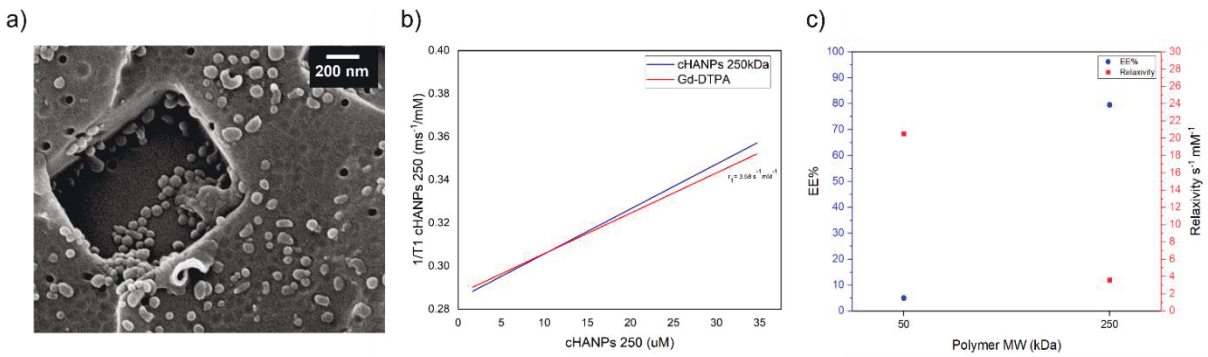

By comparing results obtained by cHANPs and HW-cHANPs some conclusions about the role that the polymer MW has on the particle stability and EE% can be drawn. A lower polymer MW offers a much controllable precipitation process. However, in HW-cHANPs, simple process parameter adjustment might lead to single chain precipitation guaranteeing a much higher stability of the resulting particles. Regarding particle degradation, a higher polymer MW might increase the time required for degradation thus slowing down the release of encapsulated agents. Finally, despite EE% is increased when increasing polymer MW, the particle structural parameters are much more complex to manage due to high chain entanglement and for this reason the optimal crosslinking density for the occurrence of the Hydrodenticity effect is not trivial to be defined, as presented in Figure 1.9c. Indeed, in the optimized crosslinking conditions of HW-cHANPs, no Hydrodenticity effect was observed.

I.III.III. One-step production of PEG-crossliked Hyaluronic Acid NPs: feasibility study and multiple agent encapsulation for Multimodal Imaging applications

It is known that, when nanoparticles are injected in the systemic circulation, plasma proteins adsorb on NP surface and the formation of a *protein corona* occurs. This phenomenon facilitates the clearance of NPs by macrophages of the reticuloendothelial system (RES). Among the most effective strategies to increase the circulation time of nanoparticles there is the surface pegylation, where the hydrophilic PEG on NPs surface creates a hydrated layer around the NPs (opsonization), avoiding the protein corona formation and recognition and clearance by the RES.

Pegylated cHANPs (PEG-cHANPs) were produced in a one-step process as described in the dedicated method section. A schematic of the production process is presented in Figure 1.10.

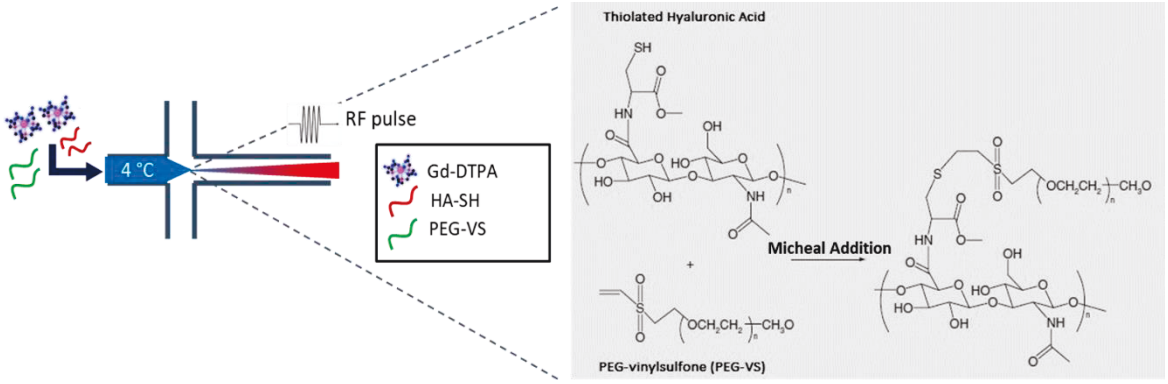

Figure 1.10 - Schematic representation of the microfluidic HFF for one-step crosslinking and PEGylation of PEG-cHANPs

A study about the feasibility of the particle production process is conducted to evaluate the effect of the $FR^2$and functional group ratio on the obtaining and size of the nanoparticles.

As first step, different FR^2 values ranging from 0.06 to 0.44 were tested to characterize their influence on nanoprecipitation phases of nucleation and growth. Middle channel flow rates were varied from 10 µL/min to 40 µL/min while side ones from 90 µL/min to 160 µL/min. From the analysis of the results in Figure 1.11a, it was possible to identify three different regions. In the first one the mean particle size is around 30 nm. In the second region, particle size increases from ~ 250 nm to ~ 800 nm. Finally, the third region is characterized by massive precipitation. Indeed, in this range, SEM observations show the formation of big aggregates and films of material that compromise the DLS analysis.

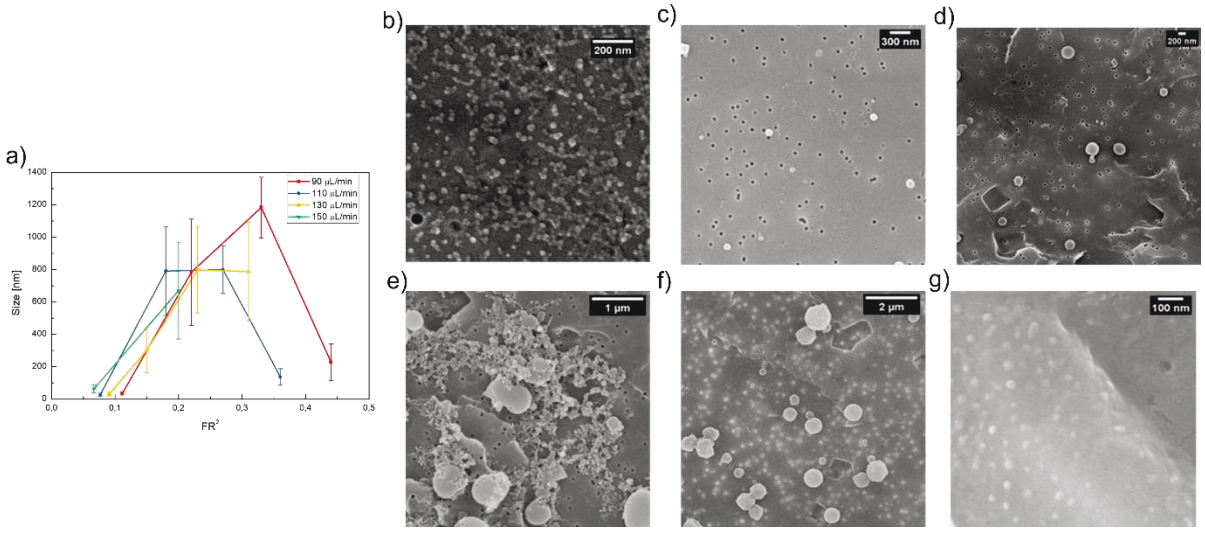

Figure 1.11 – Effect of the flow rate ratio on particle nanoprecipitation. a) Effect of the FR2 on particle size and polydispersity; b) and c) SEM images representative of the first region; d)-f) SEM images representative of the second region; g) SEM image representative of the third region.

This suggests that increasing the FR^2 over a certain limit, the production moves towards a region in which every variation would not produce any effect different from uncontrolled and massive aggregate precipitation. For these reasons, we selected as Operative-working Region (OR) for FR^2 the second region. Moreover, since a FR^2 value of 0.27 (obtained at 30 µL/min – solvent flow rate – and at 110 µL/min – non solvent flow rate) provides a fine and stable flow focusing and absence of precipitates in the mixing channel, it is selected as the optimized condition and used in the next experiments.

A study of the influence of the functional group ratio (defined as the number of thiol groups over the number of vinyl sulfone groups, SH/VS) on particle size and the crosslinking occurrence, is conducted. Literature data on the SH/VS ratio are reporting a value of 1.2 and a total polymer concentration of 6% w/V as the optimized condition for batch processes [36-38]. To make a comparison about the traditional batch processes and the more efficient microfluidic approach and to evaluate the impact of this ratio on the stability of the PEG-cHANPs, a study about the microfluidic implementation of the

Michael addition is conducted. At our standard FR value of 0.27, the total polymer concentration is reduced up to 0.23% w/V and significantly smaller values of the functional group ratio are explored. SH/VS value has been varied from 0.0009 to 0.2, as presented in Figure 1.12a.

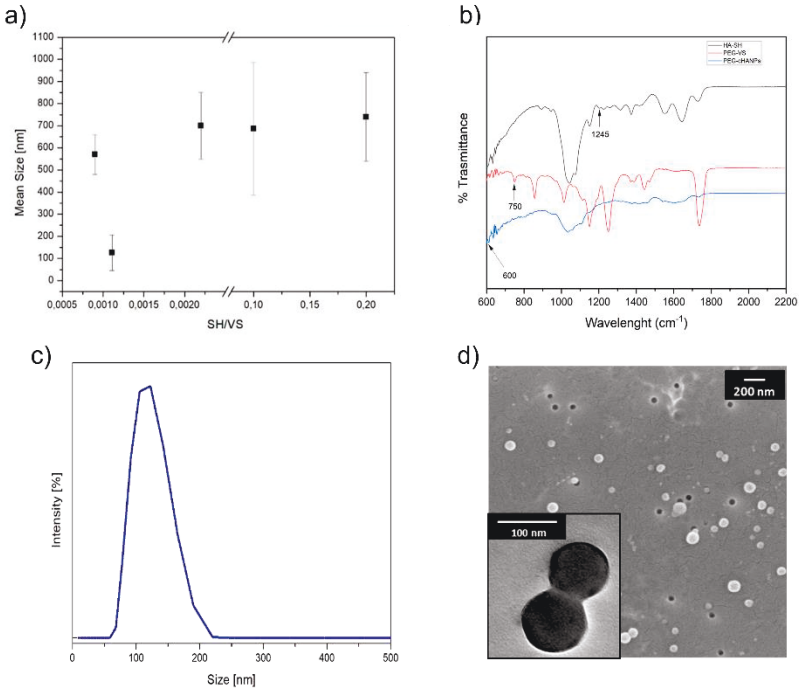

Figure 1.12 – Feasibility study for microfluidic implementation of Michael addition reaction. A) effect of functional group ratio SH/VS on particle production and polydispersity; b) FTIR spectra of HA-SH, PEG-VS and PEG-cHANPs; c) PSD of PEG-cHANPs in the optimized condition of SH/VS = 0.0011; d) SEM image of PEG-cHANPs in the optimized condition of SH/VS = 0.0011.

It is worth noticing that the similar SH/VS ratios of 0.0011 and 0.0009 have a relevant difference that is due to the difference between the substitution degree of the compounds. The thiolated Hyaluronic Acid (HA-SH) has a very low substitution degree of only 5%, while the PEG-VS is linearly functionalized (100%). This significant chemical difference produces a great change in the concentration of the injected total solution, even though there is only a small variation in the SH/VS ratios. It is particularly true in a microfluidic environment where a slight change in the concentration could promote a relevant change in the fluidodynamics and, in our particular case, in the thermodynamics of the nanoprecipitation. In details, the SH/VS ratio of 0.0009 is obtained with HA-SH concentration constant at 0.1% w/V and PEG-VS concentration of 0.223% w/v, in greater excess of PEG-VS with respect to the concentration used for SH/VS of 0.0011 (0.18% w/V). As a consequence, we observed polydisperse precipitation due to the formation of unstable PEG-VS substructures. The optimized condition is found at SH/VS value of 0.0011 that is three orders of magnitude lower than the literature reference. FTIR analyses were performed to confirm the occurrence of the crosslinking

reaction. Spectra presented in Figure 12b revealed that PEG-cHANPs do not exhibit the signal for double bond C = C observed for PEG-VS at 750 cm-1, due to the Michael addition reaction with thiol groups of HA. In addition, the successful occurrence of the reaction is confirmed by the peak at 600 cm-1 corresponding to C-S bond stretching.

In these conditions, a uniform population of spherical particles with a mean dimension of 140 nm is obtained, Figure 1.12 c and d.

Furthermore, the effect of temperature on crosslinking reaction occurrence was performed. Two different strategies, Low Temperature (LT) and Room Temperature (RT) were compared. In the first case, the temperature of the injected polymer solution was kept at 4 °C both during the preparation step and injection; in the second one, both the mixing and processing of the solution occurred at room temperature. For all cases, no temperature control on the chip was present. However, we assumed that, for the RT strategy, the mixing Temperature in the main channel is constant while for the LT strategy a Temperature gradient moving toward the RT is obtained, achieving the favorable conditions for the promotion of the crosslinking reaction. It is worthy of notice that, also at RT, the solvent solution was processed with no difficulties, meaning that the crosslinking is not completed before injection. However, results show that in this case, a film of material is formed, and the particle formation is impaired, Figure 1.13. When the temperature is kept at 4 °C a uniform population of nanoparticles is obtained. These observations reveal that Temperature control is necessary to slow down the reaction rate and to control its occurrence in the device. To study the effect of the Temperature, all trials are conducted in a standard condition of 30 µL/min for the middle channel and 110 µL/min for the side ones.

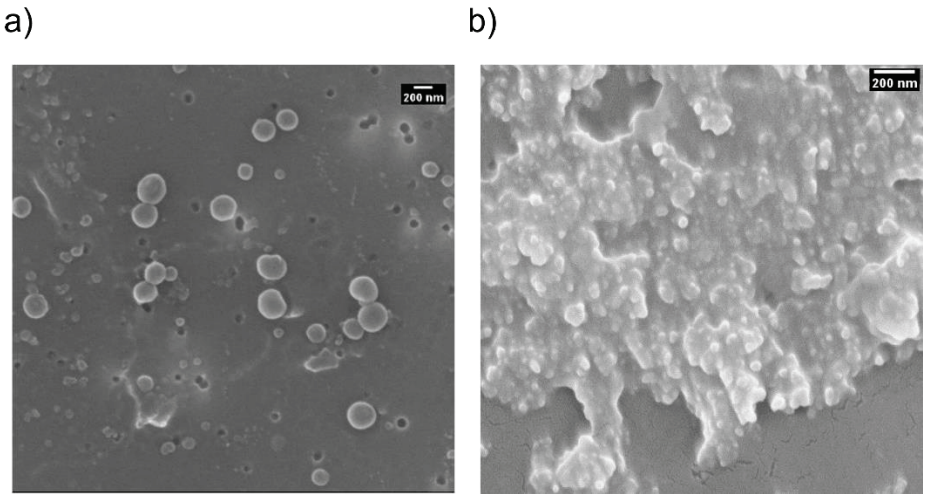

Figure 1.13 – Effect of solvent phase injection temperature. A) Low Temperature strategy with solvent phase injection at 4°C; b) Room temperature strategy with solvent phase injected at RT.

Once standard conditions for particle production were defined, Gd-DTPA was encapsulated by dissolving it in the solvent solution at a concentration of 0.1%w/V. ICP-MS analyses reveal that 110 µM of Gd-DTPA are encapsulated in PEG-cHANPs with an EE% of 60%. However, despite the high encapsulation efficiency, the measurement of PEG-cHANPs relaxivity compared to the relaxivity of free Gd-DTPA at the same concentration revealed an Hydrodenticity boosting of only 1,22 fold.

Subsequently, PEG-cHANPs coloaded with Gd-DTPA and ATTO 488 were produced by adding Gd-DTPA and ATTO488 in the solvent solution at a concentration of 0.1% w/V and 10 nmol/mL, respectively as described in the dedicated method section. With respect to Gd-loaded PEG-cHANPs, Gd-DTPA EE% decreases down to 25% and ATTO 488 EE% was quantified as 60%. Despite the reduction in the encapsulation efficiency, the co-encapsulation of the water-soluble fluorophore allowed to improve the Hydrodenticity effect from a boosting of 1,22 fold to a 5 times boosting of co-loaded PEG-cHANPs with a longitudinal relaxivity r_1 = 15.8 $mM^{-1}s^{-1}$, Figure 14b. This effect can be attributed to the increased number of water molecules brought in the polymer network needed to solvate the water soluble dye molecules. Also in this case, fluorescent imaging was performed to localize the dye molecules inside nanoparticles, Figure 14a.

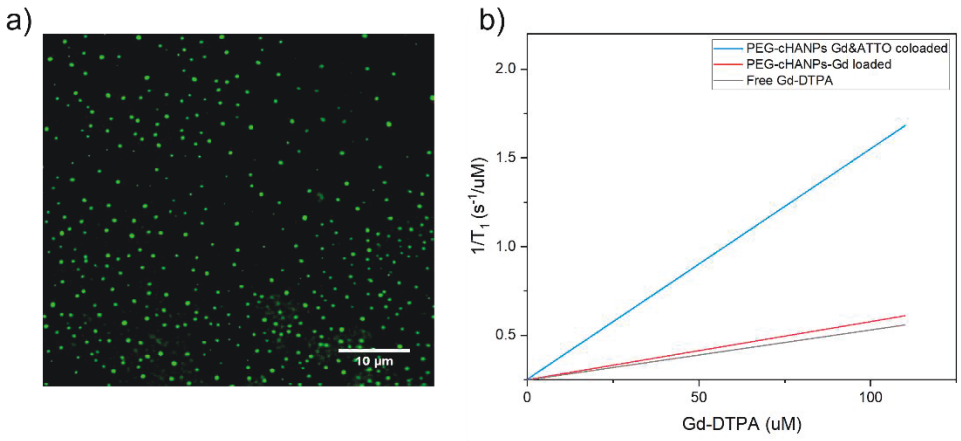

Figure 14 – Characterization of PEG-cHANPs co-encapsulation ability and Hydrodenticity property. a) Fluorescent imaging of co-loaded PEG-cHANPs; b) Comparison of relaxivity of Gd-loaded and co-loaded cHANPs and free Gd-DTPA for Hydrodenticity effect quantification

In the attempt of studying the effect of a different PEG conformation on the two polymer coprecipitation and on the crosslinking rection, the linear mPEG-VS was substituted with a four-arms one, increasing the number of -VS moieties available for crosslinking reaction of four times. Taking advantage of the optimal functional group ratio obtained from previous investigation (SH/VS = 0.0011), the total polymer concentration was adjusted accordingly. In a first attempt, a population of aggregated particles was obtained, thus the colloidal stability was not achieved suggesting that either the polymer simultaneous precipitation or the crosslinking reaction occurred. For this reason, in the same operative conditions, NPs were collected and let complete the reaction at 37°C for 12h

prior purification to promote reaction occurrence, as suggested from literature[36-38]. In this way, a uniform population of spherical particles was achieved. FTIR measurement were performed to confirm the occurrence of the crosslinking reaction, Figure 1.15a. As before, PEG-cHANPs do not exhibit the signal for double bond C = C observed for PEG-VS at 750 cm^{-1}, due to the Michael addition reaction with thiol groups of HA. The successful occurrence of the reaction is additionally confirmed by the peak at 600 cm^{-1} corresponding to C-S bond stretching. Despite the achievement of a stable particle population, measurement of the relaxivity of 4 arms PEG-cHANPs lead to a more modest increase of the relaxivity boosting of 3-fold, with a measured longitudinal relaxivity r1 = 8.32 $mM^{-1}s^{-1}$, as reported in Figure 1.15b.

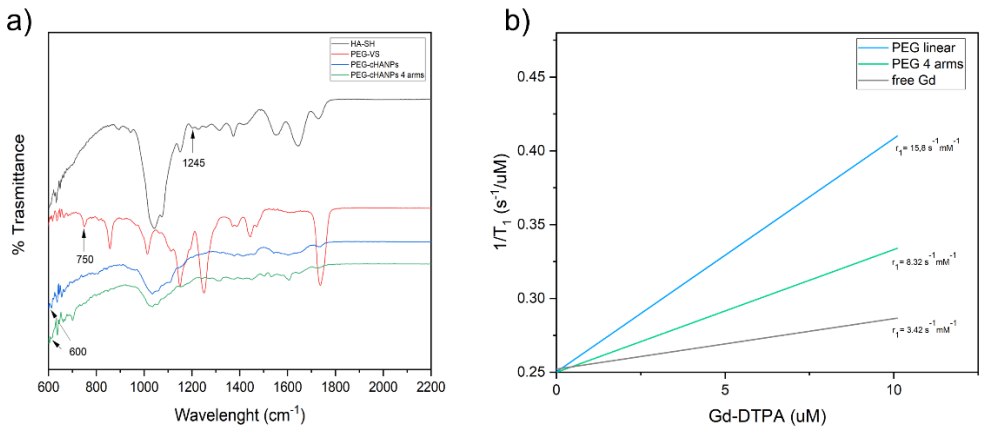

Figure 1.15 – Charcaterization of the impact of 4-arms PEG on PEG-cHANPs crosslinking. A) FTIR spectra of 4-arms PEG-cHANPs; b) Comparison of relaxivity of linear PEG-cHANPs and 4 arms PEG-cHANPs with free Gd-DTPA for quantification of 4 arms PEG on Hydrodenticity

I.IV. Conclusions

Exploiting the fine control offered by microfluidic-based HFF, different HA-based NPs were produced by nanoprecipitation. cHANPs and HW-cHANPs were successfully produced as a uniform particle population with a mean dimeter lower than 150 nm allowing to investigate the role of the polymer molecular weight on nanoprecipitation process and active agent encapsulation, as well as control of hydrogel structure and crosslinking and thus Hydrodenticity. Moreover, the molecule-by-molecule control offered by microfluidics was exploited to implement a nucleophilic addition, the Michael addition reaction, to achieve simultaneous particle PEGylation and crosslinking with strongly reduced total polymer concentration and functional group ratio with respect to traditional batch applications. The encapsulation of different active agents moving from Gd-DTPA, one of the most commonly used MRI CA in clinical practice, to standard dye for optical imaging (ATTO488 and ATTO 633) and Irinotecan, an FDA approved drug in the standard of care for the treatment of many solid tumors,

was explored. A direct comparison of different NPs characteristic as well as multiple agent co-loading on active agent EE% was conducted. Finally, the impact of different NP architectures and hydrogel networks on the property of Hydrodenticity was assessed. Overall, by means of a single, highly reliable, scalable and cost-effective microfluidic production process, it was possible to develop a library of fully biocompatible nanoparticles, with well-defined but very different designs, investigating the role that each component has in the determination of the nanoparticle synthetic identity.

I.V. References

1 Collins, M. N. & Birkinshaw, C. Physical properties of crosslinked hyaluronic acid hydrogels. *Journal of Materials Science-Materials in Medicine* **19**, 3335-3343, doi:10.1007/s10856-008-3476-4 (2008).

2 Choi, K. Y. *et al.* Smart Nanocarrier Based on PEGylated Hyaluronic Acid for Cancer Therapy. *Acs Nano* **5**, 8591-8599, doi:10.1021/nn202070n (2011).

3 Xu, X., Jha, A. K., Harrington, D. A., Farach-Carson, M. C. & Jia, X. Q. Hyaluronic acid-based hydrogels: from a natural polysaccharide to complex networks. *Soft Matter* **8**, 3280-3294, doi:10.1039/c2sm06463d (2012).

4 Bicudo, R. C. S. & Santana, M. H. A. Production of hyaluronic acid (HA) nanoparticles by a continuous process inside microchannels: Effects of non-solvents, organic phase flow rate, and HA concentration. *Chemical Engineering Science* **84**, 134-141, doi:10.1016/j.ces.2012.08.010 (2012).

5 Russo, M., Bevilacqua, P., Netti, P. A. & Torino, E. A Microfluidic Platform to design crosslinked Hyaluronic Acid Nanoparticles (cHANPs) for enhanced MRI. *Scientific Reports* **6**, doi:10.1038/srep37906 (2016).

6 Almalik, A. *et al.* Hyaluronic Acid Coated Chitosan Nanoparticles Reduced the Immunogenicity of the Formed Protein Corona. *Scientific Reports* **7**, doi:10.1038/s41598-017-10836-7 (2017).

7 Kim, Y. & Kumar, S. CD44-Mediated Adhesion to Hyaluronic Acid Contributes to Mechanosensing and Invasive Motility. *Molecular Cancer Research* **12**, 1416-1429, doi:10.1158/1541-7786.mcr-13-0629 (2014).

8 Bayer, I. S. Hyaluronic Acid and Controlled Release: A Review. *Molecules* **25**, doi:10.3390/molecules25112649 (2020).

9 Zhang, P., Sun, F., Liu, S. J. & Jiang, S. Y. Anti-PEG antibodies in the clinic: Current issues and beyond PEGylation. *Journal of Controlled Release* **244**, 184-193, doi:10.1016/j.jconrel.2016.06.040 (2016).

10 Gulati, N. M., Stewart, P. L. & Steinmetz, N. F. Bioinspired Shielding Strategies for Nanoparticle Drug Delivery Applications. *Molecular Pharmaceutics* **15**, 2900-2909, doi:10.1021/acs.molpharmaceut.8b00292 (2018).

11 Ghosh, K. Biocompatibility of hyaluronic acid: From cell recognition to therapeutic applications. *Natural-Based Polymers for Biomedical Applications*, 716-737, doi:10.1533/9781845694814.6.716 (2008).

12 Shimojo, A. A. M., Pires, A. M. B., Lichy, R. & Santana, M. H. A. The Performance of Crosslinking with Divinyl Sulfone as Controlled by the Interplay Between the Chemical Modification and Conformation of Hyaluronic Acid. *Journal of the Brazilian Chemical Society* **26**, 506-512, doi:10.5935/0103-5053.20150003 (2015).

13 Russo, M., Ponsiglione, A. M., Forte, E., Netti, P. A. & Torino, E. Hydrodenticity to enhance relaxivity of gadolinium-DTPA within crosslinked hyaluronic acid nanoparticles. *Nanomedicine* **12**, 2199-2210, doi:10.2217/nnm-2017-0098 (2017).

14 Russo, M. *et al.* PEGylated crosslinked hyaluronic acid nanoparticles designed through a microfluidic platform for nanomedicine. *Nanomedicine* **12**, 2211-2222, doi:10.2217/nnm-2017-0103 (2017).

15 De Sarno, F. *et al.* Water-Mediated Nanostructures for Enhanced MRI: Impact of Water Dynamics on Relaxometric Properties of Gd-DTPA. *Theranostics* **9**, 1809-1824, doi:10.7150/thno.27313 (2019).
16 Mora-Huertas, C. E., Fessi, H. & Elaissari, A. Polymer-based nanocapsules for drug delivery. *International Journal of Pharmaceutics* **385**, 113-142, doi:10.1016/j.ijpharm.2009.10.018 (2010).
17 Dhand, C. *et al.* Methods and strategies for the synthesis of diverse nanoparticles and their applications: a comprehensive overview. *Rsc Advances* **5**, 105003-105037, doi:10.1039/c5ra19388e (2015).
18 Hornig, S., Heinze, T., Becer, C. R. & Schubert, U. S. Synthetic polymeric nanoparticles by nanoprecipitation. *Journal of Materials Chemistry* **19**, 3838-3840, doi:10.1039/b906556n (2009).
19 Alshamsan, A. Nanoprecipitation is more efficient than emulsion solvent evaporation method to encapsulate cucurbitacin I in PLGA nanoparticles. *Saudi Pharmaceutical Journal* **22**, 219-222, doi:10.1016/j.jsps.2013.12.002 (2014).
20 Khan, S. A. & Schneider, M. Improvement of Nanoprecipitation Technique for Preparation of Gelatin Nanoparticles and Potential Macromolecular Drug Loading. *Macromolecular Bioscience* **13**, 455-463, doi:10.1002/mabi.201200382 (2013).
21 Damiati, S., Kompella, U. B., Damiati, S. A. & Kodzius, R. Microfluidic Devices for Drug Delivery Systems and Drug Screening. *Genes* **9**, doi:10.3390/genes9020103 (2018).
22 Capretto, L., Carugo, D., Mazzitelli, S., Nastruzzi, C. & Zhang, X. L. Microfluidic and lab-on-a-chip preparation routes for organic nanoparticles and vesicular systems for nanomedicine applications. *Advanced Drug Delivery Reviews* **65**, 1496-1532, doi:10.1016/j.addr.2013.08.002 (2013).
23 Fontana, F., Ferreira, M. P. A., Correia, A., Hirvonen, J. & Santos, H. A. Microfluidics as a cutting-edge technique for drug delivery applications. *Journal of Drug Delivery Science and Technology* **34**, 76-87, doi:10.1016/j.jddst.2016.01.010 (2016).
24 Liu, D. F., Zhang, H. B., Fontana, F., Hirvonen, J. T. & Santos, H. A. Microfluidic-assisted fabrication of carriers for controlled drug delivery. *Lab on a Chip* **17**, 1856-1883, doi:10.1039/c7lc00242d (2017).
25 Elvira, K. S., Solvas, X. C. I., Wootton, R. C. R. & deMello, A. J. The past, present and potential for microfluidic reactor technology in chemical synthesis. *Nature Chemistry* **5**, 905-915, doi:10.1038/nchem.1753 (2013).
26 Valencia, P. M., Farokhzad, O. C., Karnik, R. & Langer, R. Microfluidic technologies for accelerating the clinical translation of nanoparticles. *Nature Nanotechnology* **7**, 623-629, doi:10.1038/nnano.2012.168 (2012).
27 Valencia, P. M. *et al.* Microfluidic Platform for Combinatorial Synthesis and Optimization of Targeted Nanoparticles for Cancer Therapy. *Acs Nano* **7**, 10671-10680, doi:10.1021/nn403370e (2013).
28 Jambovane, S. R. *et al.* Continuous, One-pot Synthesis and Post-Synthetic Modification of NanoMOFs Using Droplet Nanoreactors. *Scientific Reports* **6**, doi:10.1038/srep36657 (2016).
29 Liu, D. F., Zhang, H. B., Fontana, F., Hirvonen, J. T. & Santos, H. A. Current developments and applications of microfluidic technology toward clinical translation of nanomedicines. *Advanced Drug Delivery Reviews* **128**, 54-83, doi:10.1016/j.addr.2017.08.003 (2018).
30 Ding, S. K., Anton, N., Vandamme, T. F. & Serra, C. A. Microfluidic nanoprecipitation systems for preparing pure drug or polymeric drug loaded nanoparticles: an overview.

Expert Opinion on Drug Delivery **13**, 1447-1460, doi:10.1080/17425247.2016.1193151 (2016).
31 Karnik, R. *et al.* Microfluidic platform for controlled synthesis of polymeric nanoparticles. *Nano Letters* **8**, 2906-2912, doi:10.1021/nl801736q (2008).
32 Xu, J. *et al.* Controllable Microfluidic Production of Drug-Loaded PLGA Nanoparticles Using Partially Water-Miscible Mixed Solvent Microdroplets as a Precursor. *Scientific Reports* **7**, doi:10.1038/s41598-017-05184-5 (2017).
33 Ji, C. X., Ju, S., Zhang, D. Q. & Qiang, J. W. Nanomedicine Based N-Trimethyl Chitosan Entangled Solid Lipid Nanoparticle Loaded with Irinotecan to Enhance the Therapeutic Efficacy in Esophageal Cancer Cells. *Journal of Biomaterials and Tissue Engineering* **8**, 1195-1200, doi:10.1166/jbt.2018.1846 (2018).
34 Taghizadehghalehjoughi, A. *et al.* Effect of metformin/irinotecan-loaded poly-lactic-co-glycolic acid nanoparticles on glioblastoma: in vitro and in vivo studies. *Nanomedicine* **13**, 1595-1606, doi:10.2217/nnm-2017-0386 (2018).
35 di Polidoro, A. C. *et al.* Theranostic Design of Angiopep-2 Conjugated Hyaluronic Acid Nanoparticles (Thera-ANG-cHANPs) for Dual Targeting and Boosted Imaging of Glioma Cells. *Cancers* **13**, doi:10.3390/cancers13030503 (2021).
36 Jin, R. *et al.* Synthesis and characterization of hyaluronic acid-poly(ethylene glycol) hydrogels via Michael addition: An injectable biomaterial for cartilage repair. *Acta Biomaterialia* **6**, 1968-1977, doi:10.1016/j.actbio.2009.12.024 (2010).
37 Dubbini, A. *et al.* Injectable hyaluronic acid/PEG-p(HPMAm-lac)-based hydrogels dually cross-linked by thermal gelling and Michael addition. *European Polymer Journal* **72**, 423-437, doi:10.1016/j.eurpolymj.2015.07.036 (2015).
38 Sabbieti, M. G. *et al.* In vivo biocompatibility of p(HPMAm-lac)-PEG hydrogels hybridized with hyaluronan. *Journal of Tissue Engineering and Regenerative Medicine* **11**, 3056-3067, doi:10.1002/term.2207 (2017).

II. CHAPTER 2 –CELL-PARTICLE INTERFACE: DEFINITION OF NANOPARTICLE BIOLOGIC IDENTITY AND IMPACT ON CELL-PARTICLE INTERACTION

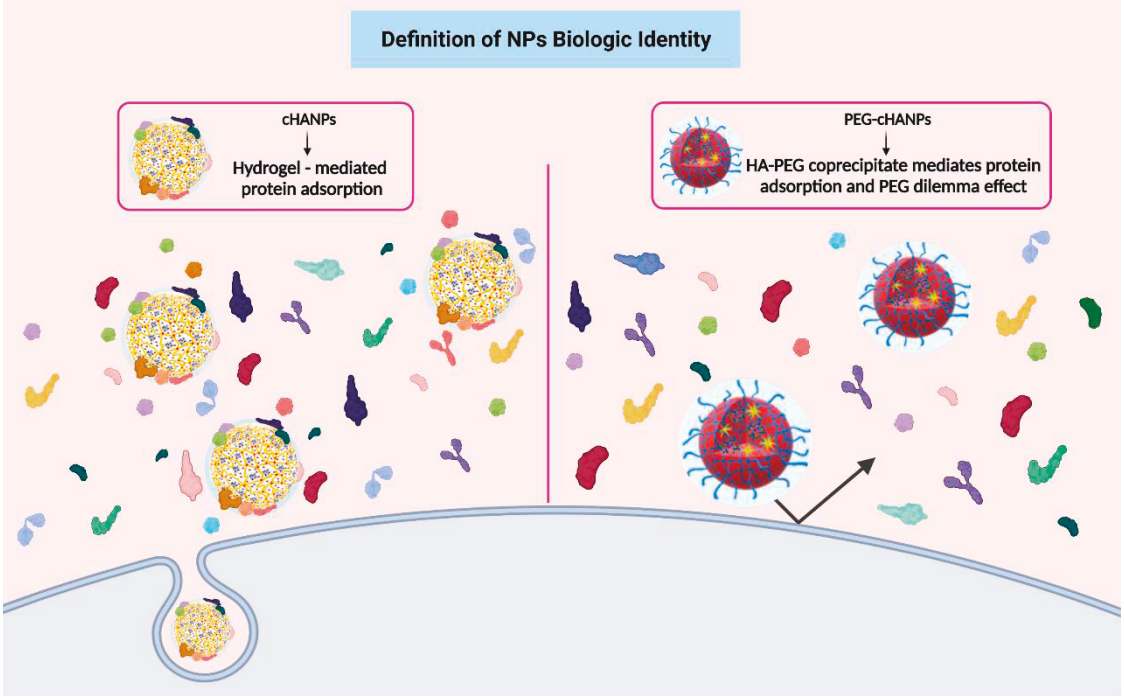

Graphical Abstract Chapter 2 – Study of the impact of material-mediated protein corona on cell-particle interface. Stability of hydrogel-based nanoparticles in differently composed biological and evaluation of the PEG-dilemma effect.

II.I. Background

Among the factors negatively impacting the clinical translation of nanomedicines, the adsorption of plasma proteins on the surface of nanoparticles (NPs) plays a major role, determining only 0.7% of nanformulations successfully interacting with their biological target being able to exploit the expected diagnostic or therapeutic function[1]. Indeed, the protein corona (PC) defines the nanocarrier biological identity, "masks" its synthetic identity, altering its surface properties and favoring the capture by macrophages and other cells of the reticuloendothelial system (RES)[2], in the end accelerating its body clearance[3]. The phagocytic fate of synthetic particles is influenced by surface functionalization, in addition to their size, surface charge, shape and mechanical rigidity[4]. Bertrand and collegues[2], recently demonstrated that NP early clearance due to RES capture can be efficiently tackled by modulating the hydrophilicity of the surface, regardless the physicochemical properties of the nanocarrier. In this regard, different strategies involving NP surface modification have been developed and designed over years[5-7]. PEGylation has revealed to be among the most promising alternatives, being widely explored in literature[8-11] and employed in successful clinical formulations. It is a pharmaceutical technology consisting of the covalent or non-covalent bonding of polyethylene

glycol (PEG) to therapeutic molecules or drug delivery nanosystems. Because of its hydrophilicity, PEG creates a hydrated layer at the surface of NPs, inhibits – or drastically reduces – the adsorption of proteins and complements normally present in biological fluids, in this way reducing recognition by cells of the RES[9]. This property is well-known as stealth effect and can be exploited to improve biodistribution of engineered NPs in human body[5], allowing them to interact with their biological target and perform the functions they were designed to.

PEG chains of different MW and assembly (e.g. linear chains and brushes), and more importantly different superficial PEG densities, have shown to determine different extent of mitigation of opsonization and early clearence. In particular, Pozzi et al.[10], demonstrated for a liposomal formulation, that PEG chains over 5000 Da tend to fold on the surface of NPs interacting by a short-range Van der Waals attractions and interchain hydrogen bonding, causing chain entanglement, inhomogeneous PEG coating and less efficient stealth protection. Differently, Bertrand et al.[2], demonstrated that 5000 Da PEG on PLGA NPs at a density of 20 chains/100nm^2 efficiently prolonged circulation times.

Despite the great promise of PEGylation in improving the pharmacokinetics (PK) of pharmaceuticals, increasing evidence that demonstrate the immugenicity of PEG both in animals and in humans are arising[12,13]. Thai Thanh Hoang Thi et al.[12] extensively reviewed clinical studies evidencing the presence of anti-PEG M-immunoglobulins (IgM) in mouse and human plasma, contradicting the claim of PEG non-immunogenicity. Their appearance in plasma has been recently found to cause the so-called accelerated blood clearence (ABC) of PEGylated products which contrasting the PEG stealth property, drastically reduces their circulation time. ABC effect has been demonstrated to be strongly influenced by the frequency of administration of PEGylated formulations. Indeed, Li et al.[14], reported that when an interval of 7 days between two subsequent intravenous injections of pegylated liposomal topotecan occurred, a reduction of about 95% in the circulation time of the second dosage was observed. The authors attribute this effect to the typical time scale of appearance of anti-PEG IgM of 3-4 days upon administration causing ABC of pegylated liposomes. Several clinical reports, correlate this effect with loss of therapeutic efficacy and increase in adverse effects of the formulation, effect which is thought to be relevant for the whole half-life of anti-PEG IgM which is of about 21 days[14,15]. Interestingly, in a clinical study of 2016, Yung et al.[16] detected pre-existing anti-PEG IgM in the serum of 70% of untreated patients, whose presence was attributed to the widespread use of PEG in pharmaceutical and cosmetic industry.

Although many studies have focused on the role that PEG has in NP opsonization and on the interaction between PEG and the immune system, there is another important factor contributing to limit the potential of PEG in improving drug PK that is, however, less explored in literature. Known as PEG-dilemma, it refers to the negative impact that the interface PEG-protein corona has on the

interaction of the Pegylated nanomedicine with its target cells, despite the increased circulation time. The reason is the formation of a water hydrated layer acting as a barrier between the pegylated system and the cell membrane.

As clear from the previous considerations, the need for alternatives to PEG able to efficiently prevent protein corona formation, prolong nanoformulation circulation time and promote their interaction with the biological target is still unmet. Among the most promising candidates there is hyaluronic acid (HA) which, as highly hydrophilic and naturally occurring polymer of the ECM owns comparable shielding to PEG, non-immunogenicity, biodegradability, and in some cases intrinsic targeting capabilities[17]. Indeed, as already stated in the previous chapter, HA is the natural substrate of CD44 receptors overexpressed in inflammation-based diseases such as cancer.

In this framework, a comparison of cHANPs and PEG-cHANPs colloidal stability in biological fluids and the investigation of particle properties modifications following to serum exposure, are performed. As model of the impact of surface hydrophobicity on protein adsorption, a commercial model of polystyrene NPs is used. A morphological analysis to visualize PC on NP surface and determine its impact on NP morphology is conducted. In addition, the impact that the absorbed corona has on the uptake by target cells is investigated, evaluating the possible advantages of a coprecipitated matrix of PEG and HA (PEG-cHANPs) in ameliorating the effects of PEG-dilemma. Finally, a different NP design involving cHANPs surface functionalization with a pegylated, custom made zwitterionic compound (Zwit-cHANPs) was evaluated for its ability of modulating particle uptake by cells.

II.II. Experimental Section

II.II.I. Materials

ATTO 488 MW 804 g/mol (Ex/Em 488/520) and ATTO 633 MW 652 g/mol (Ex/Em 633/655), dulbecco Modified Eagle Medium high glucose (DMEM), Fetal Bovine Serum (FBS), Phosphate Buffer Saline (PBS), Trypsin, Penicillin/Streptomycin, L-glutamine, Human Serum Albumin (HSA) for cell culture and in vitro study were purchased by Sigma Aldrich. For cell culture U-87 MG cell line (passage 15-36) was purchased from ATCC. Polystyrene NPs (PS NPs) were purchased from Sigma Aldrich. Zwitterion PEG—SH+-(CH2)2—COO- (MW = 10000 Da) was customly produced at BOCSCI Inc. (New York, USA). Crosslinked hyaluronic acid nanoparticles (cHANPs) and Polyethylene glycol crosslinked hyaluronic acid nanoparticles (PEG-cHANPs) were synthesized as discussed in the previous chapter.

II.II.II. Determination of particle stability in biological sera

NP suspensions were prepared by diluting the concentrated NP stock solution in DMEM without serum (serum free medium, SFM) or supplemented with different % of sera (10% V/V FBS or 20% w/V). Unbound and weakly bound soft-corona proteins were removed from the protein-NP suspension by centrifugation in Corning Spin-x Concentrators (MWCO 50 KDa) (Corning®) (3000 rpm, 10 min, 4°C) for cHANPs and PEG-cHANPs, and by UltraCentrifugation (70000rpm, 30min, 4°C) for PS NPs. Concentration of hard protein corona adsorbed on NPs surface was determined using a bicinchoninic acid (BCA) assay.

The particle size, polydispersity index (PDI), and zeta-potential (ZP) of PS NPs, cHANPs and PEG-cHANPs in different serum condition were measured using the dynamic light scattering (DLS) technique. NPs were dispersed in 1 mL of double distilled deionized water at a concentration of 20 µg/mL and measurements were performed using Malvern Zetasizer Nano ZS90 (Malvern Instruments, Malvern, UK) at 37°C. All measurements were replicated three times and reported results are the mean value of all measurements.

Tecnai FEI® transmission electron Microscope was used to evaluate NPs stability and architecture after protein corona adsorption. Sample preparation consisted in placing 10 µL of NPs suspension on a Formvar/Carbon 200 mesh Cu Agar® filter. After drying overnight under hood, samples were ready to be observed.

II.II.III. Quantification of nanoparticle uptake by circulating macrophages and target cells: flow cytometry measurements

After assessing the morphological stability of the particles at serum exposure, the role of PEGylation in preventing the capture by circulating macrophages was assessed in vitro. Flow cytometry measurements were used to quantify and compare the uptake of co-loaded cHANPs and PEG-cHANPs by J774 as a well-established cell model of circulating macrophages. J774 cells were seeded in 96-well plates (Falcon®) at a density of 0.5 x 10^5 cells/well and incubated with culture medium (DMEM, FBS 10% V/V, L-glutamine 1% V/V and penicillin/streptomycin 1% V/V) for 24 hours prior the addition of NPs (50 µg/mL). Cell incubated with medium without NPs are used as negative control. At the end of any time point, medium was removed, and samples were washed three times with PBS (1x) to ensure removal of non-internalized nanoparticles from the outer cell membrane. Cells were then trypsinized for 5 min at 37°C. After cell detachment confirmation at optical microscope, complete medium was added to neutralize trypsin and cells were transferred in polystyrene round-bottomed tubes (Falcon®) to be immediately analyzed by flow cytometry.

The very same procedure was used to perform flow cytometry analyses to quantitatively measure the uptake of nanoparticles (PS NPs, cHANPs and PEG-cHANPs) in different serum conditions by U87 cells, representing a possible cellular target[18].

U87 cells were seeded in 48-well plates (Falcon®) at a density of 0.5 x 10^5 cells/well and incubated with culture medium (DMEM, FBS 10% V/V, L-glutamine 1% V/V and penicillin/streptomycin 1% V/V) for 24 hours prior the addition of NPs to assure cell attachment. Afterwards, cells were incubated with medium at two different sera conditions (10% FBS and 20% HSA) supplemented with PS NPs, cHANPs or PEG-cHANPs (20 µg/mL) for 1, 2, 4, 24 and 48 hours. Cells supplemented with complete medium (DMEM, FBS 10% V/V, L-glutamine 1% V/V and penicillin/streptomycin 1% V/V) without NPs were used as negative control. In both cases, forward scattering (FSC), side scattering (SSC) and fluorescence intensity (FI %) were measured using a BD FACSCelesta™ (BD®) flow cytometer to obtain information about cell viability and quantify nanoparticle internalization, respectively. bA 488nm or 633nm laser wavelength was used to excite NPs fluorescence collected using the 595–660 nm spectral detection channel. Results are reported as the mean of the distribution of cell fluorescence intensity obtained by measuring 10000 events averaged between three independent replicas divided by the mean fluorescence of three replicas of control. Error bars correspond to the standard deviation between replicas. Data analysis was performed using CytoFlow software.

II.II.IV. Zwit cHANPs production

The custom made zwitterionic compound was composed of a PEG moiety conjugated to a zwitterionic sequence PEG—SH+-(CH2)2—COO-. Zwit-cHANPs are produced by direct post-production contact of co-loaded cHANPs with a water solution of zwit at pH=8. As first step, cHANPs pH is modified from neutral to pH = 8 by NaOH and after 10 min stirring, zwit solution (1 mg/mL) is added and let interact for 2h upon wheel stirring. Zwit-cHANPs are then characterized for size, zeta potential and morphology by SEM and TEM.

II.II.V. Confocal Imaging for determination of NPs uptake

Optical fluorescent imaging is performed to study Zwit-cHANPs cellular localization. Cells are seeded at a density of 5x10^4 cells/well in 8 slide µ-well glass bottom (IBIDI® GMBH). After 24h, time to let cells adhere to the surface, medium supplied with Zwit-cHANPs (50 µg/mL) is added and incubated for 24h. Live cells are observed at Leica Microsystems TCS SP5 Laser

Scanning Confocal Microscope equipped with an incubator to keep the temperature at 37°C and CO_2 levels at 5%, with a 60x oil objective.

II.III. Results

II.III.I. Colloidal stability of hydrogel-based nanoparticles in biological sera

The first step was the assessment of NP colloidal stability at exposure to two different biological sera depending on NP surface chemistry. Hydrophilic cHANPs and PEG-cHANPs and hydrophobic PS NPs are exposed to FBS 10% V/V as a model of culture medium, which is the condition used in all *in-vitro* testes and HSA 20% w/V as a model of human plasma and compared to serum free medium (SFM) properties. DLS analyses were performed to measure mean size, polydispersity, and z-potential (ZP) of PS NPs, cHANPs and PEG-cHANPs in different serum conditions. Nanoparticles were incubated with 10% FBS V/V or 20% HSA w/V for 1h, a time scale chosen to allow the establishment of an equilibrium between serum dispersed and nanoparticle adsorbed proteins[3,19]. Excess of serum proteins and soft corona were removed prior measurement, as described in the dedicated method section. DLS measurement in Figure 2.1 reveal that PS NPs undergo a significant increase in mean size from 105 nm in SFM to 234.6 nm in FBS and 159,9 nm in HSA, and a relevant particle size distribution (PSD) broadening can be observed, as a result of hard protein corona formation. Differently, the hydrogel-based nanoparticles show a remarkably lower increase in mean size, both for cHANPs and PEG-cHANPs. This effect can be attributed to the well-known stealth property of highly hydrophilic polymer, that creating a hydrated layer on the surface of the particle, drastically reduces the absorption of plasma proteins.

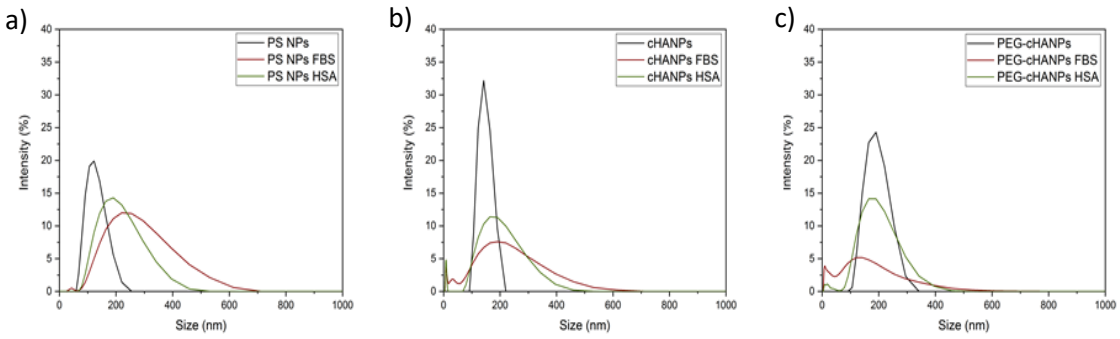

Figure 2.1 – Comparison of DLS measurement in SFM, FBS and HSA of a) PS NPs, b) cHANPs, c) PEG-cHANPs.

Comparing cHANPs and PEG-cHANPs, the latter show a lower increase in size, suggesting less affinity to FBS and HSA proteins than cHANPs because of the presence of coprecipitated PEG

chains in the structure of HA. In addition, a widening of the PSD observed for cHANPs couopled to the almost unchanged mean size, suggests a possible partial aggregation state. ZP values of all bare NPs decrease in absolute value after 1 hour of contact with different *sera*, as a confirmation of protein adsorption on NPs surface, Figure 2.2. However, this decrement is much more evident in PS NPs going from -17 mV to -9 mV, with respect to cHANPs and PEG-cHANPs which decreased from -13 mV to – 9 mV and from -11 mV to -9 mV, respectively. This confirms the improved colloidal stability of hydrogel nanoparticles with respect to the hydrophobic PS NPs.

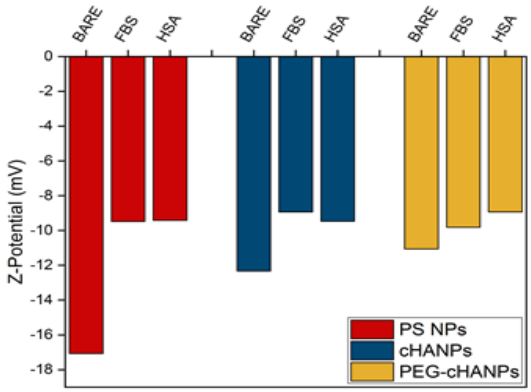

Figure 2.2 – Zeta potential measurements of PS NPs, cHANPs and PEG-cHANPs in SFM, FBS and HSA.

To assess NP morphological stability at adsorption of plasma proteins, TEM analyses were performed after NP exposure at different sera. Observations in figure 2.3 revealed the presence of a protein corona on the surface of all NPs in both serum conditions, which, as expected, is much more evident for PS NPs than for hydrogel NPs. In addition, cHANPs corona appears more compact than PEG-cHANPs one, especially in HSA, confirming the role of the coprecipitated PEG in the reduction of protein adsorption. Despite the presence of the corona, images demonstrate the structural and colloidal stability of all NP systems and confirm DLS results. TEM analyses also confirm that NPs size increase after protein corona formation is much more evident in PS NPs.

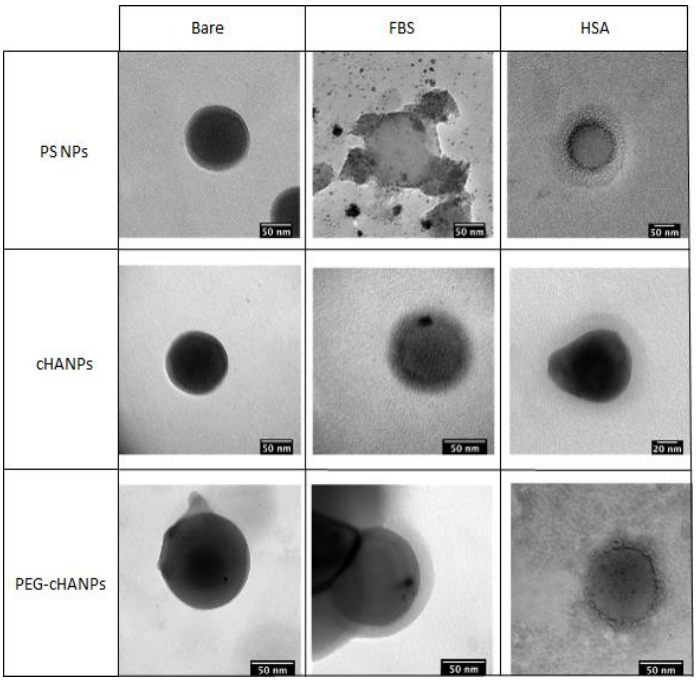

Figure 2.3 – TEM observation of PS NPs, cHANPs and PEG cHANPs bare, in FBS and HSA.

As a summary for direct comparison of all the results obtained for PS NPs, cHANPs and PEG-cHANPs in the three tested serum conditions are presented in Table 1.

Table 1 - Summary of DLS and ZP measurements for PS NPs, cHANPs and PEG-cHANPs in SFM, FBS and HSA

Particle Type	Serum Condition	Mean Size (nm)	ZP (mV)
PS NPs	SFM	105.673 ± 6.139	-17.067 ± 0.322
	FBS	234.605 ± 35.288	-9.480 ± 1.279
	HSA	159.959 ± 20.430	-9.427 ± 0.845
cHANPs	SFM	150.027 ± 13.832	-12.333 ± 1.102
	FBS	165.558 ± 46.349	-8.930 ± 0.648
	HSA	162.608 ± 49.489	-9.473 ± 1.244

	SFM	161.380 ± 15.626	-11.067 ± 0.873
PEG-cHANPs	FBS	175.554 ± 11.459	-9.813 ± 1.142
	HSA	185.736 ± 47.852	-8.937 ± 1.712

II.III.II. cHANPs and PEG-cHANPs uptake by circulating macrophages

After studying the role that hydrogels, and in particular PEG play in the reduction of protein adsorption on nanoparticle surface when in biological fluids, the impact that this reduced adsorption has on the uptake of circulating macrophages was assessed. For this reason, a flow cytometry analysis was conducted to quantify the amount of cHANPs and PEG-cHANPs captured by J774, a cellular murine model for circulating macrophages[20]. Results in Figure 2.4 show that, in a time span of 8h, which is the average circulation time expected both for cHANPs and PEG-cHANPs, NPs show a relatively low internalization by macrophages, with cHANPs being captured in a greater extent, especially for longer exposure times (i.e. 6h-8h). This result confirms that cHANPs bears partial stealth properties being HA a highly hydrophilic polymer, and that PEG of PEG-cHANPs acts as an effective antifouling agent, further reducing the capture of NPs by circulating macrophages.

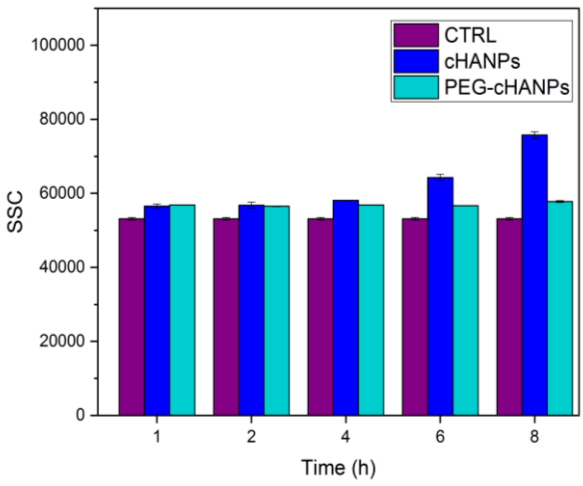

Figure 2.4 – Side scattering (SSC) measurement of J774 exposed to cHANPs and PEG-cHANPs (50 µg/mL) up to 8h as an indirect measure of particle internalization

II.III.III. Role of hydrogels in NPs-cell interaction with U87 as model of target cells

The second step was the investigation of the impact that the hydrated layer formed at the particle surface by PEG, which is responsible for proteins rejection in serum, has on the interaction that nanoparticles have with the target cells. Indeed, if on one side, i*n-vivo*, the reduction of protein adsorption mediated by PEG may result in increased circulation time because of the lower opsonization of the nanocarriers, on the other side, it is still unclear the impact that PEGylation has on the interaction with targets, as in the uptake by target tumor cells. This effect is known as PEG-dilemma and specifically it refers to the two important negative consequences characterizing the use of PEG as stealth material. Firstly, many authors reported the presence of anti-PEG antibodies in human blood samples contradicting the claim of PEG non-immunogenicity. Secondly, the presence of a hydrated layer at the surface of the particle constitutes a barrier to particle internalization by cells.

To investigate whether the PEG negatively impacts the interaction of NPs with target cells, we investigated *in-vitro* the role of the different surface chemistry (hydrophilic cHANPs and PEG cHANPs and hydrophobic PS NPs) in modulating the uptake by U87 cells, a well-established model of human glioma. Cells were incubated with cHANPs, PEG-cHANPs or PS NPs (50 µg/mL) up to 24h and the internalization of NPs in different serum conditions was compared. Results are presented as normalized fluorescent intensity as the ratio between the measured fluorescent intensity of cells exposed to different NP systems divided by the net fluorescence of the same volume of free NPs. The reason for that is the much higher fluorescent intensity characterizing the PS NPs as standard, commercially available NPs. If not accounted, it would not be possible to perform a direct comparison of the achieved results.

As reported in figure 2.5, the uptake of hydrogel particles is less affected by protein adsorption in both sera. This can be easily observed by looking at the preserved uptake kinetic of both cHANPs and PEG-cHANPs in both sera. cHANPs and PEG-cHANPs are uptaken much faster than the hydrophobic PS NPs reaching the maximum of internalization already after 2h of contact. Moreover, PS NP uptake requires 24h to reach relevant internalization levels in both in SFM and serum-exposed conditions and, with particular regard to HSA serum condition, the 24h uptake result strongly hindered by protein absorption or loss of particle colloidal stability. Differently, FBS was determining an increased uptake of all NPs with, however, an increased standard deviation between replicas which is a probable symptom of uneven protein adsorption and unspecific interaction of particles with target cells. As expected, PEG-cHANPs are the NPs less affected by the presence of proteins in the serum.

Surprisingly, they do not show a significantly decreased uptake with respect to cHANPs as was expected. This effect might be attributed to the structural characteristic of the hydrogel matrix. Indeed, PEG-cHANPs are not constituted by a HA core covered by a PEG outer layer but by a coprecipitated HA-PEG matrix. This might have synergistically aided the stealth property of the HA, contributing to reduce protein adsorption and improve colloidal stability of the formulation and, at the same time, mitigate the PEG-dilemma effect, improving the interaction of PEG-cHANPs with target cells.

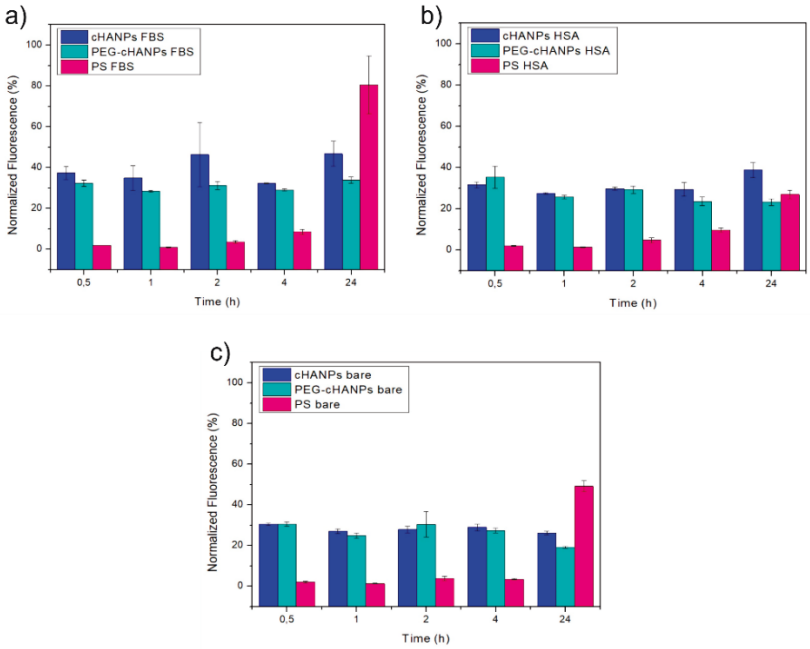

Figure 2.5 – Fluorescent intensity of U87 cells incubated with cHANPs, PEG-cHANPs and PS NPs (50 µg/mL) in a) FBS 10% V/V; b) HSA 20% w/V; c) SFM.

II.III.IV. Zwit-cHANPs role in mediating nanoparticle-cell interaction

To further investigate the role of superficial PEG in the preventing NPs uptake by target cells, a different design of cHANPs surface was investigated. Post-production, cHANPs surface was covered with a custom made pegylated-zwitterionic compound (PEG-Zwit). The contact was performed at pH = 8.5 to promote PEG-Zwit – cHANPs electrostatic interaction. Two different particle:zwit volumetric ratios (1:1 and 1:2) were explored starting from 1 mg/mL cHANPs and PEG-Zwit suspensions. Contact was performed for different time points, starting from 1h up to 24h. Zeta-potential measurements were performed as a measure of the masked surface, and thus of successful coverage. Results in figure 2.5a show that after exposure to alkaline pH, cHANPs ZP strongly decreases because of -COOH groups activation. At contact with PEG-zwit, cHANPs ZP starts increasing as a consequence of their electrostatic

interaction. ZP increase keeps constant over time for the lower particle:zwit ratio, symptom of a stable interaction. Differently, for the higher particle:zwit ratio, after 24h ZP decreases up to the initial highly negative value, indication of an inhomogeneous interaction. To further assess the superficial coverage, TEM observations were performed as shown in figure 2.5b and 2.5c.

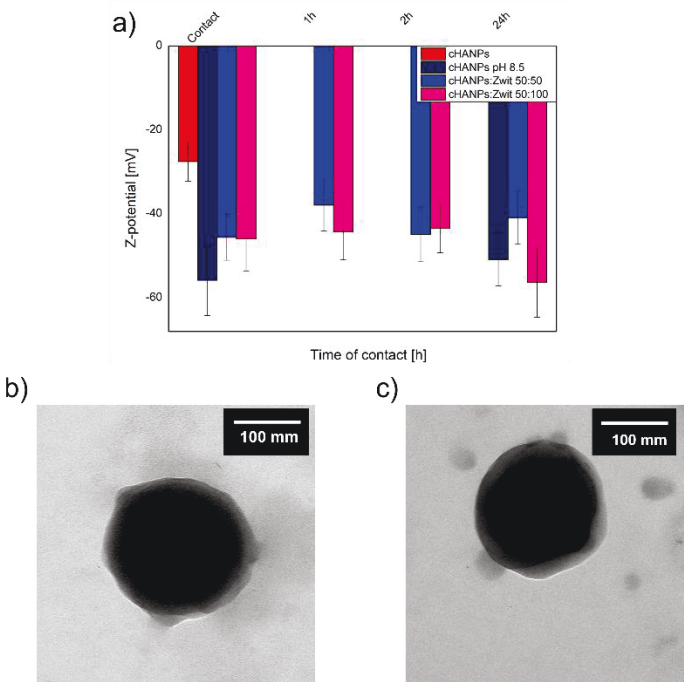

Figure 2.5 – Zwit cHANPs characterization. a) Zeta-potential measurement of cHANPs in contact with PEG-zwit at different volume ratios and time points; b) TEM image of Zwit-cHANPs after 2h of contact with the 1:1 particle:zwit ratio; c) TEM image of Zwit-cHANPs after 2h of contact with the 1:2 particle:zwit ratio

TEM images clearly reveal the presence of a shell of a different electron density on cHANPs surface, attributable to PEG-Zwit coverage. The main difference between the two observations is the presence of unreacted material in the background that in addition to the not stable ZP of the higher particle:zwit ratio, determined the setting of the optimized conditions for Zwit-cHANPs production to 1:1 volume ratio and 2h of contact.

After production, the impact that the different surface chemistry of Zwit-cHANPs has on cell-nanomaterial interaction was assessed by comparing the uptake of Zwit-cHANPs to the uptake of cHANPs by U87 cells cultured with FBS and measured by flow cytometry. Both SSC and Fluorescence intensity in Figure 2.6a and b show that Zwit cHANPs introduces a delay in the uptake of particles reaching the maximum of the internalization after 4h of contact, value reached in 2h from cHANPs. This result is confirmed both by SSC that, being a measure of the cell granularity is an indirect measurement of nanoparticle uptake, and by single cell fluorescence. SSC increases sharply already after 30 min of contact with cHANPs, while for Zwit-cHANPs it reaches the maximum only after 4h.

The same observation can be done for fluorescent intensity. The increase in the fluorescent value of Zwit-cHANPs at 1h of incubation is out of the internalization trend and might be attributed to the diffusion of the free fluorophore released by particles being a small free-diffusing molecule, as previously reported[18]. To confirm the internalization of NPs and locate them inside cell cytosol, a confocal observation of Zwit-cHANPs incubated cells was performed. Results in figure 2.6b clearly reveal a significant amount of internalized particles in cell cytoplasm after 24h of contact. The absence of a diffuse and homogeneous fluorescent patina in the culture medium exclude the presence of a significant amount of free dye, further confirming the stability of Zwit-cHANPs at surface coverage.

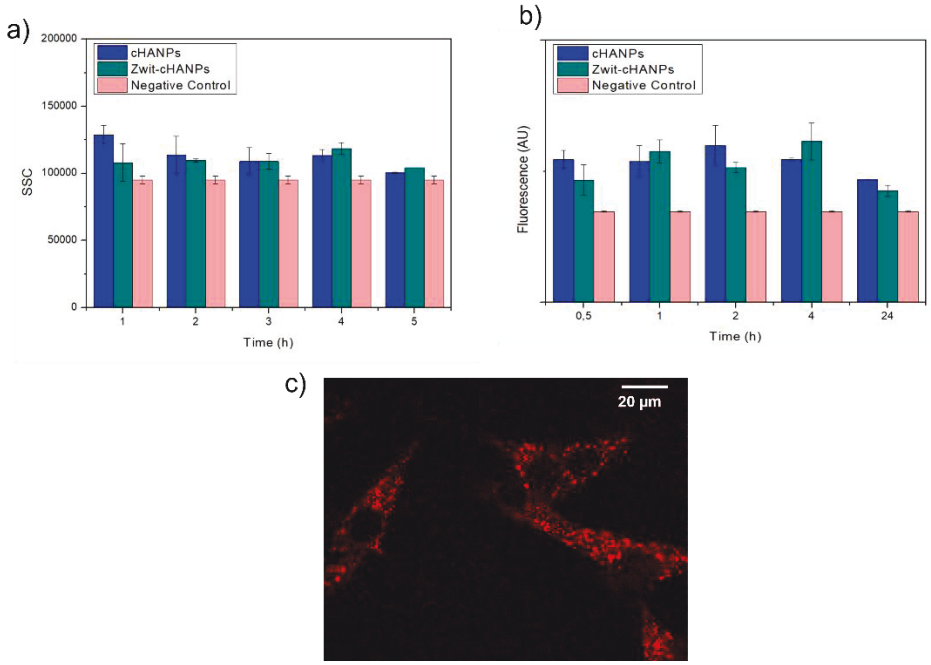

Figure 2.6 – Study of Zwit-cHANPs internalization by U87 cells. a) Side Scattering (SSC) and b) fluorescent intensity of U87 incubated with cHANPs and Zwit-cHANPs; c) Optical fluorescence imaging for the localization of Zwit-cHANPs in cell cytoplasm

II.IV. Conclusions

The relationship existing between the synthetic and the biological identity of cHANPs and PEG-cHANPs has been characterized. The role of specific design choices as the production of a coprecipitated PEG-HA matrix in both stealth properties and cellular particle uptake has been evaluated. A comparison with commercially available hydrophobic PS NPs was performed in order to assess the role of surface properties in the definition of nanoparticle biological identity and consequent impact on uptake by target cells. Results demonstrated that the hydrophilic surface of hydrogel-based nanoparticles contributed

significantly to preserve nanoparticle colloidal stability in biological serum, with small variations both in surface charge and mean hydrodynamic radius as well as particle morphology. cHANPs and PEG-cHANPs capture by a murine cell model of circulating macrophages in serum-containing medium was evaluated in order to assess the role of PEG in preventing RES capture when in blood circulation. Flow cytometry measurements revealed that HA of cHANPs exhibits a strong antifouling property with a significant particle uptake evident only after 6h of contact. The additional role of PEG determined the shift of the maximum uptake at 8h of contact, thus the convenience of its use need to be evaluated based on its impact on target cells uptake. U87 cells were used as a target cell model, being a widely used human glioma cellular model. Flow cytometry results showed that uptake of PS NPs is widely affected by serum, and particularly by HSA, determining a strong reduction in particle uptake probably due to aggregation state and loss of colloidal stability. Hydrogel particles demonstrated to be minimally impacted by the presence of serum as their uptake kinetic was basically unaffected with respect to SFM. Also, the comparison with a surface exposed PEG on Zwit-cHANPs demonstrated a much more evident hindering of nanoparticle uptake with respect to the coprecipitated matrix of PEG-cHANPs. However, further investigations of the pH-dependent charge switching of the zwitterion have to be performed, in order to understand if the switching to a positive charge in presence of an acidic pH (i.e. tumour microenvironment) might counterbalance this delay in the uptake due to PEG. This results all together demonstrated first that the synthetic identity of hydrogel nanoparticles is minimally affected when in biological environment, and secondly that it is not impacting the interaction of the HA-based nanoparticles with target cells.

II.V. Reference

1 Shreffler, J. W., Pullan, J. E., Dailey, K. M., Mallik, S. & Brooks, A. E. Overcoming Hurdles in Nanoparticle Clinical Translation: The Influence of Experimental Design and Surface Modification. *International Journal of Molecular Sciences* **20**, doi:10.3390/ijms20236056 (2019).

2 Bertrand, N. *et al.* Mechanistic understanding of in vivo protein corona formation on polymeric nanoparticles and impact on pharmacokinetics. *Nature Communications* **8**, doi:10.1038/s41467-017-00600-w (2017).

3 Aggarwal, P., Hall, J. B., McLeland, C. B., Dobrovolskaia, M. A. & McNeil, S. E. Nanoparticle interaction with plasma proteins as it relates to particle biodistribution, biocompatibility and therapeutic efficacy. *Advanced Drug Delivery Reviews* **61**, 428-437, doi:10.1016/j.addr.2009.03.009 (2009).

4 Champion, J. A. & Mitragotri, S. Shape Induced Inhibition of Phagocytosis of Polymer Particles. *Pharmaceutical Research* **26**, 244-249, doi:10.1007/s11095-008-9626-z (2009).

5 Blanco, E., Shen, H. & Ferrari, M. Principles of nanoparticle design for overcoming biological barriers to drug delivery. *Nature Biotechnology* **33**, 941-951, doi:10.1038/nbt.3330 (2015).

6 Stylianopoulos, T. & Jain, R. K. Design considerations for nanotherapeutics in oncology. *Nanomedicine-Nanotechnology Biology and Medicine* **11**, 1893-1907, doi:10.1016/j.nano.2015.07.015 (2015).

7 Karmali, P. P. *et al.* Different Effect of Hydrogelation on Antifouling and Circulation Properties of Dextran-Iron Oxide Nanoparticles. *Molecular Pharmaceutics* **9**, 539-545, doi:10.1021/mp200375x (2012).
8 Choi, K. Y. *et al.* Smart Nanocarrier Based on PEGylated Hyaluronic Acid for Cancer Therapy. *Acs Nano* **5**, 8591-8599, doi:10.1021/nn202070n (2011).
9 Jokerst, J. V., Lobovkina, T., Zare, R. N. & Gambhir, S. S. Nanoparticle PEGylation for imaging and therapy. *Nanomedicine* **6**, 715-728, doi:10.2217/nnm.11.19 (2011).
10 Pozzi, D. *et al.* Effect of polyethyleneglycol (PEG) chain length on the bio-nano-interactions between PEGylated lipid nanoparticles and biological fluids: from nanostructure to uptake in cancer cells. *Nanoscale* **6**, 2782-2792, doi:10.1039/c3nr05559k (2014).
11 Rotman, M. *et al.* Enhanced glutathione PEGylated liposomal brain delivery of an anti-amyloid single domain antibody fragment in a mouse model for Alzheimer's disease. *Journal of Controlled Release* **203**, 40-50, doi:10.1016/j.jconrel.2015.02.012 (2015).
12 Thi, T. T. H. *et al.* The Importance of Poly(ethylene glycol) Alternatives for Overcoming PEG Immunogenicity in Drug Delivery and Bioconjugation. *Polymers* **12**, doi:10.3390/polym12020298 (2020).
13 Moreno, A. *et al.* Anti-PEG Antibodies Inhibit the Anticoagulant Activity of PEGylated Aptamers. *Cell Chemical Biology* **26**, 634-+, doi:10.1016/j.chembiol.2019.02.001 (2019).
14 Li, C. L. *et al.* Prolongation of time interval between doses could eliminate accelerated blood clearance phenomenon induced by pegylated liposomal topotecan. *International Journal of Pharmaceutics* **443**, 17-25, doi:10.1016/j.ijpharm.2013.01.012 (2013).
15 Zhang, P., Sun, F., Liu, S. J. & Jiang, S. Y. Anti-PEG antibodies in the clinic: Current issues and beyond PEGylation. *Journal of Controlled Release* **244**, 184-193, doi:10.1016/j.jconrel.2016.06.040 (2016).
16 Yang, Q. *et al.* Analysis of Pre-existing IgG and IgM Antibodies against Polyethylene Glycol (PEG) in the General Population. *Analytical Chemistry* **88**, 11804-11812, doi:10.1021/acs.analchem.6b03437 (2016).
17 Gulati, N. M., Stewart, P. L. & Steinmetz, N. F. Bioinspired Shielding Strategies for Nanoparticle Drug Delivery Applications. *Molecular Pharmaceutics* **15**, 2900-2909, doi:10.1021/acs.molpharmaceut.8b00292 (2018).
18 Salvati, A. *et al.* Quantitative measurement of nanoparticle uptake by flow cytometry illustrated by an interlaboratory comparison of the uptake of labelled polystyrene nanoparticles. *Nanoimpact* **9**, 42-50, doi:10.1016/j.impact.2017.10.004 (2018).
19 Hadjidemetriou, M., Al-Ahmady, Z. & Kostarelos, K. Time-evolution of in vivo protein corona onto blood-circulating PEGylated liposomal doxorubicin (DOXIL) nanoparticles. *Nanoscale* **8**, 6948-6957, doi:10.1039/c5nr09158f (2016).
20 Spedalieri, C., Szekeres, G. P., Werner, S., Guttmann, P. & Kneipp, J. Probing the Intracellular Bio-Nano Interface in Different Cell Lines with Gold Nanostars. *Nanomaterials* **11**, doi:10.3390/nano11051183 (2021).

III. CHAPTER 3 - HA-BASED NANOMATERIAL INTERACTION WITH COMPLEX BIOLOGICAL ENVIRONMENTS: DIFFUSION IN TRIDIMENSIONAL TISSUES

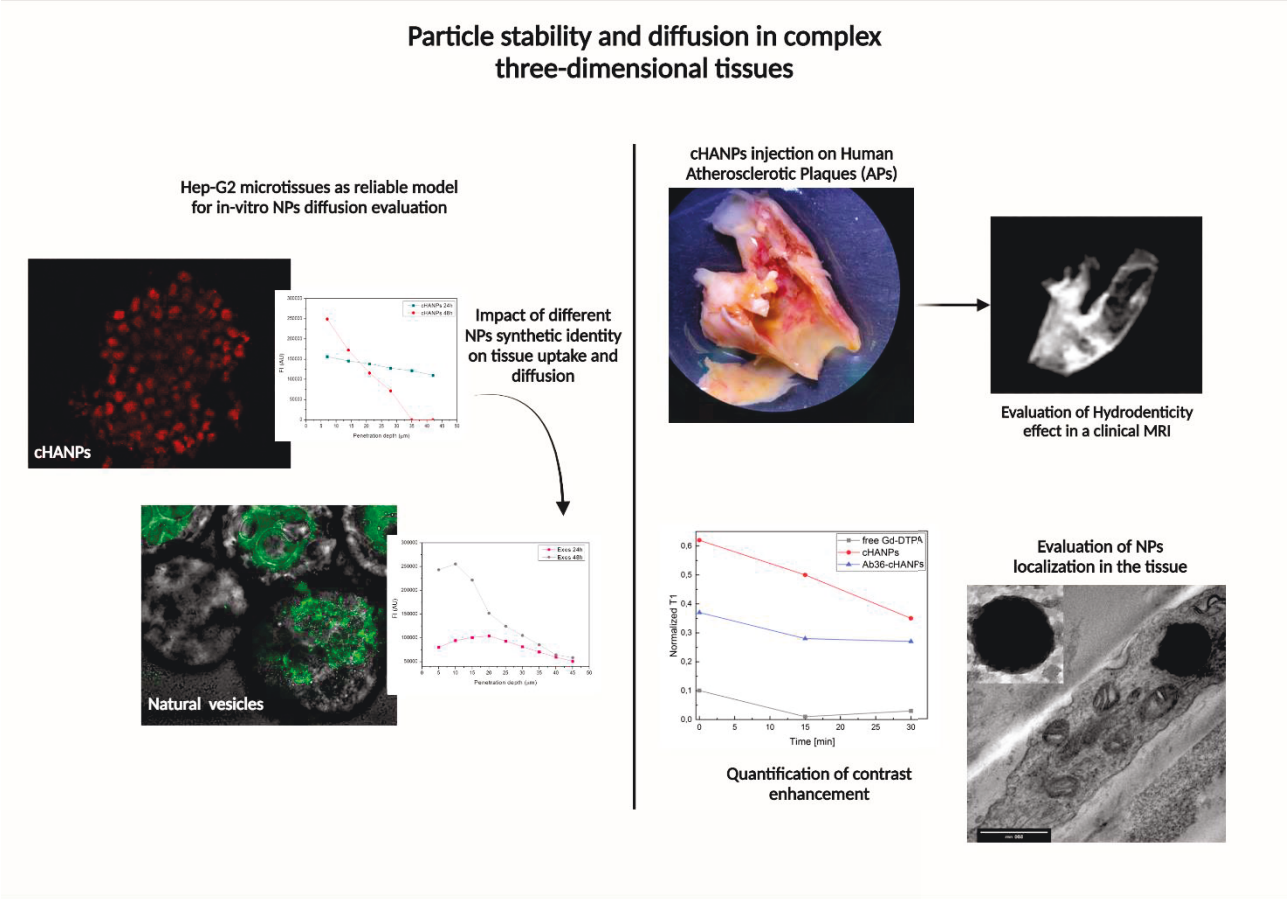

Graphical abstract Chapter 3 – Determination of NPs synthetic identity impact on penetration in complex three-dimensional liver microtissues. Assessment of nanoparticle stability and synthetic identity preservation in a complex and heterogeneous three-dimensional human tissue.

III.I. Background

In previous chapters, the characterization of the synthetic and biological identities of hydrogel nanoparticles was presented. The investigation of the impact that the contact with the biological environment has on the properties of these nanocarrier was further assessed. In this chapter, the transport properties, and the ability of hydrogel-based particles in preserving their structural properties, as well as the property of Hydrodenticity, in complex three-dimensional environments is presented.

As discussed in the background section, following the poor understanding of the connection between the synthetic and the biological identity of NPs, the use of poorly reliable platforms for their preclinical testing is the major factor affecting the ability of successfully predicting NP biodistribution and toxicity profile in clinical settings. The assessment of nanotechnology safety and efficacy starts from the

evaluation of biocompatibility and cellular uptake on 2D cell culture and moves in 3D scarcely reliable in-vitro models[1]. To increase the complexity of the testing platform, spheroid or the more complex multicellular spheroids are used as organ or disease model to evaluate the effect that the exposure to NPs has on size, growth regulation, and necrotic core formation of the spheroid itself[2]. However, it has been widely demonstrated that these models scarcely resemble organ-specific features and most importantly lack of a uniform and endogenous-like extracellular matrix able to recapitulate the tissue transport properties. These latter features are crucial for nanotechnology efficacy evaluation since, compared to free-drug molecules, NP effective diffusion in tissues is much strongly hindered by the extracellular space anatomy and this ultimately determine the efficacy of the NPs in interacting with its cellular target[3]. In 2019, Corrado et al.[4], compared the functionality and the tissue competency of Hep-G2 spheroid-like and microtissue-based in-vitro model of liver. They demonstrated that despite the high cellular density, spheroids present a low expression of typical hepatic biomarkers as well as decreased amount of secerned albumin and urea, both indicators of liver functionality. On the contrary, microtissue precursors demonstrated higher levels and faster secretion of albumin and urea as well as high P-glycoprotein 1 (P-gp) expression, a transporter protein known to be physiologically localized and expressed into the canalicular membranes of hepatocytes[5]. This protein is directly involved in the first-pass metabolism and in the biotransformation of chemicals out of the liver.

Moving further in the common pathway for testing of NPs efficacy, animal models of disease are employed to obtain preliminary estimation of *in-vivo* NPs biodistribution and toxicity[6]. However, recent literature with particular regard to tumour models, is highlighting how their reliability strongly depends on tumour implantation methodology, implantation site, developmental stage, immunocompetency of the animal and if it is an orthotopic model[7]. As an example, Zhang et al.[8], compared an orthotopic and a subcutaneous model of prostate cancer in mice revealing impactfully differences in the tumour microenvironment of the two models in terms of vascularization and hypoxia, features that are enormously impacting evaluations of drug delivery transport.

In addition, animal models are still failing in accounting inter-specie differences, especially for therapeutic dose and toxicity evaluation, revealing an intrinsic limitation as testing platform[9].

For this reason, there is an urgent need of models that are able of recapitulating the complexity of the genetic, molecular and anatomical profile of human tissues. In this sense, literature is moving towards the evaluation of treatment efficacy directly on micro biopsy of patient tissues, specifically cultured in vitro to keep key anatomical features, molecular and genetic profile unaltered[10].

In the direction of accounting some of the presented limitations, two complex, three-dimensional and reliable platforms were used for the assessment of the ability of cHANPs of preserving their structural properties and the evaluation of cHANPs transport properties. At first, the liver microtissue precursor (μ-TP) model developed by Corrado et al.[4], was employed to preliminary estimate the transport properties

of cHANPs in a complex and endogenous extracellular matrix. To further assess the role of Hyaluronic Acid and the impact that particle synthetic identity has on vector transport properties, a comparison with natural vesicles (Exos) and hybrid complex lipid-polymer NPs (Lipons) was conducted. Secondly, cHANPs structural stability was evaluated in Human Atherosclerotic Plaques (AP) removed by surgical endarterectomy. After cHANPs were specifically engineered with the antibody Anti-CD36 to interact with macrophages of the AP through the scavenger receptor CD36[11,12], the preservation of the property of Hydrodenticity in such a complex environment was demonstrated upon MRI in a clinical 1.5 T instrument. The anatomy of the plaques was chatracterized under electron microscopy and a preliminary assessment of nanoparticle-tissue interaction was performed.

III.II. Experimental Section

III.II.I. Materials

QuantiPro™ BCA Assay Kit was purchased from Sigma Aldrich (St. Louis, Missouri, USA). The rabbit anti-human polyclonal antibody to human CD36 and its biotinylated form is purchased from Invitrogen (Thermo Fisher Scientific, USA). Glutaraldehyde (25% aqueous solution; EM Grade, molecular formula $OCHCH_2CH_2CH_2CHO$, CAS #111-30-8) paraformaldehyde (16% aqueous solution, EM Grade, methanol free solution, Specific Gravity: 1.09molecular formula: HCHO), sodium cacodylate buffer (Prepared from Sodium Cacodylate Trihydrate F.W. 214.02), potassium ferrocyanide (ACS reagent, molecular formula K3Fe(CN)6 F.W. 329.25), osmium tetroxide (4% aqueous solution, molecular formula OsO4, F.W. 254.20), uranyl acetate (4% aqueous solution ACS reagent, molecular formula $UO2(OCOCH_3)2{\cdot}2H2O$ F.W. 424.14), Spurr epoxy resin (low viscosity kit: NSA Nonenyl Succinic Anhydride, EM grade, DER 736 Specific Gravity: 1.14, ERL 4221 Cycloaliphatic Epoxide Resin specific gravity (H_2O=1), DMAE 2-dimethylaminoethanol C4H11NO F.W. 89.14 Specific Gravity: 0.883-0.888) were purchased from Electron Microscopy Sciences. FOMBLIN® (perfluoropolyether), was purchased from Merck KGaA (Germany). HepG2 cells and liver µ-TP were kindly provided by the doctor Vincenza de Gregorio (University Federico II of Naples).

III.II.II. Human Atherosclerotic Plaques

Atherosclerotic plaques (APs) are harvested by carotid endarterectomy from subjects with severe atherosclerotic disease (>70% stenosis or 50% to 70% stenosis with clinical symptoms – according to American Heart Association guidelines) and donated for research with the written consent by 6 Males patients recruited by the Department of Public Health (Vascular Surgery Unit) of the University of Naples Federico II (Ethical Committee of the University of Naples Federico II - Number 157/13,

September 9, 2013). APs are collected and transported in saline solution at 4°C, within 2 hours of explantation. If not used right after the removal, APs are stored in liquid nitrogen and progressively defrosted in 24h prior to use.

III.II.III. Preliminary evaluation of cHANPs diffusion in liver µ-TP

cHANPs co-encapsulating Gd-DTPA and ATTO 633 are produced as described in previous chapters. Briefly, a microfluidic X-junction chip is used to implement nanoprecipitation. A solvent solution of HA (0.05% w/V), Gd-DTPA (0.1%w/V), ATTO 633 (10 nmol/mL) and NaOH (pH=12.2) is injected in the middle channel at 27 µL/min and a non-solvent solution of Acetone and DVS (4% V/V) in the side channels at 110 µL/min.

Mature liver µ-TP were provided by Dr. Vincenza de Gregorio[4]. For testing, µ-TP were seeded in a 96-well conic bottom plate at different densities moving from 3 to 10 µ-TP/well and wells with a maximum of 5 µ-TP/well were selected for testing. cHANPs at a concentration of 100 µg/mL were added to the suspension medium without FBS and let interact for 24h or 48h. As a comparison, the same procedure was followed for exosomes stained with PKH67 (Exos) and hybrid lipid-polymer nanoparticles encapsulating ATTO633 (Lipons) at a concentration of 100 µg/mL and 53.2 µg/mL, respectively. µ-TPs without any treatment and cultured in serum free-medium were used as negative control.
At the desired time point, µ-TPs were transferred in an 8-well µslide (IBIDI®) and confocal imaging with a HCX PL APO CS 63 x 1.40 Oil objective was performed. Argon laser at 488 nm and HeNe 633 nm laser were used. Z-stacks to understand about NP tissue penetration were acquired.

III.II.IV. Quantification of NPs penetration into tissue

The acquisition of Z-stack of NP-exposed µ-TP was performed to indirectly assess NP penetration into tissues. Quantification of NP penetration was performed through full picture fluorescence quantification by ImageJ. Basically, full picture fluorescence is acquired for each z-step which had different thickness depending on the local thickness of the observed tissue. This value is corrected for autofluorescence by subtracting the fluorescence of the untreated tissues with the same laser options. These normalized values are then plotted against tissue thickness and the fluorescence profile analysed.

III.II.V. cHANPs engineering for selective interaction with Human AP

The antibody anti-CD36 is conjugated on the surface of the nanoparticle firstly indirectly, by means of the biotin-streptavidin bridge and then directly. In the first strategy, HA carboxyl groups are activated by 10 min of wheel stirring with EDC (0.02 M) and NHS (0.01 M). After activation, streptavidin (STV) (25 µg/mL) is added to NP suspension and wheel stirred for 1h. Centrifugation in Corning® Spin-X® UF Concentrators with a MWCO of 50 kDa by Corning (New York, USA) at 2000 rpm, 4°C for 10 min is used to remove excess of streptavidin.

The amount of successfully bound ST to ST-cHANPs is quantified by BCA assay. For quantification, 150 µL of NPs and 150 µL of buffer are let react for 1h at 60°C in a 96-well plate. The amount of bound STV is quantified by means of a calibration curve (0.5-30 µg/mL). cHANPs absorbance cHANPs is in triplicate and its value is subtracted to the total absorbance of ST-cHANPs.

Then, the biotinylated anti-CD36 (0.005 µg/mL) is added to ST-cHANPs and let react for 4h. Centrifugation in Corning Concentrators with a MWCO of 50 kDa by Corning (New York, USA) at 3000 rpm, 4°C for 10 min is used to remove the unreacted antibody. In the following sections, this formulation is reported as Ab36-ST-cHANPs.

In the second strategy, the anti-CD36 is conjugated directly to the NPs surface. Carboxyl groups are activated as before. After activation, anti-CD36 (0.0025 µg/mL) is added directly to the suspension and let react for 4h. Centrifugation in Corning Concentrators with a MWCO of 50 kDa by Corning (New York, USA) at 3000 rpm, 4°C for 10 min. In the following section, to remove the unreacted antibody and this formulation is reported as Ab36-cHANPs.

III.II.VI. Morphological Characterization of Atherosclerotic plaques (AP) by Electron Microscopy (EM)

Both SEM and TEM are used to investigate the morphology of atherosclerotic plaques (AP). After macroscopic analysis and classification, atherosclerotic plaques containing some adherent intima and media are dissected and subsequently treated for electron microscopy imaging. For the TEM observation, Samples are cut into pieces less than 1 mm^3 and fixed with 0.5% glutaraldehyde plus 4% paraformaldehyde in 0.1M sodium cacodylate overnight at 4°C, then washed three times with 0.1 M sodium cacodylate buffer. APs are then post-fixed with 1% osmium tetroxide/1% potassium ferrocyanide mixing in 0.1 M sodium cacodylate, for 1 hour in ice, in the dark, and washed in a chilled buffer. The en-bloc staining is performed with 4% uranyl acetate aqueous solution overnight at 4°C followed by washing in chilled water. The dissected pieces are dehydrated with an ascendant series of ethanol (30%-50%-70%-95%-absolute) on ice. Dehydrated samples for TEM imaging are embedded in Spurr epoxy resin and after polymerization at 60 °C for 72 h were sectioned by Ultramicrotome (FC7-UC7, Leica). The 70 nm slices obtained are seeded on 200 mesh copper grids and imaging is

carried out by using a Tecnai G2-20 (FEI_USA) at a 120KV, in a range of magnification between 2 µm and 500 nm. Dehydrated samples intended for SEM imaging are subjected to Critical Point Drying (CPD) process before the imaging. A layer of 20 nm of Gold is sputtered (HR 208, Cressington) before imaging with a Field emission SEM (Ultraplus, Zeiss, Germany). The secondary electron detector is used and the images were acquired at 10 kV in a range of magnification between 2 µm – 200 µm.

III.II.VII. Ex-vivo Magnetic Resonance Imaging (MRI)

Pre-contrast and post-contrast imaging are performed on APs at 3 T on a PET/MRI (Siemens) to reconstruct tissue three-dimensional structure and evaluate contrast agent performances. Prior to imaging, each AP is submerged in Fomblin® to preserve tissue hydration and structure during imaging. Fomblin does not have a residual MR signal and does not interfere with the biological tissue signal [14]. Each experiment is performed by placing six APs in a 6-well plate, one per well. APs are divided into three groups of two to account for the intrinsic variability in terms of anatomy and composition characterizing each plaque. Each group of two plaques is injected with a different contrast agent: Gd-DTPA, cHANPs, and Ab36-cHANPs. By means of a cannula needle (24 G x 19 mm) fixed in the lumen of the aorta, 150 µL of contrast agent suspension at the same Gd-DTPA concentration are slowly injected and imaging is performed soon after, 15 and 30 minutes after the injection. The T1-weighted MR images of HA NPs, unloaded and loaded with Gd-DTPA at different concentrations using an inversion recovery sequence are measured with the following parameters: TR = 2500 ms; TE = 12 ms; TI = 50, 100, 200, 400, 800, 1100, 1800 ms; FOV= 180x146 mm; slice thickness = 4 mm, acquisition matrix = 360x292. Each acquisition has a duration of 12 minutes.

III.II.VIII. MRI post-processing

Images obtained by bidimensional T1-weighted spin-echo sequences are post-processed with a software tool named Mr map to build a T1 map of the tissue. Maps are calculated by selecting the single sequences with the different TI values in the various phases before and after injection of contrast agent. T1 are measured in 20 pixels wide Region of Interest (ROI) which are chosen in a region with apparent homogeneous contrast. T1 values are then normalized as follows

$$Normalized\ T1 = \frac{T1_{pre-injection} - T1_{post-injection}}{T1_{pre-injection}}$$

to evaluate the contribution of every injected CAs to the variation in measured T1.

III.II.IX. A preliminary study of the interaction of cHANPs and Ab-cHANPs with APs: ex-vivo Electron Microscopy

After MR imaging, atherosclerotic plaques injected with different contrast agents (cHANPs and Ab36-cHANPs) are fixed and processed for electron microscopy. The site surrounding the injection by cannula needles is dissected from each plaque and processed for TEM imaging, according to the protocol described above.

III.III. Results

III.III.I. Preliminary evaluation of cHANPs diffusion in liver µ-TP

Co-loaded cHANPs are incubated with liver µ-TP to study NPs transport properties through a reliable model, able to recapitulate endogenous extracellular matrix features[4]. As a first step in the experiment design, the quantification of cHANPs uptake (50 µg/mL) by a 2D layer of Hep-G2 cells was performed in order to select the most suitable timespan to perform contact with the 3D tissue. Flow cytometry results in Figure 3.1 reveal a significant uptake in all the investigated time points that is not saturated within the first 12h of contact, as revealed by SSC in Figure 3.1a. Fluorescence intensity in Figure 3.1b confirms that a significant particle uptake occurred up to 24h where a slight decrease in fluorescence was observed as a result of the cell duplication causing the redistribution of NPs in daughter cells.

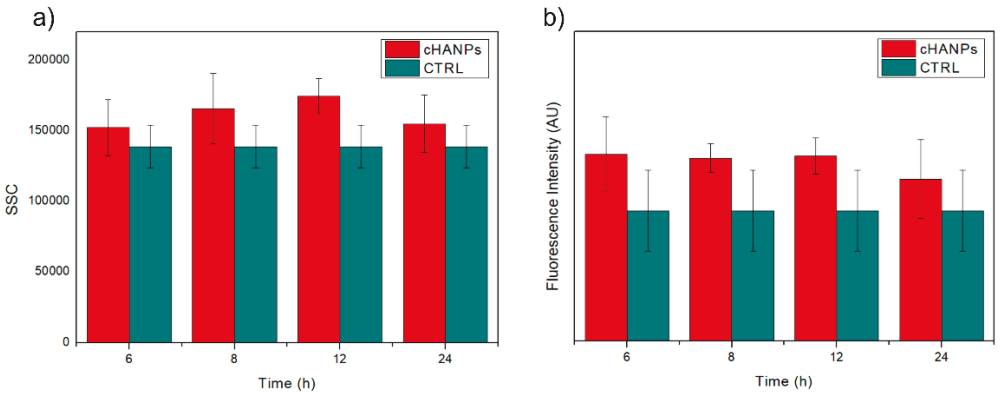

Figure 3.1 – Quantitative uptake of cHANPs by Hep-G2 adherent cells. a) Side Scattering (SSC) of Hep-G2 cells incubated with cHANPs; b) Fluorescent Intensity of Hep-G2 cells incubated with cHANPs

For this reason, considering the most complex structure of the 3D tissue and the time required for NP diffusion in the whole thickness of the tissue, 24h and 48h were set as sampling time points for determination of NP penetration.

As a second step, cHANPs (100 µg/mL) were incubated with µ-TP in serum free medium to assure that the results obtained in the evaluation of NP ability to penetrate the tissue could be attributed directly to the NP synthetic identity. After the two selected time points confocal images were acquired as described in the dedicated method section. Results in Figure 3.2 show that a significant presence of NPs in the core of the observed microtissues could be detected at both time points.

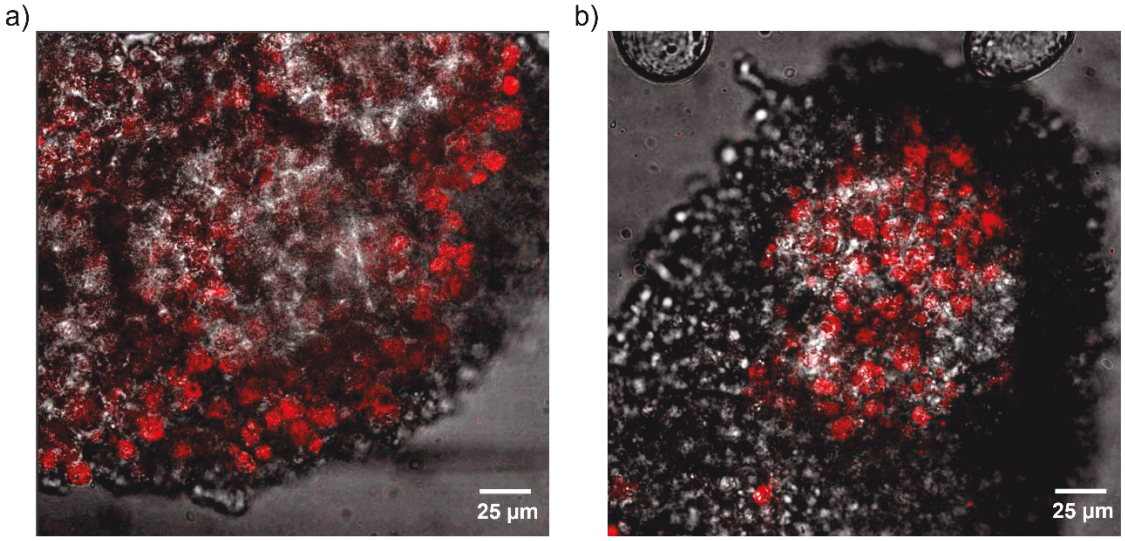

Figure 3.2 – Confocal images of liver µ-TP incubated with co-loaded cHANPs a) µ-TP fluorescence after 24h of cHANPs incubation; b) µ-TP fluorescence after 48h of cHANPs incubation.

From the images it is possible to observe the absence of diffuse fluorescence as a sign of stability of dye encapsulation in the particles, indirect indication of particle structural preservation. In addition, images reveal that fluorescence can be detected in the whole cell cytosol, being the cells composing the tissue clearly visible. Already after 24h, a significant NP uptake was detected, and this might be attributed to the expression of CD44 receptors on Hep-G2 cells, despite this cell line is reported as the lowest CD44 expressing cell line among liver tissue ones[15]. Being a natural target of HA, CD44 receptors might have mediated the high particle uptake inside liver µ-TP.

To assess the depth of cHANPs penetration inside the tissue, z-stacks were acquired, and full picture fluorescence quantified for every z-step, then plotted against tissue thickness (further details in the dedicated method section). Results in Figure 3.3 reveal that 24h represent a sufficient time to allow particle penetration up to 45 µm deep in the tissue. In addition, this reveals that particles can diffuse in the tissue and preserve their stability until reaching inner-core cells. By comparing these values with the ones obtained for 48h, it is possible to observe higher values in the surface of the tissue and significantly reduced fluorescence in the core of the tissue, reaching no significantly increased fluorescence with respect to control from 35 µm on. This profile reveals that 24h are not enough to saturate the uptake of cHANPs that continues increasing over time, as revealed by the superficial fluorescence. However, drop in tissue fluorescence over thickness reveals that particles are degraded

by cells and that particle diffusion, being slower than the degradation, cannot assure uniform fluorescence over the whole tissue thickness.

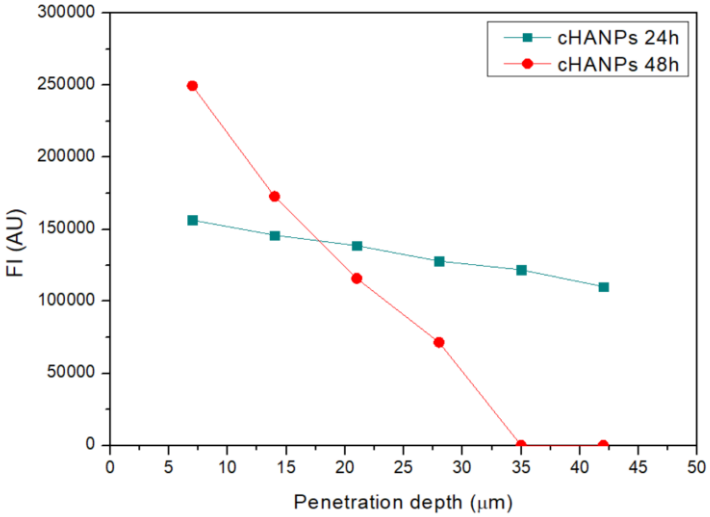

Figure 3.3 – cHANPs time-dependent penetration in liver μ-TP

Comparison of cHANPs and different synthetic identity' NPs in μ-TP penetration

Results obtained for cHANPs were compared with the penetration of other two NP systems, U87 derived exosomes (Exos)[13] and Hybrid lipid polymer NPs (Lipons) to study the impact of different synthetic identities on nanoparticle diffusion. The tested Exos and Lipons exhibit a mean size of about 150 nm and 90 nm, respectively. These systems were chosen to preliminary compare the impact that vesicle-based and natural but very complex vectors, such as exosomes and hybrid lipid polymer structures such as Lipons have in the interaction with liver μ-TP and how this interaction impacts on tissue penetration. Also in this case, confocal images were acquired after 24h and 48h of incubation and z-stacks were acquired to quantify NP penetration into tissue. Images in Figure 3.4 reveal very different behaviour of the two systems over time. The first thing to be observed is the different interaction that this NPs have with liver μ-TP. Exos are accumulating in specific spots, interacting specifically with some domains. Whether these domains are located on cell membrane or intracellularly is not known. Lipons, as cHANPs, occupy the whole cell cytosol, making cells clearly visible. Additionally, by looking at the corrected full picture fluorescence plotted against tissue thickness in Figure 3.5, it can be observed that for both NP systems 24h are not enough to guarantee a significant accumulation of the particles in the tissue. In addition, by looking at 48h fluorescence it can be observed that Exos are still majorly accumulated in the tissue surface with the higher fluorescence observed between 5 and 20 μm of tissue depth. By looking at Lipons, it can be instead

registered a significant fluorescence in whole tissue thickness with higher values in the first 20 µm of depth.

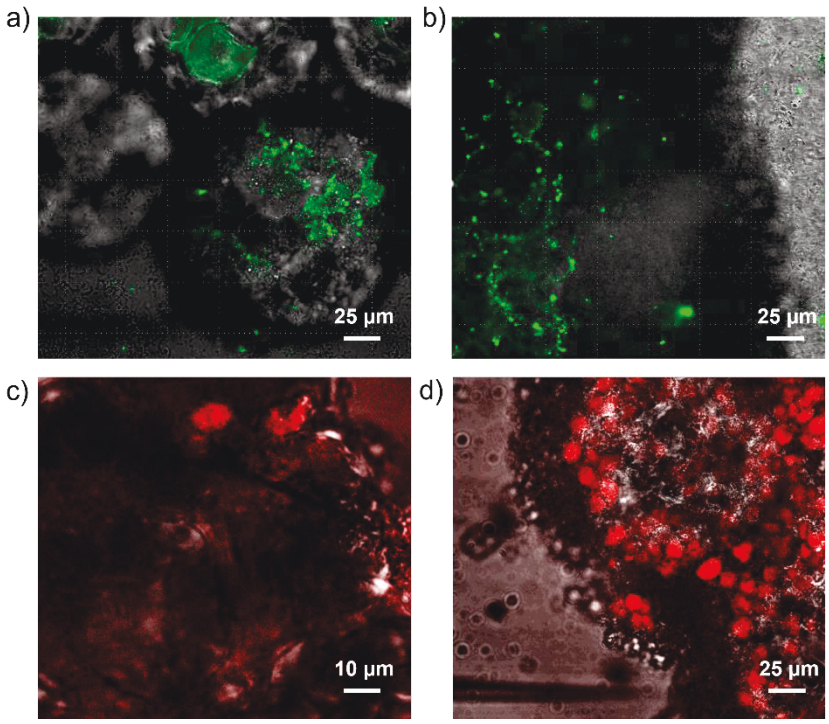

Figure 3.4 - Confocal images of liver µ-TP incubated with co-loaded cHANPs a) µ-TP fluorescence after 24h of Exos incubation; b) µ-TP fluorescence after 48h of Exos incubation; c) µ-TP fluorescence after 24h of Lipons incubation; d) µ-TP fluorescence after 48h of Lipons incubation

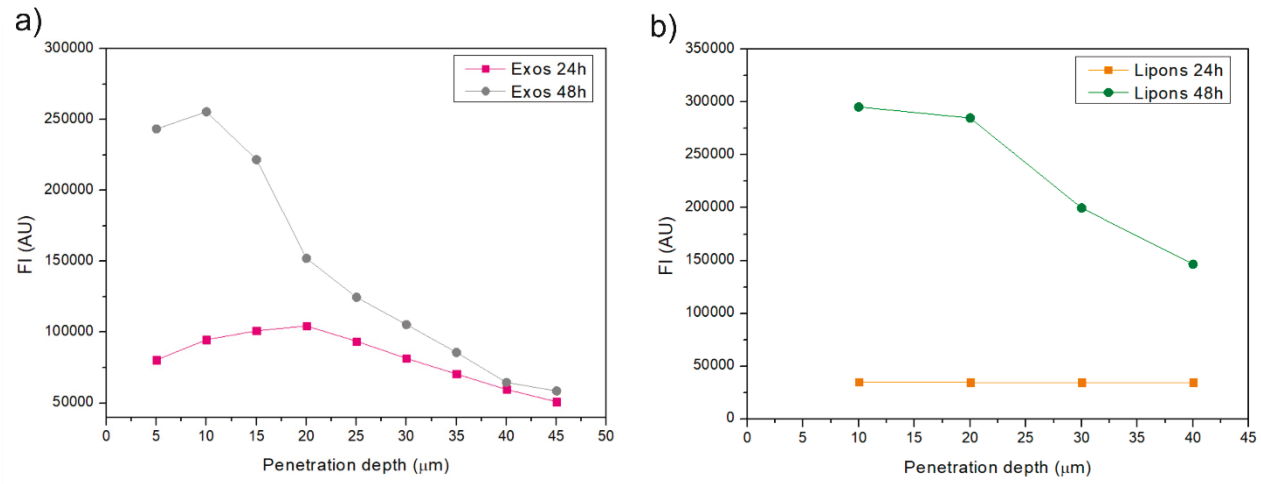

Figuure 3.5 - Time-dependent penetration in liver µ-TP of a) Exosomes; b) Lipons

III.III.II. cHANPs structural stability in human Atherosclerotic Plaques

Atherosclerosis is an inflammatory pathology that interests the intima and media layers of arteries of medium and large size and is characterized by the formation of typical Atherosclerotic lipid Plaques (AP) that cause the narrowing of the vessel lumen. During the AP formation, the endothelium lining the vessel changes dramatically, allowing the invasion of inflammatory and immune cells (macrophages and T cells)[16] with the consequent formation of a fibrous cap deposited to isolate the site of inflammation. As this fibrous cap becomes thinner, the plaque is at risk of rapture with severe consequence for the patient as stroke and death. For this reason, AP represent a highly complex environment made of highly heterogeneous cellular and extracellular components.

Hyaluronic acid (HA) possess a good potentiality to naturally interact with the AP since it is a substrate for many receptors particularly abundant in the AP such as CD44 and ICAM [17]. In addition, the discovery that inflammation drives plaque growth and rupture additionally suggests that the immune system might be an interesting diagnostic target [18]. Specifically, the macrophage scavenger receptor CD36 is present on the surface of macrophages and is implicated in the formation of foam cells. Indeed, the process, that starts with the uptake of oxidized Low-Density Lipoprotein (oxLDL) by macrophages, causes the upregulation of CD36 which is called the "eat me signal". In addition, oxLDL via CD36 inhibits macrophage migration exerting a macrophage-trapping mechanism in the atherosclerotic lesion. For these reasons, CD36 was conjugated on cHANPs surface prior evaluation of its interaction with APs.

Engineering of cHANPs for selective interaction with human AP

As discussed, despite this intrinsic targeting ability of hyaluronic acid, cHANPs surface was further engineered to improve the specificity of the probe by surface decoration with the antibody Anti-CD36 (Ab36) for macrophages active targeting.

The surface decoration was performed by first indirect streptavidin mediated conjugation and then directly. In the first strategy, the surface of nanoparticles is conjugated to streptavidin (ST) to produce ST-cHANPs. The protein was covalently bound to carboxyl groups of HA and biotin-Ab36 was conjugated exploiting the high biological affinity between ST and Biotin to ST-cHANPs, producing Ab36-ST-cHANPs. The amount of ST successfully bound to the surface of nanoparticles was measured by BCA assay and results showed a very high binding efficiency of 92,6%. However, TEM investigation of particle morphology in Figure 1b revealed that Ab36-ST-cHANPs were increased in size as a consequence of multiple ST layers deposition on cHANPs surface. This might affect the surface properties of the particles completely altering its synthetic identity.

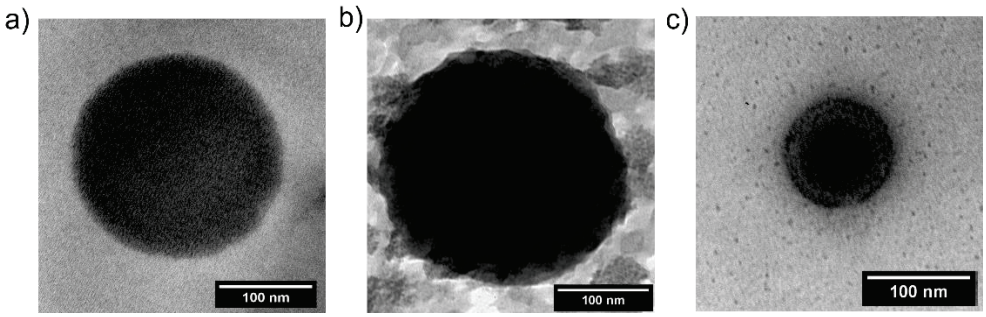

Figure 3.6 – Transmission Electron Microscopy (TEM) images of a) cHANPs; b) Ab36-ST-cHANPs c) Ab-cHANPs

For this reason, direct conjugation of the Ab36 to the surface of cHANPs with the aim of preserving the exposure of some HA chains to APs, was explored. In this second strategy, the amine groups of the Ab36 are covalently bound to the carboxyl group of HA, to produce Ab36-cHANPs. The TEM image in Figure 1c revealed the presence of the Ab36 on Ab36-cHANPs. PSD of Ab36-ST-cHANPs and Ab36-cHANPs is measured by DLS and revealed a mean size of about 215,2 ± 72 nm which slightly differs from cHANPs mean size. Overall, TEM images and DLS measurements demonstrate the morphological stability of nanoparticles against conjugation.

Relaxometric properties of cHANPs, Ab36-ST-cHANPs and Ab36-cHANPs: preservation of Hydrodenticity

After morphological stability after surface conjugation has been assessed, cHANPs ability of retaining both Gd-DTPA cargo and the Hydrodenticity properties were assessed. ICP-MS measurements are performed to quantify the amount of encapsulated Gd-DTPA and results are shown in Table 1. The measurements demonstrate that both Ab36-ST-cHANPs and Ab36-cHANPs retain Gd-DTPA with a partial loss which is more pronounced for Ab36-cHANPs (about 55%). However, the distribution of the longitudinal relaxation time T1 of Ab36-ST-cHANPs and Ab36-cHANPs presented in Figure 3.7 shows that, despite the increase in T1 is presence both for Ab36-ST-cHANPs and Ab36-cHANPs with respect to cHANPs, it is more evident for Ab36-ST-cHANPs which instead retain a higher amount of Gd-DTPA. The reason for that may be found in the effect that ST has on the polymer network. The deposition of many layers of ST on the surface of nanoparticles might cause a loss of elasticity of the polymer chains as well as the hindering of efficient water exchange with Gd-DTPA, resulting in a lower relaxivity. This hypothesis can be confirmed by comparing the amount of residual Gd-DTPA in both Ab36-ST-cHANPs and Ab36-cHANPs to Gd-DTPA concentrations associated with the measured relaxivity. The comparison presented in Table 1 reveals a boosting of 4 times for cHANPs and 2,68 times for Ab36-cHANPs, confirming that this system preserves the Hydrodenticity property. Differently no boosting is present for Ab36-ST-cHANPs, as hypothesized. For this reason, the next

experiments are conducted with Ab36-cHANPs which demonstrate to preserve the Hydrodenticity effect.

Table 1 – Impact of surface conjugation on the Hydrodenticity effect

	Gd-DTPA content [uM]	***Gd-DTPA [uM] T1 associated***	***Boosting Times***
cHANPs	*19*	*74,5*	*4*
Ab-ST-cHANPs	*18,12*	*19*	*1,04*
Ab-cHANPs	*10,6*	*27,9*	*2,63*

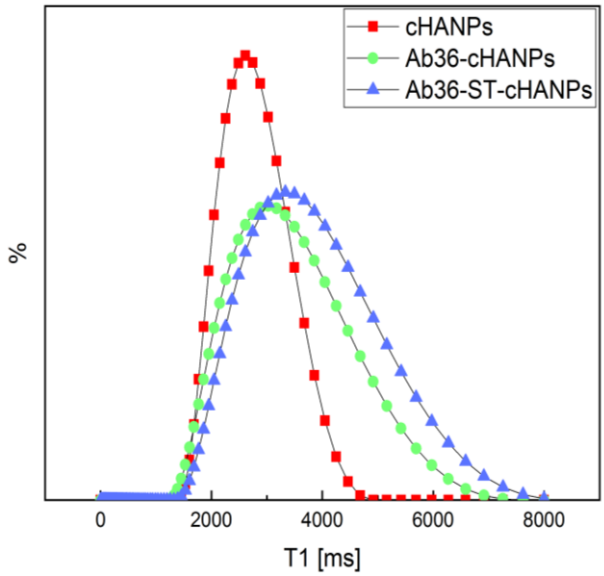

Figure 3.7 – Comparison of relaxometric properties of cHANPs, Ab36-ST-cHANPs and directly conjugated Ab36-cHANPs

Electron Microscopy characterization of human AP

Atherosclerosis is activated by alterations of the endothelial layer of blood vessels [19]. For this reason, the characterization of endothelium alterations is particularly relevant to understand both the physiopathology of the disease and the composition of the tissue interacting with the imaging probe during the diagnostic investigation when injected into blood circulation. Here, both scanning and transmission electron microscopy (SEM and TEM) were used to characterize human carotid APs and in particular their luminal wall. Figure 3.8 shows SEM images of a transversal section of a human AP. Each sample analysed has disrupted endothelial lining and presents delamination in different layers. Indeed, as shown in Figures 3.8a and 3.8b the endothelium of tunica intima is detached from the basal lamina (red arrow), and in some areas, the endothelial lining appears to be interrupted and damaged (black arrow). In some points, the endothelial layer is completely absent showing only the

fibrinous reticulum, as presented in Figure 3.8c. Also, in the areas covered by the endothelial layer, there are cells showing pseudopodia (white arrow in Figure 3.8d) and microvilli. The formation of microvilli may indicate diffuse endo/exocytosis phenomena, confirming that dysfunctional endothelium is characterized by altered permeability. These observations are confirmed by TEM imaging as shown in Figure 3.9. Figure 3.9a shows a cross-section of human carotid AP particularly abundant in lipid droplets of different sizes and surrounded by calcium deposits (red arrow) which are mixed in the fibrinous reticulum. In Figure 3.9b the matrix reveals also the presence of interspersed cholesterol crystals which Grebe et al. [20] defined as a hallmark of advanced atherosclerotic plaques. In Figure 3.9c the cross-section of the tunica intima shows the absence of endothelial cells thus the complete damage of the endothelial lining, as observed by SEM imaging. All these observations confirm the abundance of exposed macrophages and thus the great potential of Ab36 targeted probes for the diagnosis of APs.

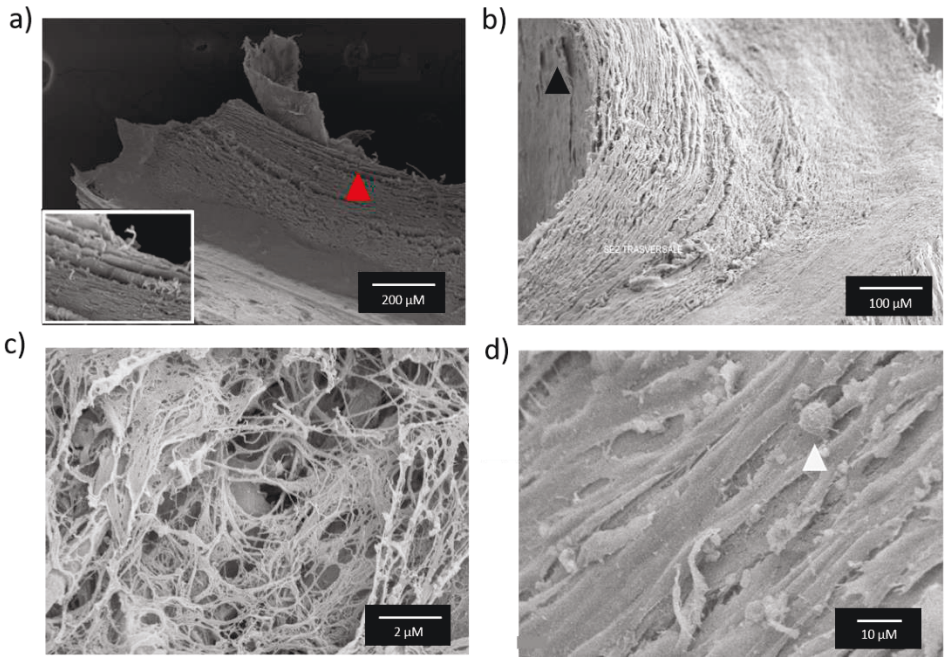

Figure 3.8 – Scanning Electron Microscopy of a human AP. a) tunica intima with detached basal lamina; b) damaged endothelium; c) fibrous cap where endothelium is absent; d) infiltrated cells with pseudopodia and microvilli

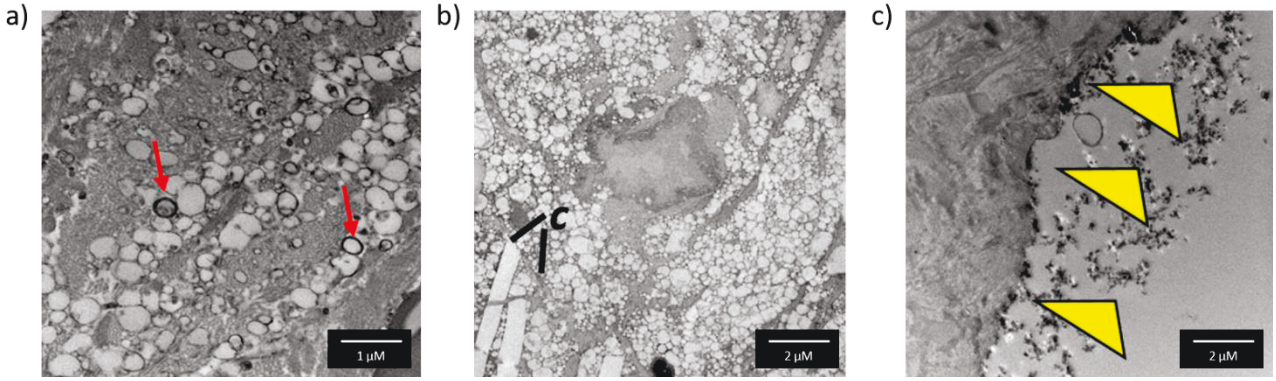

Figure 3.9 – Trasmission electron Microscopy of a human AP. a) Lipid droplets of different dimensions; b) cholesterol crystals dispersed in the lipidic component of the plaque; c) damaged endothelium

Ex-vivo Magnetic Resonance Imaging (MRI)

The following section aims to demonstrate that the Hydrodenticity of cHANPs and Ab36-cHANPs which confers improved relaxometric properties to these imaging probes, is preserved in the complex environment of APs, demonstrating that these systems preserve their synthetic identity is such a complex microenvironment. In this regard, an ex-vivo Magnetic Resonance Imaging experiment is conducted on six human carotid APs injected with three different contrast agents: free Gd-DTPA, cHANPs, and Ab36-cHANPs all at a concentration of 12 µM of Gd-DTPA. As known, APs have very different compositions and to account for this variability each probe is injected in two different plaques. The first set of experiments is dedicated to the optimization of the volume of injection to guarantee a good permeation of the tissue without liquid loss. The optimal volume of injection is set at 150 µL. The anatomy of APs is reconstructed by three-dimensional inversion recovery (IR) sequences before injection of contrast agents. After, T1-weighted images pre, post, 15 min, and 30 min after injection bidimensional spin-echo T1-weighted sequences are used to acquire images to build a T1 map of the APs in this way evaluating the contribution of each contrast agent to AP relaxivity. Figure 3.10a presents a typical setting of the experiment. Figure 3.10b presents the output of a spin-echo sequence. These images are then post-processed to build a T1 map as shown in Figure 3.11a where the value of T1 is evaluated in a Region of Interest (ROI) of about 20 pixels. As described in the dedicated method section, the contribution of each CA to the measured T1 is evaluated normalizing the T1 value measured at each time point post-injection with respect to the T1 measured in the same ROI before injection. Results in Figure 3.11b show that both cHANPs and Ab36-cHANPs provide a normalized T1 significantly higher than free Gd-DTPA even if injected at the same concentration, at any time point. These results show that the Hydrodenticity of both cHANPs and Ab36-cHANPs is preserved over time in a complex environment (such as APs) despite the great variability in the composition of the injected tissues. Table 2 reports the complete set of analysed data.

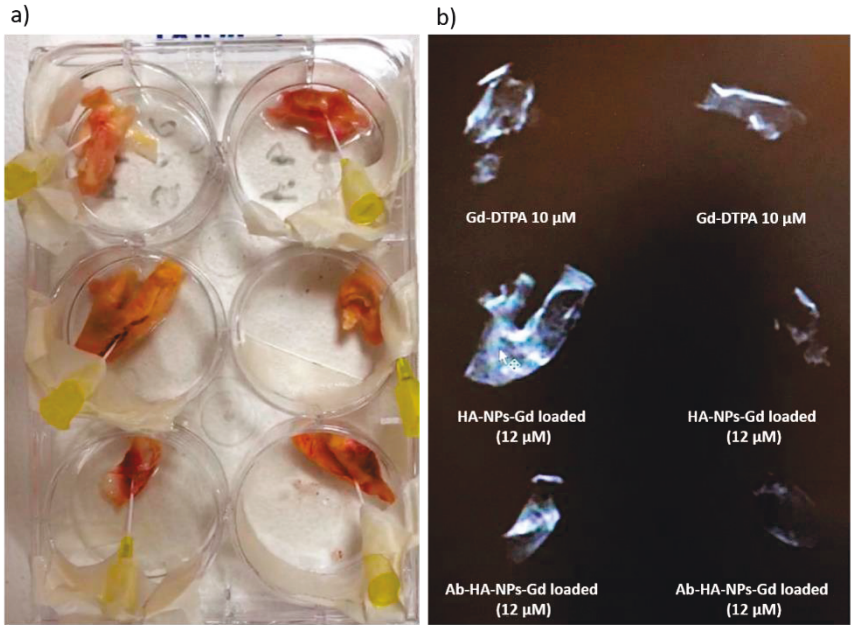

Figure 3.10 – Magnetic Resonance Imaging of human APs. a) Typical experimental setting; b) MRI of six human APs injected with 3 different CAs: free Gd-DTPA, Gd-loaded cHANPs and Gd-loaded Ab36-cHANPs

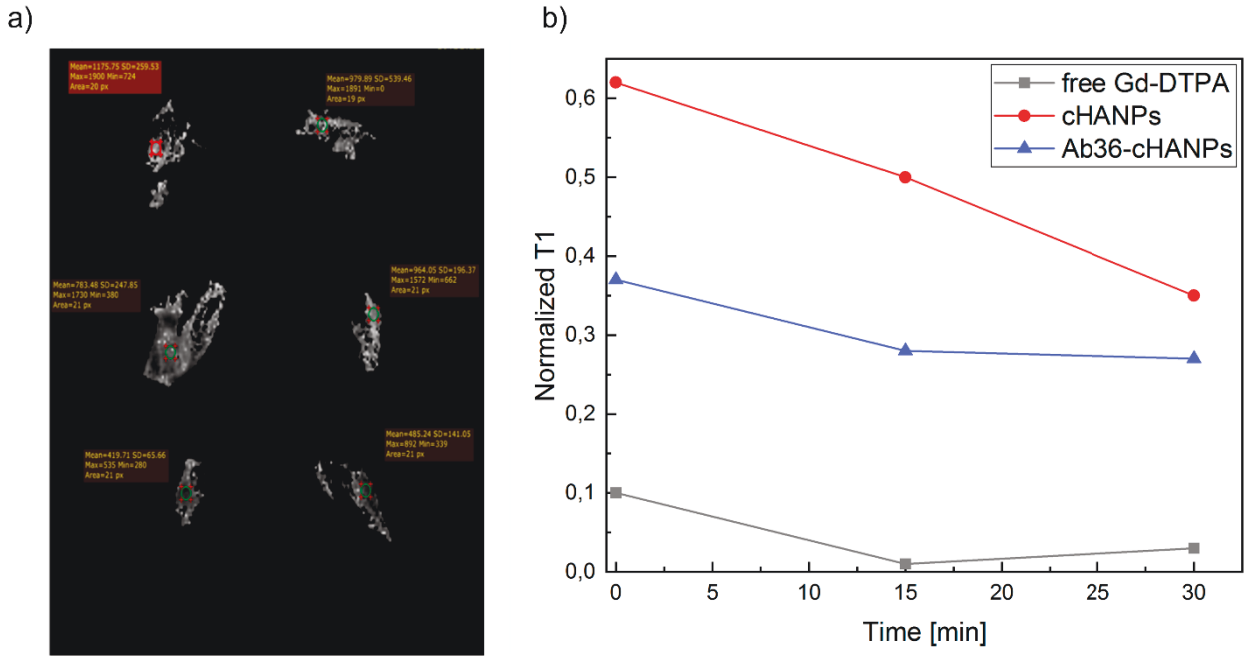

Figure 3.11 – Quantification of contrast enhancement due to CA injection. A) T1 map of AP for T1 quantification; b) T1 signal normalization for evaluation of contrast enhancement evolution over time for the injected CAs.

Table 2 – Complete set of T1 values measured for free Gd-DTPA, cHANPs and Ab36-cHANPs

Experiment 1	Gd-DTPA 12 uM	Gd-DTPA 12 uM_2	cHANPs (12 uM)	cHANPs_2 (12 uM)	Ab-cHANPs (10,6 uM)	Ab-cHANPs (10,6 uM)
Pre-injection	1175,75	979,89	964,05	485,24	783,48	419,71
St Dev	259,53	593,86	196,37	141,05	247,85	65,66
Post-injection	1346,45	903,48	773	733,62	782,6	480
St Dev	317,1	641,49	281,84	264,06	144,94	62,75
15 min post-injection	1142,45	875,81	831,05	604	754,45	480,22
St Dev	245,65	573,13	262,04	182,16	109,38	63,77
30 min Post-injection	1137,4	1117,43	816,05	668,95	746,4	479,67
St Dev	332,94	471	261,43	231,12	255,17	47,94

III.III.III. A preliminary study of the interaction of cHANPs and Ab36-cHANPs with APs: ex-vivo Electron Microscopy

A preliminary study about the interaction of cHANPs and Ab36-cHANPs with APs is conducted by dissecting the injection site of the plaque after MRI and performing TEM imaging. In the first step, the stability of NPs at exposure to chemical reagents used for EM preparation protocol was assessed to assure that that no morphological changes occurred when nanoparticles are exposed to 4% paraformaldehyde, 2,5% glutaraldehyde, 2%Osmium tetroxide, and 0,1 M sodium cacodylate. Then, the injection site was dissected and prepared for TEM imaging. As described in the method section, the preparation protocol for EM included many washing steps that might have caused the removal of the majority of the particles that are not specifically interacting with the AP. Figures 3.12a and 3.12b present TEM images of a section of AP previously injected with cHANPs and Ab36-cHANPs, respectively. A comparison with other works based on the study by Liu et al.[21] on macrophage morphology, confirms, in both cases, that the nanoparticles lie in cellular compartments, which can be easily recognized by the presence of mitochondria in the first image and of the cell nucleus with DNA in the second one. No particles were found in the extracellular matrix. It is possible to hypothesize that both these observations might be due to an interaction between hyaluronic acid and scavenger receptors for cHANPs and additionally to the antigen CD-36 in the case of Ab36-cHANPs. However, these preliminary results should be confirmed by a chemical assay (e.g. immunohistochemistry).

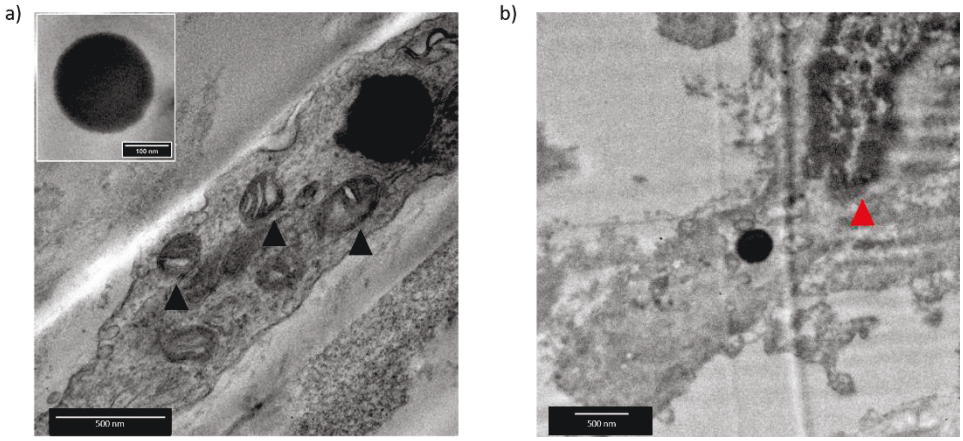

Figure 3.12 – Transmission electron microscopy of a section of APs injected with bare cHANPs and Ab36-cHANPs. a) cellular localization of cHANPs (cell mitochondria by black triangles); b) cellular localization of Ab36-cHANPs (nucleus indicated by red triangle)

III.IV. Conclusions

In the first section of the chapter, the transport properties of cHANPs in liver µ-TP as a reliable model, able to recapitulate endogenous extracellular matrix features, were preliminarily investigated. The same experiment was performed for other two different NP systems, exosomes and hybrid lipid-polymer NPs to compare the role of different NPs synthetic identity on liver µ-TP penetration. Overall, results allowed to preliminary conclude that cHANPs are the faster interacting NP system and, as stated, this might be attributed to the presence of CD44 receptors on Hep-G2 cell surface. Indeed, in 24h a homogeneous distribution of NPs in the whole thickness of the tissue could be detected. This result needs to be confirmed by determination of particle uptake kinetic, localization of CD44 receptors and evaluation of the cellular fate of NPs once inside the tissue. Moreover, the consequence of this faster interaction should be evaluated in an in-vivo context, with particular regard to clearance from blood circulation.

In the second section, cHANPs interaction with a second, very complex tissue was evaluated. Gd loaded cHANPs distribution and preservation of Hydrodenticity property in Human atherosclerotic plaques (AP) was assessed. After particle injection in AP, contrast enhancement due to free Gd-DTPA, bare particles and Ab36-cHANPs was evaluated and the preservation of the Hydrodenticity effect, which means the preservation of nanoparticle structural properties, was confirmed with both bare and engineered nanoparticles providing a boosting in contrast enhancement with respect to free Gd-DTPA at the same concentration. Additionally, it was possible to preliminary assess the interaction of cHANPs with AP after injection by TEM. In these observations, cHANPs were detected on the cellular components of the tissue however, further studies need to be conducted in order to confirm the

specificity and localize the site of interaction. Finally, in-vivo studies would be required to assess the successful targeting ability of macrophages by Ab36-cHANPs.

III.V. Reference

1 Kang, L. F., Chung, B. G., Langer, R. & Khademhosseini, A. Microfluidics for drug discovery and development: From target selection to product lifecycle management. *Drug Discovery Today* **13**, 1-13, doi:10.1016/j.drudis.2007.10.003 (2008).

2 Mehta, G., Hsiao, A. Y., Ingram, M., Luker, G. D. & Takayama, S. Opportunities and challenges for use of tumor spheroids as models to test drug delivery and efficacy. *Journal of Controlled Release* **164**, 192-204, doi:10.1016/j.jconrel.2012.04.045 (2012).

3 Sykova, E. & Nicholson, C. Diffusion in brain extracellular space. *Physiological Reviews* **88**, 1277-1340, doi:10.1152/physrev.00027.2007 (2008).

4 Corrado, B. *et al.* A three-dimensional microfluidized liver system to assess hepatic drug metabolism and hepatotoxicity. *Biotechnology and Bioengineering* **116**, 1152-1163, doi:10.1002/bit.26902 (2019).

5 Arias, I. M., Gatmaitan Z Fau - Mazzanti, R., Mazzanti R Fau - Shu, H., Shu H Fau - Kumamoto, Y. & Kumamoto, Y. Structure and function of P-glycoprotein in the normal liver and intestine.

6 Pound, P. & Ritskes-Hoitinga, M. Is it possible to overcome issues of external validity in preclinical animal research? Why most animal models are bound to fail. *Journal of Translational Medicine* **16**, 304, doi:10.1186/s12967-018-1678-1 (2018).

7 Ireson, C. R., Alavijeh, M. S., Palmer, A. M., Fowler, E. R. & Jones, H. J. The role of mouse tumour models in the discovery and development of anticancer drugs. *British Journal of Cancer* **121**, 101-108, doi:10.1038/s41416-019-0495-5 (2019).

8 Zhang, W. T. *et al.* Comparative Study of Subcutaneous and Orthotopic Mouse Models of Prostate Cancer: Vascular Perfusion, Vasculature Density, Hypoxic Burden and BB2r-Targeting Efficacy. *Scientific Reports* **9**, doi:10.1038/s41598-019-47308-z (2019).

9 Van Norman, G. A. Limitations of Animal Studies for Predicting Toxicity in Clinical Trials Is it Time to Rethink Our Current Approach? *Jacc-Basic to Translational Science* **4**, 845-854, doi:10.1016/j.jacbts.2019.10.008 (2019).

10 van de Merbel, A. F. *et al.* An ex vivo Tissue Culture Model for the Assessment of Individualized Drug Responses in Prostate and Bladder Cancer. *Frontiers in Oncology* **8**, doi:10.3389/fonc.2018.00400 (2018).

11 Lewis, D. R. *et al.* Sugar-based amphiphilic nanoparticles arrest atherosclerosis in vivo. *Proceedings of the National Academy of Sciences of the United States of America* **112**, 2693-2698, doi:10.1073/pnas.1424594112 (2015).

12 Park, Y. M. CD36, a scavenger receptor implicated in atherosclerosis. *Experimental and Molecular Medicine* **46**, doi:10.1038/emm.2014.38 (2014).

13 Romano, E., Netti, P. A. & Torino, E. A High Throughput Approach Based on Dynamic High Pressure for the Encapsulation of Active Compounds in Exosomes for Precision Medicine. *International Journal of Molecular Sciences* **22**, doi:10.3390/ijms22189896 (2021).

14 Itskovich, V. V. *et al.* Quantification of human atherosclerotic plaques using spatially enhanced cluster analysis of multicontrast-weighted magnetic resonance images. *Magnetic Resonance in Medicine* **52**, 515-523, doi:10.1002/mrm.20154 (2004).

15 Coradini, D. *et al.* Inhibition of Hepatocellular Carcinomas in vitro and Hepatic Metastases in vivo in Mice by the Histone Deacetylase Inhibitor HA-But. *Clinical Cancer Research* **10**, 4822, doi:10.1158/1078-0432.CCR-04-0349 (2004).

16 Doran, A. C., Meller, N. & McNamara, C. A. Role of smooth muscle cells in the initiation and early progression of atherosclerosis. *Arteriosclerosis Thrombosis and Vascular Biology* **28**, 812-819, doi:10.1161/atvbaha.107.159327 (2008).

17 Kelley, W. J., Safari, H., Lopez-Cazares, G. & Eniola-Adefeso, O. Vascular-targeted nanocarriers: design considerations and strategies for successful treatment of atherosclerosis and other vascular diseases. *Wiley Interdisciplinary Reviews-Nanomedicine and Nanobiotechnology* **8**, 909-926, doi:10.1002/wnan.1414 (2016).

18 Lipinski, M. J., Frias, J. C. & Fayad, Z. A. Advances in detection and characterization of atherosclerosis using contrast agents targeting the macrophage. *Journal of Nuclear Cardiology* **13**, 699-709, doi:10.1016/j.nuclcard.2006.07.004 (2006).

19 Gimbrone, M. A. & Garcia-Cardena, G. Endothelial Cell Dysfunction and the Pathobiology of Atherosclerosis. *Circulation Research* **118**, 620-636, doi:10.1161/circresaha.115.306301 (2016).

20 Grebe, A. & Latz, E. Cholesterol Crystals and Inflammation. *Current Rheumatology Reports* **15**, doi:10.1007/s11926-012-0313-z (2013).

IV. CHAPTER 4 - SURFACE FUNCTIONALIZATION OF HA-BASED NANOPARTICLES FOR GLIOBLASTOMA TARGETING: A CASE STUDY

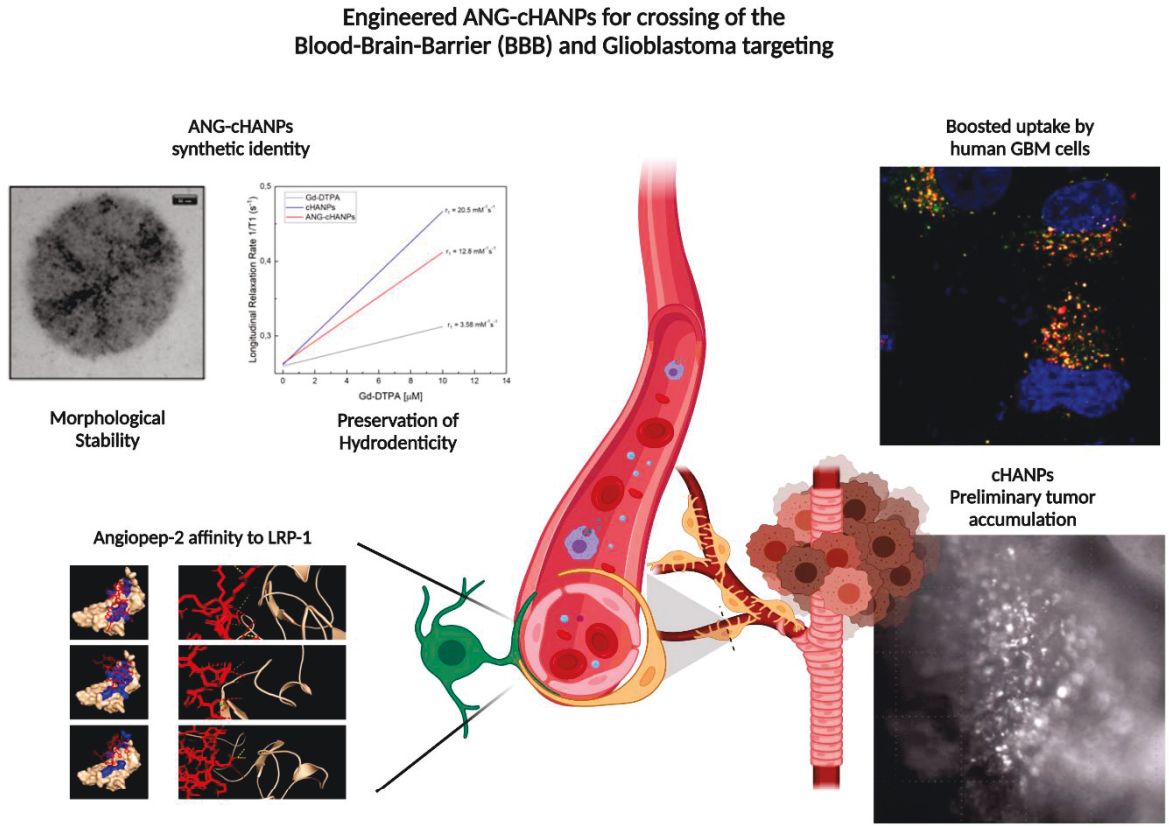

Graphical abstract Chapter 4 – Disease-inspired rational design of theranostic hydrogel-based nanoparticles for earlier diagnosis, effective therapy and more accurate follow up of Glioblastoma Multiforme.

IV.I. Background

In previous chapters the three levels of nano-bio-interactions moving from the definition of a nanocarrier biological identity, to biological identity impact on cellular uptake and nanoparticle transport properties in complex tissues have been evaluated. In this chapter, Glioblastoma Multiforme will be used as a model of disease to identify disease-specific biological barriers, investigate the potential of specifically engineered hydrogel NPs to interact and successfully overcome these barriers *in-vitro*, and preliminary study nanoparticle distribution and tumour accumulation *in-vivo*.

Glioblastoma Multiforme (GBM) or grade IV astrocytoma is the most aggressive malignant brain tumor [1]. The latest guidelines for diagnosis, treatment and tumor volume evaluation were published in 2017 by the European Association of Neuro Oncology (EANO). They defined MRI as the gold standard [2] and the

radiographic appearance of GBM as an enhancing regions around a dark, necrotic core in T1 contrast enhanced images [3].

GBM standard of care is defined by the "Stupp Protocol" that prescribes postoperative chemotherapy with the alkylating agent Temozolomide (TMZ) in combination with radiotherapy [2]. However, TMZ demonstrated beneficial effects in less than 50% of patients and, in particular, those affected by the methylation of the O [6]-methylguanine-DNA methyltransferase (MGMT) promoter. Additionally, GBM cells early develop intrinsic and adaptive TMZ resistance mechanisms which strongly reduce its efficacy [4].

In 2006, the FDA approved the antiangiogenic monoclonal antibody Bevacizumab as adjuvant therapy in patients with severe edema [5] without, however, conferring any benefit in patient prognosis and long term survival, which remain both very poor. Indeed, this pathology is characterized by a late diagnosis, absence of a precise evaluation of treatment efficacy and accuracy of the follow-up, and inability to prevent tumour recurrence [5] with a patient mean survival of only 15 months. The scarce success of the standard of care can be attributed to the presence of two disease-specific biological barriers that currently approved drugs fail to overcome with success, the Blood Brain Barrier (BBB) and the very distinct Tumor Microenvironment (TME). BBB is a physiological diffusional barrier that protects the brain from potentially harmful substances in the systemic circulation. The barrier function of BBB is assured by its anatomical structure, named the Neurovascular Unit (NVU). NVU consists of five major parts: endothelial cell layer, pericytes, immune cells, astrocytes, and basement membrane[6]. Despite the physical filter is represented by highly packed endothelial cells, all these cellular components participate to the barrier homeostasis. BBB severely restricts the passage of substances inside the brain, however there are several routes by which molecules can selectively penetrate inside the brain[7,8]. They can be both passive, regarding mainly neutral molecules not larger than $\sim 400\ \mathrm{Da}$[9], or active, thus involving specific solute carriers. For example, glucose is selectively delivered by the glucose transporter-1 (GLUT-1) for energy production in brain, amino acids cross the BBB using the specific transporters, such as L-type amino acid transporter (LAT)1 and 2[10], and lipoproteins by LRP family receptors[11,12]. Moreover, the landscape characterizing GBM microenvironment is made of physical [13-15], chemical [16], mechanical [17,18] and biological [19-21] barriers, that prevent the accumulation of contrast agents, drugs at therapeutic concentrations, and decrease their therapeutic potential because of multidrug resistance development [16,20,21]. The enhancing portion of the tumor mass observed by MRI is the result of the diffusion of active molecules into the perinecrotic regions of the tumor mass since they are characterized by newly formed and leaky blood vessels with impaired BBB function [22]. GBM diagnosis, treatment and monitoring may therefore be significantly delayed depending on the vascularization of the tumor and may exclude a significant portion of the total mass.

In this framework, nanoparticle-based formulations can play a role in controlling biodistribution, transport properties and transport mechanisms of the active agents for therapy and diagnosis. As discussed, nanoparticles are able to improve drug bioavailability, protect CAs molecules from transmetalation, and, when properly engineered, target active agent molecules specifically at the diseased site using active targeting mechanisms [23]. Indeed, the selection of ad hoc targeting moieties can both trigger specific internalization mechanisms as receptor mediated transcytosis and avoid active agents being substrates of P-efflux pumps, responsible for the major GBM resistance to therapy. These approaches may contribute to effective therapy, earlier diagnosis and more accurate evaluation of treatment efficacy during the follow-up, potentially improving patient outcomes. Finally, several works [13,24,25] are showing the minimal efficacy of the enhanced retention and permeability (EPR) effect in favoring selective accumulation of nanoparticles at the tumor site, above all in the brain. For this reason, a strategy to guarantee sufficient active agent crossing preferably the endothelial layer of the healthy vasculature of the tumor needs to be developed. This evidence becomes even more relevant in GBM where almost 80% of the tumor mass is characterized by a healthy BBB [26], which is further limiting passive transport relevance.

Thus, a fully biocompatible nanovector with ”theranostic” capacities, able to protect active agents from degradation or instability, actively transport and specifically accumulate them at the tumor site, properly modulating their biodistribution, needs be conceived to guarantee the crossing of the BBB and sufficient and selective accumulation in the tumor mass.

Because of the aforementioned drawbacks, alternative treatments to TMZ have been widely explored [27]. Among others, the topoisomerase I inhibitor Irinotecan (CPT-11) showed encouraging results. Indeed, CPT-11 is FDA approved as adjuvant therapy in colon-rectal cancer and its liposomal formulation ONYVIDE™ was approved by the FDA in 1996 for the treatment of metastatic adenocarcinoma of the pancreas. Recently, both in preclinical test and Phase I clinical trial CPT-11 loaded liposomes (NL-CPT11-NCT00734682) have been tested in patients with recurrent malignant glioma. In 2018, Taghizadehghalehjoughi et al., reported that CPT-11 loaded PLGA nanoparticles administered through convection-enhanced delivery in tumor-bearing mice, produced a significant reduction in tumor volume, much higher than free drug in the same concentration [28]. As stated, further benefits in the selective delivery of active compounds overcoming biological barriers can be obtained by triggering an active-targeting approach. Among many routes, targeting receptor-mediated transcytosis can be advantageous since it is possible to exploit the numerous transport proteins exposed by the endothelial layer of the BBB that are physiologically involved in the transport of nutrients. In literature there are several examples of receptors physiologically expressed at the BBB that have been exploited for active targeting. As an example Lam et al.[29], developed Transferrin conjugated liposomes to enhance the transport of temozolomide and a bromodomain inhibitor inside an orthotopic model of human glioma. Results

showed that up to 2% of the injected dose successfully accumulated inside the tumor and that liposomes were able to diffuse in the tumor extracellular matrix moving far from the extravasation site. However, as reported by Protein Atlas[30] where an accurate review of the current knowledge about receptor expression in major organs of the human body is presented, Transferrin receptors as well as Insulin receptors as a second widely explored ligand for BBB crossing, demonstrate high tissue specificity for placenta and pancreas respectively. For this reason, the selectivity of brain accumulation that the use of this receptors might provide is limited.

A receptor that has recently been explored for targeted brain drug delivery is the Low-Density Lipoprotein Receptor-related Protein-1 (LDLRP-1), a 600 kDa member of the low-density lipoprotein receptor family physiologically involved in the transcytosis of many proteins and peptides and contributing to BBB integrity [12]. LRP-1 is highly expressed on BBB and overexpressed on glioma cells [12,31,32] with discrete levels of expression in most of the tissues composing the brain[30]. It is a transmembrane cell-surface protein which is composed of 31 complement type repeats (CRs) grouped in four domains, commonly known as cluster I, cluster II, cluster III and cluster IV. A CR consists of approximately 40 amino acid residues with three disulphide linkages and coordinates one calcium ion. In LRP-1, CR56 in clusters II, and the CR17, in Cluster III, have been identified as the major ligand-binding sites[33,34].

In 2008, Demeule et al., designed the synthetic peptide Angiopep-2 as the most efficient combination of the common aminoacidic sequences of the physiological substrates of LRP1 (e.g. ApoE, aprotinin) showing the highest transcytosis capacities on a BBB in-vitro model [35], and the ability to escape P-efflux pumps [36].

Recently, the same group brought Angioepep-2 in clinical trials with the formulation ANG1005[37], a drug-peptide conjugate that is able to enhance the transport of paclitaxel in brain tumors and metastasis through transcytosis mechanism that they demonstrated to involve LRP-1 receptors.

In this chapter, we address the limitations of the current diagnosis, treatment and monitoring of GBM, exploiting the principle of Hydrodenticity in the design of Angiopep-2 engineered Theranostic crosslinked Hyaluronic Acid Nanoparticles (Thera-ANG-cHANPs). Angiopep-2 affinity with the LRP-1 receptors will be assessed though flexible molecular docking by Autodock Vina, with particular regard to the impact that its surface conjugation might have on the peptide targeting ability. Thera-ANG-cHANPs serum stability will be investigated and NPs improved cellular uptake will be demonstrated in both standard and patient derived human glioma cells. Transport mechanism and therapeutic potential of Thera-ANG-cHANPs will be elucidated *in-vitro.* Finally, preliminary tumor accumulation of cHANPs in an orthotopic human model of glioma will be presented.

IV.II. Experimental Section

IV.II.I. Materials

(3-Dimethylaminopropyl)-N'-ethyl carbodiimide hydrochloride EDC (molecular formula $C8H17N3{\cdot}HCl$; M_w= 191,70 Da), N-Hydroxysuccinimide NHS (molecular formula $C4H5NO3$; M_w=115,09 Da) were purchased from Merck KGaA (Germany). Irinotecan (CPT11; M_w=652 Da) was purchased from Aurogene srl (Italy). Angiopep-2 (TFFYGGSRGKRNNFKTEEY, M_w = 2625.8 Da) was purchased from ProteoGenix SAS (France). QuantiPro™ BCA Assay Kit was purchased from Sigma Aldrich (St. Louis, Missouri, USA). The human glioblastoma cell line U87 (passage 15-36) was purchased from ATCC (Virginia, USA). Dulbecco Modified Eagle Medium high glucose (DMEM), Fetal Bovine Serum (FBS), Phosphate Buffer Saline (PBS) and Human Serum Albumin (HSA) for cell culture and in-vitro studies were purchased by Sigma Aldrich Co. (St. Louis, Missouri, USA). The Water, used for synthesis and characterization, was purified by distillation, deionization, reverse osmosis (Milli-Q Plus) and finally filtered with a 0,22 µm cutoff filter. Theranostic crosslinked hyaluronic acid nanoparticles (Thera-cHANPs) and Polyethylene glycol crosslinked hyaluronic acid nanoparticles (PEG-cHANPs) were synthesized as discussed in the previous chapter.

IV.II.II. Angiopep-2 3D structure prediction

As described in the background section, Angiopep-2 is a 19-aminoacids peptide (TFFYGGSRGKRNNFKTEEY) that has been designed to specifically interact with LRP-1 receptors which are of great interest for the crossing of the Blood-Brain-Barrier.

As a very novel peptide, Angiopep-2 (ANG-2) 3D model is not available in standard databases. For this reason, to perform the molecular docking simulation and study its interaction with the LRP-1 receptors, its three-dimensional structure is obtained by the software PEP-FOLD3. PEP-FOLD3 allows the determination of the 3D structure of linear peptides of 5–50 amino acids in aqueous solution. The folding process proceeds by the addition of one amino acid at time along the whole amino acidic sequence and assures a very high reliability, with a deviation of only 3.3Å from the experimental conformation[38]. As a result of the prediction, five out of the most probable conformations are extracted and a probability of folding structures (e.g. alpha-helix, β – sheets) in a 2D plot is presented, Figure 4.1.

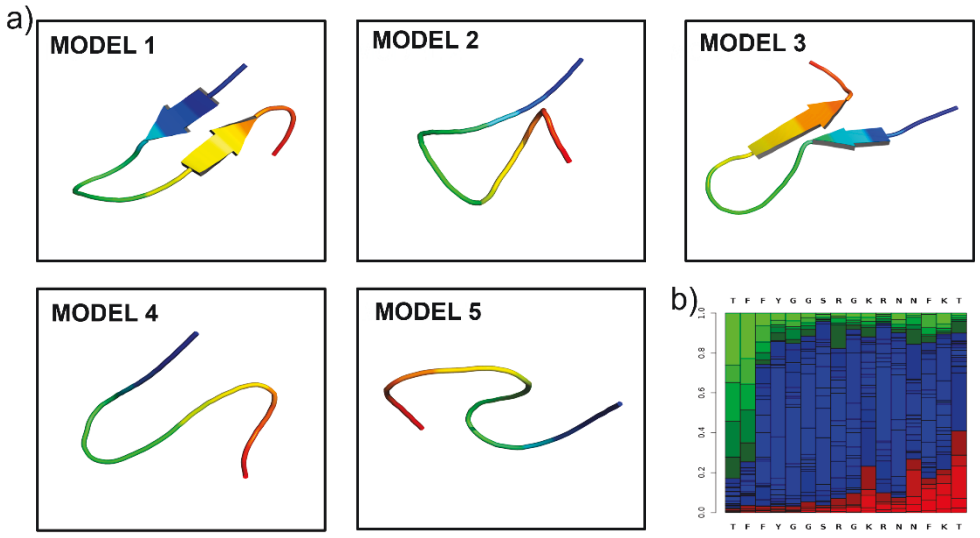

Figure 4.1 – Presiction of Angiopep-2 3D folding by PEP-FOLD3. A) Five most probable 3D conformations of Angiopep-2; b) 2D plot of folding probability in alpha-helix (green), ß-sheet (red), o others (blue).

IV.II.III. Relevance of LRP-1 CR56 and CR17 in ligand-bonding

It has been reported that different local charge distributions are of fundamental importance for the specificity of the bonding of ligands to specific CR in LRP-1. Indeed, despite their similarity given by the very short amino acidic sequence and their open loop structure, each CR guarantees specificity against ligands mainly by different contour surfaces and charge distributions[33].

The double module of complement type repeats CR56 is the portion of LRP-1 in the cluster II binding site that is responsible of the specific interaction with many ligands such as the Receptor Associated Protein (RAP). The RAP is an endoplasmic reticulum (ER) resident protein that is required for the effective recycling of LRP to the cell surface and for this reason it is involved in the transcytosis process. Indeed, it prevents the premature interaction between the receptor and its ligands in the ER, thereby preventing the receptor from being degraded in lysosomes[39]. LRP-1 – RAP bonding has been extensively studied and CR56 of complex II has been identified as the main site of the bonding[33].

CR17 in cluster III is reported as the major binding site for apolipoprotein and specifically for ApoE[40]. Lipid association of ApoE can enhance receptor binding by several mechanisms. Since multiple copies of ApoE are embedded in lipoprotein particles, strings of CRs could bind to several ApoEs at once, creating an avidity effect [41]. Guttman et al.[40], demonstrated that the ApoE helix contacts CR17 on the side rather than directly at the calcium binding site, as instead happens for RAP1 binding in CR56.

The flexible docking of the novel peptide Angiopep-2 with the CR56 (PDB ID: 2FYL) and CR17 (PDB ID: 2KNX) is performed to energetically characterize the ANG-LRP1 bonding and understand whether this bonding might trigger a reduced lysosomal degradation of ANG-2 substrates.

IV.II.IV. Flexible docking by Autodock Vina

AutoDock is a suite of automated docking tools. It is designed to predict how small molecules, such as substrates or drug candidates, bind to a receptor of known 3D structure. Current distributions of AutoDock consist of two generations of software: AutoDock4 and AutoDock Vina. Autodock Vina achieves significant improvements in the average accuracy of the binding mode predictions, while being up to two orders of magnitude faster than AutoDock4[138] and for this reason it has been chosen for simulations. As a result of docking, the energy of the bonding in kcal/mol as well as the most probable binding site(s) for a ligand are provided. To gain information about the nature of the bonding as well as the residues involved, the open-source software PyMOL and in particular OpenGL Extension Wrangler Library (GLEW) and FreeGLUT plug in able to solve Poisson-Boltzmann equations using the Adaptive Poisson Boltzmann Solver[144], were used. The operating procedures were made as follows: (1) Load the Molecule in format .pdb and remove the water from the molecule 3D model; (2) Select the macromolecule and obtain the coordinates with the tool Gridbox; (3) Save in format .gpf the grid settings; (4) List Receptor and Ligand filename and insert macromolecule center coordinates; (5) Select 10 as number of tries; (6) Choose the exhaustiveness (accuracy of the simulation). To analyse the obtained results, (1) Load result file in Pymol; (2) change the visualization of the molecules in *stick and balls*; (3) select the function *show residues*; (4) Select the legacy plug-in *show contact;* (5) select the atoms involved in the binding and export the list of the involved residues as a .xls file. The residues involved in the bonding were selected as statistically relevant or not. This selection was performed by building a gaussian distribution for each simulation representing the probability of occurrence of each bonding among different trials. All the bonds with a probability of occurrence included in 3 times the standard deviation of the gaussian distribution were selected as statistically relevant (please note that this procedure led to select as statistically relevant almost 98% of the residues identified by Autodock).

IV.II.V. 4.2. Synthesis of co-loaded ANG-cHANPs

Angiopep-2 is conjugated to nanoparticle surface through the amidation reaction of free carboxyl groups of cHANPs and amine groups of Angiopep-2. 500 µL of cHANPs suspension containing

5x10^8/mL NPs, is added to an aqueous solution of EDC (0.02M) and NHS (0.006M) and let react for 10 min under continuous wheel stirring to activate available carboxyl groups. Then, Angiopep-2 (50µg/mL) is added and the suspension is continuously wheel stirred prior purification.

The procedure is optimized by testing the addition of different concentrations of Angiopep-2 and different contact times to maximize the efficiency of the reaction. The purification from unreacted peptide is performed either by ultracentrifugation (UC) or by centrifugation in Corning® Spin-X® UF Concentrators (CC) with a MWCO of 30 kDa or 50 kDa by Corning (New York, USA).

The quantitative BCA assay is used to measure the amount of peptide successfully bound to cHANPs. Typically, 150 µL of sample and 150 µL of buffer solution are put in a 96 well-plate, and let react for 1h at 60°C. Therefore, the absorbance of purified samples is measured at 562 nm and the amount peptide in the sample quantified through a calibration curve (0.5-30 µg/mL). The absorbance of bare cHANPs (7,5 x 10^7 NPs/mL) is measured for each batch and subtracted to the absorbance of ANG-cHANPs at the same concentration prior to quantification.

Triplicates of different dilutions of the samples (1:2, 1:5, 1:10) are measured in order to confirm the repeatability of the measurement and to average the effect of measuring a suspension that is likely subjected to inter-measurement variability. The efficiency of the conjugation reaction is calculated dividing the measured amount of peptide in the purified sample by the one added initially.

IV.II.VI. Quantification of Carboxyl groups of HA

Titration method was used to quantify the amount of carboxyl groups of HA and compare it with theoretical calculation. 1 µL of NaOH (1mM) was added to a HA (10mg/mL) solution and after 1 minute stirring pH was measured. After each titrant addition, solution was stirred, and pH measured. Starting from the NaOH amount added at the equivalence point the molar concentration of carboxyl groups was calculated.

IV.II.VII. Preliminary In-vivo studies

Biodistribution in Healthy Mice

BALB/c nude mice (6-8-week years old) were provided access to food and water ad libitum and were hosted in the animal facility at the Erasmus MC (Rotterdam, The Netherlands). All experiments were performed according to the guidelines for animal care of the Erasmus MC Animal Experiments Committee. Co-loaded cHANPs (60 uM of Gd-DTPA) were systemically injected via tail vein and animal sacrificed 4h and 8h after injection. Organs

were harvested for ex-vivo fluorescence evaluation by IVIS spectrum imager (model, Perkin Elmer) and biodistribution was assessed.

Tumor accumulation in human orthotopic model of glioma

BALB/c nude mice (6-8-week years old) were provided access to food and water ad libitum and were hosted in the animal facility at the Cheinge (Naples, Italy). All experiments were performed according to the guidelines for animal care of the Cheinge. Intracranial imaging window was surgically implanted on mouse brain for high resolution, online optical imaging of the tumour. Co-loaded cHANPs were injected both retro-orbitally ($c_{ATTO488}$ = 2.3 $nmol/mL$) as an alternative, BBB-bypassing route of administration and systemically ($c_{ATTO488}$ = 1 $nmol/mL$). 4h post injection particle accumulation at the tumour was observed.

IV.III. Results

IV.III.I. 3.1 Protein-protein flexible docking: Angiopep-2 bonding to CR56

LRP-1 is a 600kDa protein overexpressed at the endothelial layer of the BBB and involved in the physiological transport of lipoprotein inside the central nervous system. It is composed of four different clusters, with cluster II and III being the major responsible for ligand bonding.

The double module complement type repeats CR56 constitutes the ligand binding site of the cluster II and is composed of 82 residues, from Ser932 to His1013[33]. In particular, CR5 involves the acidic residue Asp959 which does not coordinate calcium. This residue has been proven to be involved in Receptor associated protein (RAP) bonding and for this reason it is considered an active player in selective ligand binding and transcytosis[33].

CR56 3D model was used to perform flexible docking simulations with all five ANG-2 models, and results were compared both in terms of binding site, binding energy and nature of the bonding. Figure 4.2 visually reports results of the simulation showing similar regions of LRP-1 involved in the bonding for each of the ANG-2 model. Binding energies and LRP-1 residues involved are reported in Table 1. Results show that all the models interact very similarly with CR56, with high binding energies characterized by a mean of -5.68 ± 0.6 kcal/mol except for the model 2 showing a higher binding energy that however correlates with a higher standard deviation (7.8 ± 1.2).

Moreover, docking results showed that each ANG-2 model binds ASP 959 of CR5 and that the bonding occurs through electrostatic clashes that characterize 29% of the total bonds. This result

confirms that ANG-2 bonding to LRP-1 triggers a transcytosis mechanism[36] and that this selective bonding occurs by means of electrostatic interaction, as previously reported[33].

As second step, ANG-2 residues involved in LRP1 bonding were analysed and results showed that almost all ANG-2 residues bind LRP1 (Figure 4.3). This is not a surprising result considering how this synthetic peptide has been designed. Indeed, Demeule et al.[35] obtained the aminoacidic sequence of ANG-2 by comparing the sequences of physiological substrates of the receptor and choosing the common moieties. For this reason, each ANG-2 residue should be equally involved in the bonding of the receptor. The main consequence of this result is that the combination of Angiopep-2 with a drug delivery system that requires the chemical bonding of some moieties of the peptide to the DDS, should not negatively impact on its targeting ability.

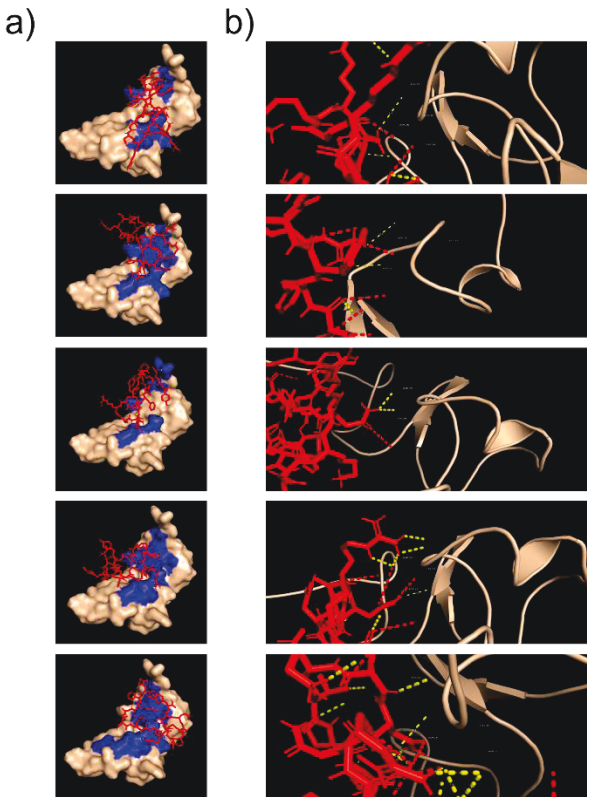

Figure 4.2 - Simulation of Angioepep-2/CR56 bonding: Molecular Docking results. a) 3D representation of Angiopep-2 binding site on CR56 (in blue); b) details of Angiopep-2/CR56 bonding (dotted line in yellow represent Pi-interaction, in red electrostatic clashes).

Table 1 - table reporting average binding energies for each Angiopep-2/CR56 bonding; list of all Angiopep-2 residues involved in the binding and bond classification.

	Binding Energy ΔG [=] Kcal/mol	Pi-interaction	Electrostatic clashes
Model 1	-5.25 ± 0.2	16ARG, 27ASP, 28ASP, 30CYS, 62ANS, 70ASP, 80CYS	28ASP, 29ASP, 70ASP
Model 2	-7.8 ± 1.2	16ARG, 27ASP, 28ASP, 62ANS, 63TRP, 64ARG, 70ASP, 71CYS, 80CYS	29ASP, 62ANS, 70ASP, 80CYS
Model 3	-5.12 ± 0.2	16ARG, 28ASP, 29ASP, 62ANS, 65CYS, 80CYS, 82HIS	16ARG, 29ASP, 62ANS, 65CYS, 80CYS, 82HIS
Model 4	-5.22 ± 0.4	16ARG, 28ASP, 29ASP, 30CYS, 58CYS, 62ANS, 63TRP,70ASP, 71CYS, 80CYS	28ASP, 29ASP, 58CYS, 62ANS,70ASP, 71CYS, 80CYS
Model 5	-5.05 ± 0.3	16ARG, 17CYS, 25ASP, 27ASP, 28ASP, 29ASP, 30CYS, 58CYS, 63TRP,70ASP, 71CYS	17CYS, 27ASP, 28ASP, 29ASP, 70ASP, 71CYS, 80CYS

Finally, Models 1 and 3 displayed a major persistence of specific amino acids between trials and the reason for that might be related to the folding associated to each of these models. Being the bonding based on electrostatic and hydrophobic interaction, those folding might have facilitated the interaction of these specific amino acids over the others.

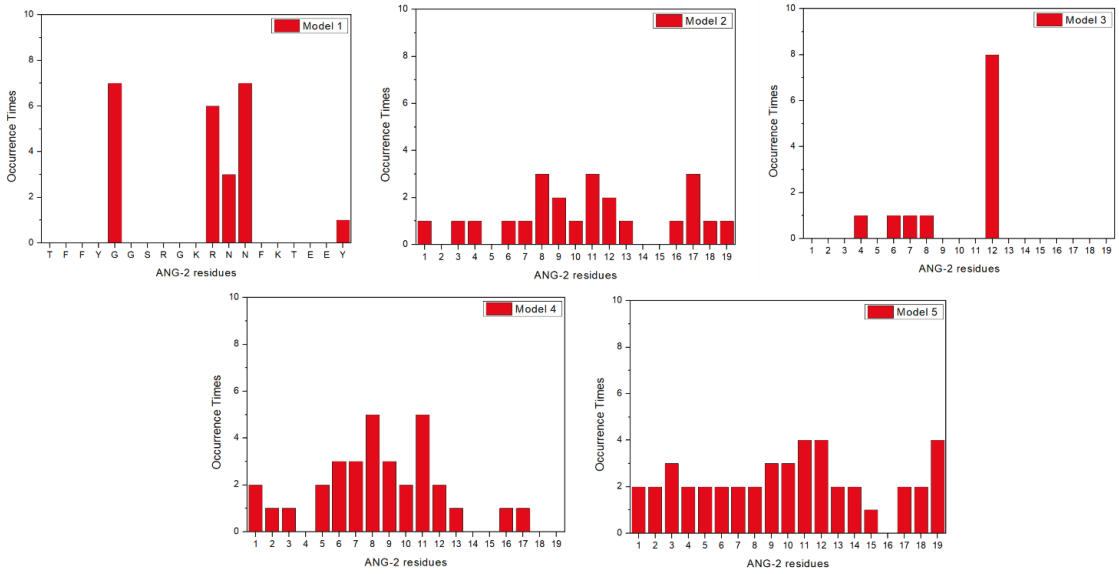

Figure 4.3 – Angiopep-2 residues involved in LRP-1 bonding

IV.III.II. 3.2 Protein-protein flexible docking: Angiopep-2 bonding to CR17

Regarding lipoprotein internalization, LRP1 shares relevant interacting moieties with other receptors of the LDL family, such al LRP3[40]. The common subdomains CR16-18 show high affinity towards ApoE (130-149), with the highest affinity for the single repeat CR17. This bonding has been widely characterized and revealed a similar motif seen previously in other ligand CR interactions, in which lysine residues of the ligand interact with the calcium binding site of the

CR. It has been speculated that the decrease in calcium concentrations within the endosome plays a role in ligand dissociation as the calcium affinity for certain CRs significantly weakens at lower pH[42].

CR17-ANG-2 flexible docking was performed for all the 5 models of ANG-2. As for CR56, Figure 4.4 visually reports results of the simulation showing similar regions of LRP-1 involved in the bonding for each of the ANG-2 model. Binding energies and LRP-1 residues involved in the bonding are reported in Table 2. Results show a slightly reduced binding energy of ANG-2 to CR17 with respect to CR56 being the average binding energy - 5.3 ± 0.62. Also in this case, all models show a similar binding energy, except for model 2 displaying higher binding energy and standard deviation (- 8 ± 1.46).

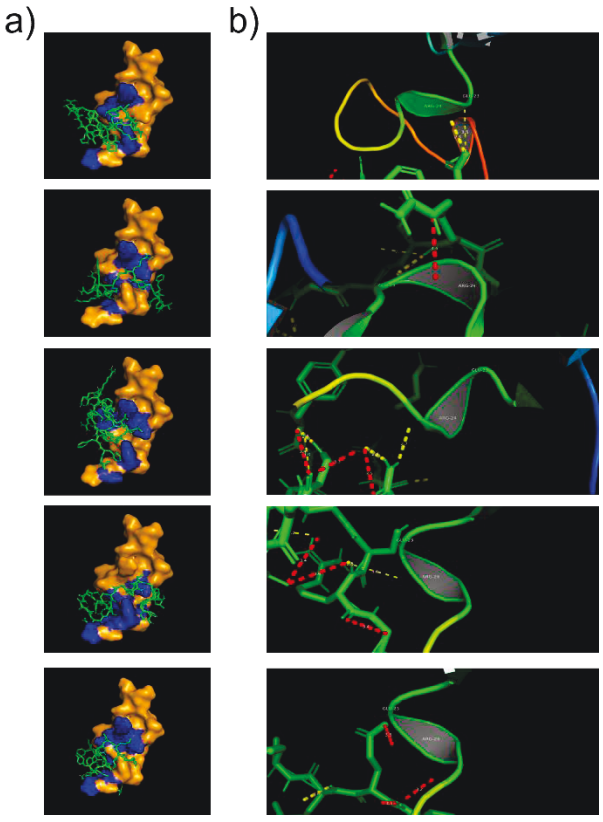

Figure 4.4 - Simulation of Angioepep-2/CR17 bonding: Molecular Docking results. a) 3D representation of Angiopep-2 binding site on CR17 (in blue); b) Details of Angiopep-2/CR17 bonding (dotted line in yellow represent Pi-interaction, in red electrostatic clashes)

Table 2 - Table reporting average binding energies for each Angiopep-2/CR17 bonding; list of all Angiopep-2 residues involved in the binding and bond classification.

	Binding Energy ΔG [=] Kcal/mol	Pi-interaction	Electrostatic clashes
Model 1	-4.77 ± 0.2	17THR, 41ILE, 50THR, 24ARG, 47TYR,27CYR, 28ASP	17THR, 41ILE, 50THR, 27CYS, 28ASP
Model 2	-8 ± 1.4	11SER, 13SER, 27CYS, 39GLU, 41ILE, 48ASN, 43ALA, 23GLU, 24ARG	11SER, 13SER, 27CYS, 39GLU, 41ILE, 48ASN, 43ALA, 23GLU, 24ARG
Model 3	-5.05 ± 0.17	24ARG, 28ASP, 29GLY, 30ASP, 49SER, 23GLU, 47TYR	28ASP, 29GLU
Model 4	-4.48 ± 0.57	23GLU, 27CYS, 39GLU, 40SER, 44GLY, 47TYR, 48ASN, 50THR	23GLU, 27CYS, 39GLU, 47TYR, 48ASN, 50THR
Model 5	-4.44 ± 0.74	23GLU, 24ARG, 26LEU, 28ASP, 39GLU, 41ILE, 48ASN, 50THR	23GLU, 24ARG, 26LEU, 28ASP, 39GLU, 41ILE, 48ASN, 50THR

At the analysis of the nature of the bonds, it can be observed that, despite very similar binding energies, the relative amount of pi-interaction and electrostatic clashes is significantly different among different models. Additionally, it was not possible to identify a pattern, or a specific residue sequence involved in the bonding and for this reason it appears that CR17-ANG2 interaction is less site specific than CR56-ANG2. Examining the results obtained for ANG2 residues involved in the interaction with CR17, Figure 4.5 reveals that in almost all models the majority of amino acids is involved in the bonding and that, as before, model 1 and 3 display the preferential interaction with specific amino acids. Also in this case, a reduced availability of some residues due to the folding of the peptide can be identified as the cause.

As previously stated, ApoE interacts with LRP1 though lysine residues that coordinate calcium ions. This interaction weakens in endosomes and cause the endosomal release of the receptor. ANG-2 presents two lysine residues in its sequence that are always involved in the binding, even in models 1 and 3. Whether CR17-ANG2 bonding might mimic the CR17-ApoE bonding leading to endosomal degradation of ANG-2 instead of transcytosis is still unclear.

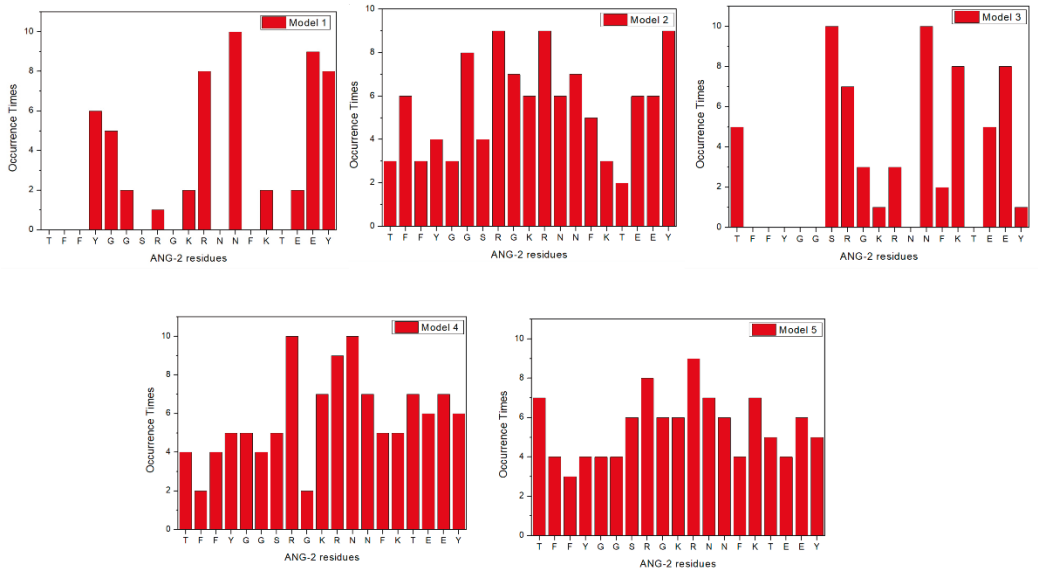

Figure 4.5 – Angiopep-2 residues involved in LRP-1 bonding

IV.III.III. Engineered hydrogels for brain delivery: ANG-cHANPs production and characterization

Crosslinked hyaluronic acid nanoparticles (cHANPs) co-loaded with the metal chelate Gd-DTPA and the fluorophore ATTO 488 are produced in microfluidics by nanoprecipitation through a hydrodynamic flow focusing regime in standard operative conditions as described in Chapter 1. Briefly, nanoparticles are produced in a microfluidic X-junction chip where the solvent solution of HA and active agents (Gd-DTPA and ATTO 488 or ATTO 633 alternatively) is fed in the middle channel and the non-solvent solution made of acetone and DVS, in the side channels.

Theranostic cHANPs (Thera-cHANPs) co-encapsulating CPT-11 and Gd-DTPA are produced through a cosolvation strategy, adding 10% *V/V* of ethanol and 0.025% *w/V* of CPT-11 at to the solvent solution of HA and Gd-DTPA because of low CPT-11 water solubility (~1 mg/mL). Solvent solution is injected in the middle channel at 27 µL/min. As in the other experiments, acetone and DVS are fed in the side channels as non-solvent solution at 110 µL/min.

Both cHANPs and Thera-cHANPs were conjugated with the 19 amino acid peptide, Angiopep-2, which confers a dual-targeting ability to the nanostructures[43,44]. The procedure was optimized by testing the addition of different concentrations of Angiopep-2 and different reaction times. The addition of 50 µg of peptide per mL of suspension after 4 h of contact, reveals the highest amount of bound peptide (27.63 µg/mL) and an efficiency of the bioconjugation reaction of 55.27%.

To assess the stability of nanoparticles against Angiopep-2 conjugation, a morphological analysis on Angiopep-2 decorated crosslinked hyaluronic acid nanoparticles (ANG-cHANPs) is conducted by TEM, as reported in Figure 4.7a. Particle Size Distribution (PSD)was measured by DLS both for

conjugated and bare particles and reported in Figure 4.7b. ANG-cHANPs in Figure 4.7a clearly show changes in the morphological structure of the particles probably promoted by the peptide, which, during the reaction, is bound not only to the external surface but also partially to the internal hydrogel network. The significant increase in the mean size of nanoparticles pre and post bioconjugation reported in Figure 4.7b by DLS analysis can be attributed to hydrogel swelling due to bioconjugation. When conjugated to angiopep-2, uncrosslinked polymer chains of nanoparticles are sliding one on the other producing an increase in size. Indeed, the PSD shows an increase in the mean diameter of the nanoparticles from about 150 nm to 300 nm after the bioconjugation. It is also important to point out the DLS measurement could reasonably overestimate the hydrodynamic radius of nanoparticles as reported previously by Stetefeld et al. [44]. Indeed, the measured size could be related to the slower diffusion of water layer surrounding the nanoparticles and induced by the extension of the peptide in the continuous medium, leading to increased apparent mean size. This effect has been already reported by Silva et al. [45], who observed for chitosan/alginate nanoparticles a significant mismatch between the hydrodynamic radius measured by DLS and the size of nanoparticles observed at TEM in a dried state. The overestimation of size by DLS has been similarly discussed.

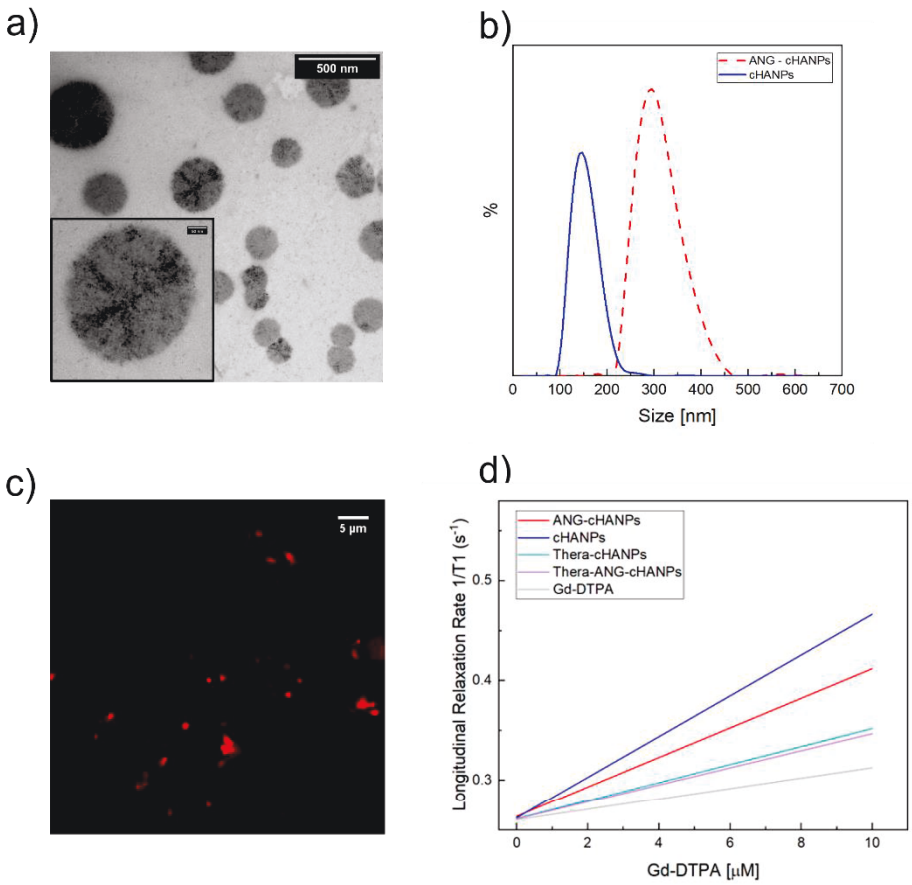

Figure 4.7 – Angiopep-2 decorated crosslinked hyaluronic acid nanoparticles (ANG-cHANPs) characterization. (a) TEM image of ANG-cHANPs; (b) PSD of cHANPs and ANG-cHANPs; (c) Confocal images of ANG-cHANPs; (d) Relaxivity of cHANPs, ANG-cHANPs, Thera-cHANPs and Thera-ANG-cHANPs

To study the effect of the conjugation reaction on the encapsulation and stability of payload agents, the encapsulation efficiency (EE%) of both Gd-DTPA, ATTO 488 and irinotecan is calculated for cHANPs, ANG-cHANPs, Thera-cHANPs and Thera-ANG-cHANPs. Table 3 summarizes the results showing that all the loaded compounds are retained inside ANG-cHANPs and Thera-ANG-cHANPs with a partial loss of about 50% with respect to cHANPs. The loss of cargo may be attributed to the re-arrangement of the hydrogel network during the bioconjugation reaction that we discussed in the previous section, causing the swelling of the hydrogel, the imbibition of water and diffusion of some molecules out of the hydrogel[45].

Table 3. Co-loaded cHANPs, ANG-cHANPs Thera-cHANPs and Thera ANG-cHANPs characterization.

	Particle Size [nm]	Zeta Potential [mV]	Gd-DTPA [µM]	Gd-DTPA EE%	ATTO 488 [µM]	ATTO 488 EE%	Irinotecan [µM]	Irinotecan EE%
cHANPs	149.99±29.8	−33.8 ± 4.25	12.02	3.59	0.26	16.5	-	-
ANG-cHANPs	305.6 ±60.7	−36.3 ± 3.45	5.3	-	0.152	-	-	-
Thera-cHANPs	106.79 ± 46.33	−15.4 ± 6.96	8.11	2.67	-	-	155.46	19.43
Thera-ANG-cHANPs	362 ± 48.40	−7.14 ± 6.05	2.64	-	-	-	65.85	-

Confocal image of ANG-cHANPs is presented in Figure 4.7c to localize the presence of ATTO 488 inside nanoparticles by the observation of fluorescent spots. Because of the low spatial resolution of the optical light, the dimension of the spots does not correlate with the actual particle size. These observations confirmed that ATTO 488 is retained in ANG-cHANPs.

IV.III.IV. Effect of Angiopep-2 conjugation on ANG-cHANPs and Thera-ANG-cHANPs relaxivity

The ability of hydrogel matrices to boost the relaxivity of Gd-chelates has been widely described by the Hydrodenticity theory.

We just reported that the bioconjugation reaction with angiopep-2 promotes a variation in morphology of ANG-cHANPs and a partial loss of co-loaded compounds. In this section, evaluating the relaxivities of cHANPs, ANG-cHANPs, Thera-cHANPs and Thera-ANG-cHANPs we aim to understand if the aforementioned changes in structural parameters of the polymer network influence the Hydrodenticity effect.

Figure 4.7d presents the relaxation rates in s^{-1} of cHANPs and ANG-cHANPs, both significantly higher than the relaxation rate of free Gd-DTPA. Indeed, cHANPs and ANG-cHANPs show a relaxivity of 20.32 $mM^{-1}s^{-1}$ and 12.08 $mM^{-1}s^{-1}$, which are respectively 5.67 and 3.38 folds higher than the relaxivity of free Gd-DTPA (3.58 $mM^{-1}s^{-1}$).

As already reported by Russo et al., the structural parameters of the polymer network that play a major role in tuning the Hydrodenticity effect are the crosslinking density and the mesh size of the hydrogel. Therefore, we can hypothesize that the lower relaxivity of ANG-cHANPs may be due to the presence of angiopep-2 in the bulk of nanoparticles and to the rearrangement of the structure, which is affecting the mesh size, thus changing the resulting relaxivity.

Overall, results demonstrate that, despite the establishment of a new equilibrium in the crosslinked matrix of the hydrogel network and the reduced amount of Gd-DTPA in ANG-cHANPs, a significant relaxivity boosting is still present. For this reason, we can confirm that ANG-cHANPs and Thera-ANG-cHANPs still preserve the Hydrodenticity effect.

IV.III.V. Stability of ANG-cHANPs in Culture Medium and Quantitative Uptake by U87 and GS-102 Cells

The uptake of cHANPs and ANG-cHANPs by two human glioblastoma cell lines was quantified by flow cytometry. Firstly, U87-MG cells were used as well-established in vitro model of human glioblastoma and secondly serum-free cultured patient-derived primary glioblastoma stem-like cells (GS-102) were used to confirm results on cells more closely resembling the original tumor molecular profile[46-48]. As previously published, serum-free 2D culture on ECM allows attachment of the GS-102 cells preserving cell molecular features and reliable viability assessment. This allows rapid screening of candidate therapies and reliable comparison of efficacy with the 2D culture providing similar results to 3D floating neurospheres[48].

As first step, the stability of cHANPs and ANG-cHANPs in culture medium at 37 °C is investigated.

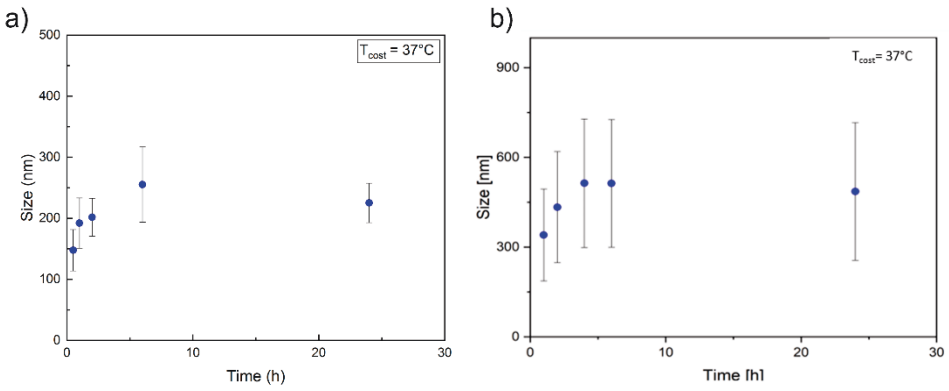

Figure 4.8 – Serum stability of cHANPs and ANG-cHANPs. a) Mean size variation of cHANPs up to 24h in culture medium (10% FBS); b) Mean size variation of ANG-cHANPs up to 24h in culture medium (10% FBS)

Figure 4.8 reports the variation of the mean size of cHANPs and ANG-cHANPs over time up to 24 h. For ANG-cHANPs, in the first 4 h, the mean size increased from 300 to 550 nm. This effect can be attributed to the dynamic formation of a protein corona on the nanoparticle surface, increasing

the measured hydrodynamic radius. Recently, Yu et al. demonstrated that the protein corona absorbed on hydrophilic nanoparticles undergo quick and frequent exchanges with proteins in solution, displaying a highly dynamic behaviour[49]. This continuous exchange should avoid that the protein corona, masking the nanoparticle surface, affects the interaction of angiopep-2 with cells. The same analysis for cHANPs confirms the stability of nanoparticles in culture medium at 37 °C up to 24 h as reported in Chapter 2.

As a consequence, our nanoparticles can preserve their original physicochemical properties in a physiological system, as confirmed by the in vitro experiments reported in the next figure (Figures 4.9 a–c).

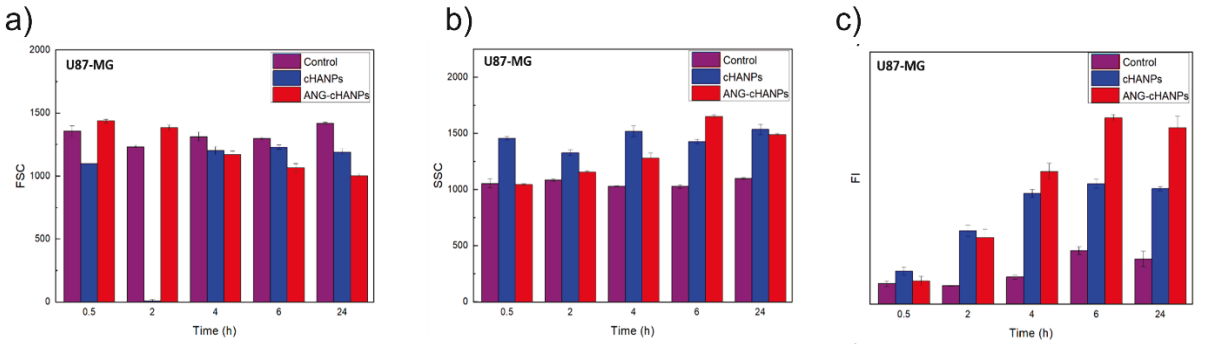

Figure 4.9 – Flow cytometry measurement for cHANPs and ANG-cHANPs uptake quantification by U87 cells. a) Forward scattering (FSC) of U87 after incubation with cHANP and ANG-cHANPs; (b) Side scattering (SSC) of U87 cells after incubation with cHANPs and ANG-cHANPs; (c) Fluorescence intensity (FI) of U87 cells after incubation with cHANPs and ANG-cHANPs

Different studies in literature try to elucidate the effect of size on the internalization of nano/microparticles. However, the attribution of the predominant role in the NP internalization to the complete synthetic identity of NPs (composition, charge, size and surface modification) is the common finding. Despite this, it has been found that nanoparticles in the range of 200 nm to 1 µM in size (where both cHANPs and ANG-cHANPs lie) are mainly internalized by endocytosis and in particular by micropinocytosis mechanisms[50]. To elucidate about this, cHANPs and ANG-cHANPs are incubated with U87-MG cells and fluorescence intensity (FI), measured in flow cytometry at different time points, is reported in Figure 4.9c. Both cHANPs and ANG-cHANPs display a significantly higher fluorescence than control at any time point. For short times (i.e., up to 4 h), a linear increase in fluorescence is observed, with ANG-cHANPs showing a higher slope. Salvati et al.[51] reported that a linear increase in fluorescence is typical of energy-dependent endocytic uptake of nanoparticles characterized by stable fluorescent labeling. Indeed, in the presence of labile dye, a sudden increase in fluorescence and a sharp drop in the very first hours would be observed. After 4 h of contact, cHANPs fluorescence reaches a plateau, remaining almost unmodified up to 24 h. In the same work, Salvati et al. identified this plateau as an equilibrium

condition in which the internalization process saturates and nanoparticles reach lysosomes [51]. On the other hand, ANG-cHANPs fluorescence continuously increases, indicating a different uptake mechanism, which is not saturated in the first 4 h of contact. This observation is in accordance with Bertrand et al.[36] who reported that the uptake mechanism of Angiopep-2 is a receptor-mediated transcytosis by LRP-1 receptors. In addition, the difference in the slope of the linear uptake of the very first hours, confirms a difference in the uptake rate, thus in the underlying uptake mechanism, which is much faster for ANG-cHANPs than cHANPs. Both for cHANPs and ANG-cHANPs at 24 h, a slight decrease in fluorescence intensity can be observed. This phenomenon can be attributed to cell division and thus nanoparticle redistribution in daughter cells[51].

All the observations are supported by FSC and SSC measurements reported in Figures 4.9b,c, respectively. FSC decreases over time and SSC increases with the same trend observed in fluorescence intensity. These effects are well described by Jochums et al.[52] who reported that nanoparticles located inside the cell, similarly to granulocytes, generate an increase in the SSC intensity in a dose-dependent manner so that the addition of nanoparticles to the cytoplasm can cause increased SSC and decreased FSC.

To confirm the involvement of Angiopep-2 and of an energy-dependent mechanism in the uptake of ANG-cHANPs, we quantified ANG-cHANPs internalization in ATP-depleted cells and in competition with excess of Angiopep-2. Internalization was quantified by measuring single cell fluorescent intensity by flow cytometry at 4 h, 8 h and 24 h of incubation. Results in Figure 4.10, as expected, reveal that the depletion of ATP and the treatment of cells with angiopep-2 caused a decrease in Fl intensity with respect to untreated cells, due to less internalized nanoparticles. Already at 4 h of incubation, both in ATP-depleted cells and angiopep-2 treated cells the fluorescence intensity is strongly reduced and at 24 h and this reduction reaches 71% and 82%, respectively. These results confirm the involvement of both an energy dependent-mechanism and the peptide Angiopep-2 in the internalization of ANG-cHANPs.

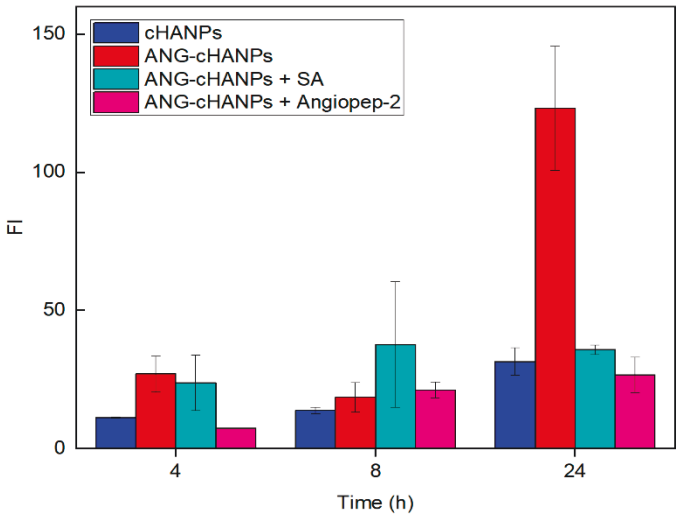

Figure 4.10 – Fluorescent Intensity (FI) of U87 cells after co-incubation with ANG-cHANPs and sodium azide (SA) to deplete cellular ATP, and excess of angiopep-2 for the competitive binding of low density lipoprotein receptor related protein-1 (LRP-1) receptors

The study of NPs uptake by flow cytometry was then conducted on patient-derived GS-102 cells and FI in Figure 4.11a reveals that a significant uptake both of cHANPs and ANG-cHANPs can be observed with a delay of 6 h with respect to U87-MG cells. Despite this time lag, at 24 h an exponential increase in fluorescence, more pronounced for ANG-cHANPs than cHANPs, is present. These results, which are in accordance with SSC and FSC measurements presented in Figure4.11b,c respectively, confirmed the involvement of a different mechanism of uptake for cHANPs and ANG-cHANPs.

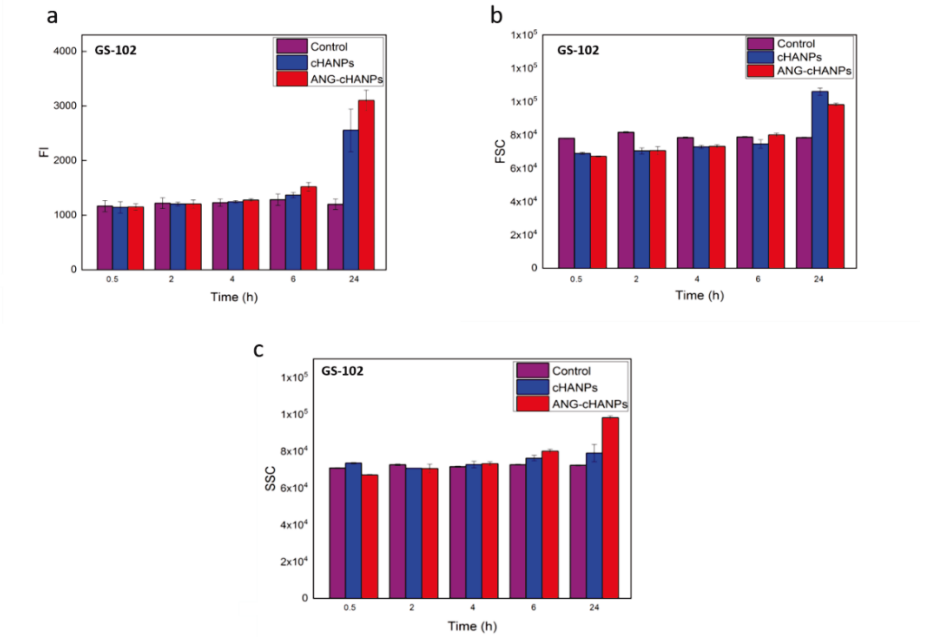

Figure 4.11 – Flow cytometry measurement for cHANPs and ANG-cHANPs uptake quantification by GS-102 cells. a) Fluorescence intensity (FI) of U87 cells after incubation with cHANPs and ANG-cHANPs; b) Forward scattering (FSC) of GS-102 after incubation with cHANP and ANG-cHANPs; c) Side scattering (SSC) of GS-102 cells after incubation with cHANPs and ANG-cHANPs;

IV.III.VI. ANG-cHANPs cellular localization by Confocal imaging

ANG-cHANPs localization in U87-MG cells is studied by confocal imaging. This study is performed with ANG-cHANPs encapsulating Gd-DTPA and ATTO 633 (EE% 10%), a NIR dye, in place of ATTO 488 in order to avoid artifacts due to the strong autofluorescence of biological samples in the visible spectrum[53]. Figures 4.12 a,b confirm ANG-cHANPs uptake, showing nanoparticle accumulation into cells. The image confirm the stability of ATTO 633 loading inside nanoparticles considering the absence of diffuse fluorescence associated with free dye[54]. As previously observed by flow cytometry results reported in Figures 4.9a–c, Figure 4.12 confirm a relevant uptake of ANG-cHANPs after 6h with a strong correlation of ANG-cHANPs with lysosomes (the overlap of red and green fluorescence of ANG-cHANPs and lysosomes respectively). These results perfectly match the flow cytometry results.

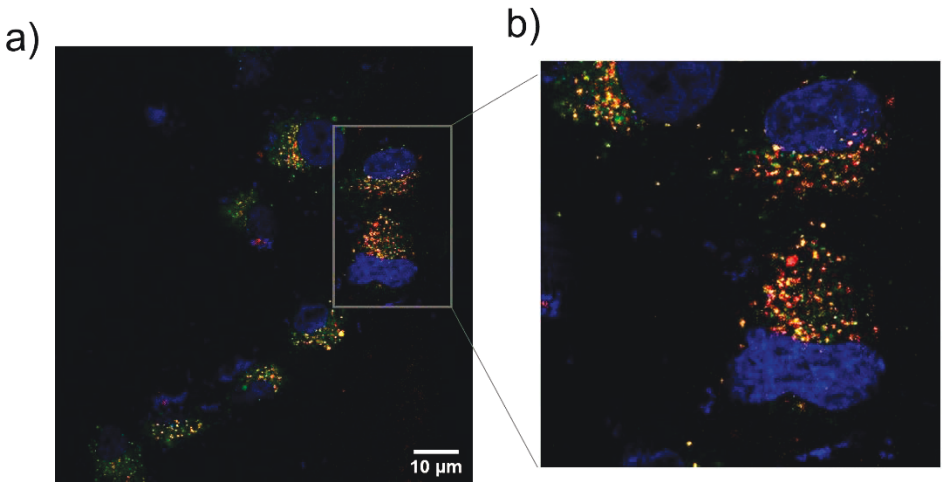

Figure 4.12 – Cellular localization of ANG-cHANPs in U87 cells by confocal imaging. Cell nuclei blu, Hoechest; Lysosomes green, Lysotracker green; ANG-cHANPs red, ATTO633.

IV.III.VII. Thera-cHANPs and Thera-ANG-cHANPs Uptake in U87 Cells

Flow cytometry measurements are performed on U87 MG cells incubated with free CPT-11, Thera-cHANPs and Thera-ANG-cHANPs at the same concentration of CPT-11 of 10 µM at different time points. The FSC measurement was used as an indication of cell viability, with the aim to assess the therapeutic potential of the nanoformulations and compare it to the free drug. As CPT-11 is a topoisomerase inhibitor acting on cell division, three time points up to 48 h were analysed to allow all the cells to complete the cell cycle. Similar to the previous experiment, the measurements of SSC were used to evaluate the amount of internalized nanoparticles, being an indication of the granularity of the cells. In this way, both the role of the nanovector itself and

Angiopep-2 in improving the uptake of CPT-11 can be evaluated. Figure 4.13a shows that starting from 24 h, the FSC both for Thera-cHANPs and Thera-ANG-cHANPs is decreased with respect to the control. In particular, the FSC of Thera-ANG-cHANPs is significantly decreased of about 35% at 24 h. The increase in FSC at 48 h may be attributed to remaining live cells that continue to replicate, with internalized NPs dividing in daughter cells causing a decrease in the amount of CPT-11 per cell. This hypothesis is supported by the significantly decreased SSC value. FSC values of free CPT-11 are higher than nanoparticles up to 48 h showing that free CPT-11 has a delayed effect with respect to nanoformulated CPT-11, which confirms improved uptake capacity of Thera-ANG-cHANPs. SSC values in Figure 4.13b confirm these results, which are significantly higher for Thera-cHANPs and Thera-ANG-cHANPs up to 24 h. Also in this case, free CPT-11 reaches the highest internalization only at 48 h. Both FSC and SSC confirm the improved uptake of nanoformulated CPT-11 which is significantly faster with respect to free drug. This effect is particularly evident for Thera-ANG-cHANPs.

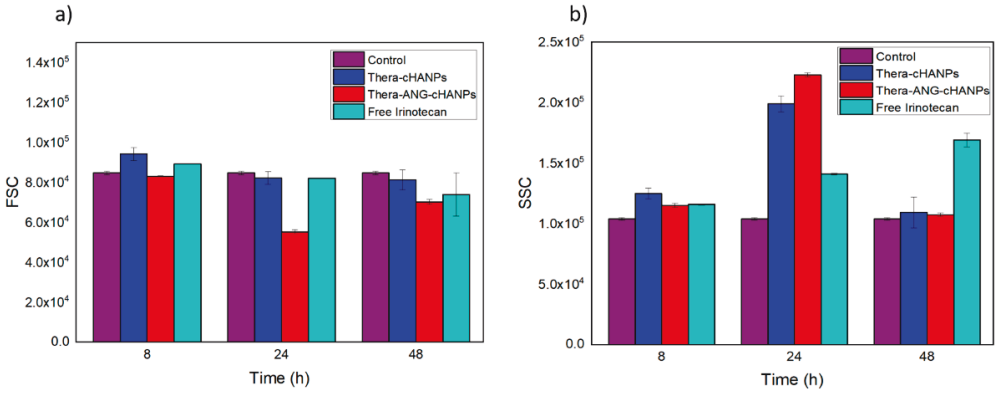

Figure 4.13 - Quantitative uptake of NPs by U87-MG cells by flow cytometry. a) Forward scattering (FSC) of U87 after incubation with theranostic Thera-cHANPs and Thera-ANG-cHANPs; b) Side scattering (SSC) of U87 after incubation with Thera-cHANPs and Thera ANG-cHANPs.

To further confirm the therapeutic potential of the formulations, an MTT assay is performed on U87 cells after incubation with 10 µM of free irinotecan, irinotecan in Thera-cHANPs, and in Thera-ANG-cHANPs at 24 h and 48 h. Results presented in Figure 4.14, confirm the improved therapeutic effect of Thera-ANG-cHANPs over the other treatments at the same concentration of drug. Importantly, the effect of Thera-ANG-cHANPs is already evident at 24 h, where the cell viability is reduced to 62%, while free irinotecan causes a reduction only at 92%. These results match flow cytometry measurements.

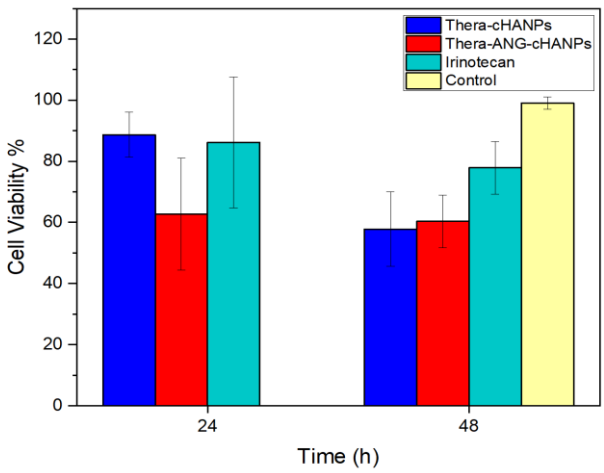

4.14 – U87 cell viability after incubation with free CPT-11, Thera-cHANPs, Thera-ANG-cHANPs (10 µM CPT-11) by MTT assay.

IV.III.VIII. Effect of Angiopep-2 surface density on cellular uptake by U87

Once demonstrated the improved transport of ANG-cHANPs and Thera-ANG-cHANPs in different cellular models of glioma and the consequent improved therapeutic effect of the formulation in U87 cells, the effect of different ANG-cHANPs surface density on particle cellular internalization was assessed. To reach a higher control over the conjugation reaction and control the superficial density of the peptide, Angiopep-2 was conjugated to the backbone of HA before microfluidic processing to obtain HA-TY19. As a first step, a titration curve was built to quantify the molar concentration of available carboxyl groups of HA, found equal to 155 nmol/mL. Then, varying amounts of Angiopep-2 at molar ratios $-COOH_{HA}$ /$-NH_{2\ ANG\text{-}2}$ equal to 2:1, 1:1 and 1:3 were conjugated through the previously reported procedure. Briefly, EDC and NHS were added to the solution and wheel stirred for 10 min to activate HA carboxyl groups. Then, varying amounts of Angiopep-2 were added and let react for 4h. At reaction completion, dialysis with a 50kDa cellulose membrane was used to purify the samples from unreacted peptide. The amount of successfully bound peptide was measured by BCA assay. Results in Table 4 show, as expected, that higher amount of added peptide corresponded to higher amount of bound peptide.

As a second step, HA-TY19 polymer was used to produce TY-19-cHANPs via nanoprecipitation in the microfluidic platform. As from standard operative conditions, the solvent solution of HA-TY19 (0.05%w/V), Gd-DTPA (0.1% w/V), ATTO633 (10 nmol/mL) was injected in the middle channel at 27 µL/min. The non-solvent solution of Acetone and DVS (4% V/V) was injected in the side channels at 110 µL/min. After purification, particles were characterized for amount of superficial

peptide, morphology and relaxometric properties. BCA assay is used to quantify the amount of peptide exposed on the particle surface and results demonstrate increasing amounts of peptide from 2:1 to 1:3 molar ratios. Surprisingly, for the HA-TY19 2:1 the whole amount of bound peptide seems to be superficially exposed. However, despite the correction of the measured absorbance values of the particles for the absorbance of the HA—TY19 polymer, a possible interference of the crosslinked polymer network in the measurement should be considered. Moreover, the porous nature of the hydrogel composing the particles might allow the entrance of BCA reagents inside the network and react also with internally exposed Angiopep-2 molecules, in this way interfering with superficial peptide measurement.

As expected, higher amount of superficial peptide was found for cHANPs-TY19 1:1 and cHANPs-TY19 1:3. SEM and TEM images in Figure 4.15 a-d compare results for cHANPs with results for cHANPs-TY19 at increasing -$COOH_{HA}$ /-$NH_{2\ ANG-2}$ molar ratios. The images demonstrate that for cHANPs-TY19 2:1 the morphological stability as well as particle size is preserved with respect to cHANPs. For cHANPs-TY19 1:1 and 1:3 morphological stability was not achieved with a matrix surrounding particles that appear bigger and aggregated. These results suggest that the higher amount of bound Angiopep-2 might have interfered both with the nanoprecipitation and the crosslinking of the nanoparticles leading to a poorly controlled production process. The measurement of relaxometric properties allowed to further confirm this hypothesis. As reported in Figure 4.15e, cHANPs-TY19 2:1 showed equal T1 of standard cHANPs, indication of both good EE% and efficient crosslinking reaction. This result was not achieved for cHANPs-TY19 1:1 and 1:3 showing a certain amount of encapsulated Gd-DTPA, being T1 higher than the typical value of pure water, but a strongly higher T1.

Table 4. Quantification of successfully bound Angiopep-2 and its surface density post particle production

SAMPLE (-COOH:NH_2)	Angiopep-2 [ug/mL]	Superficial Angiopep-2 post particle production [ug/mL]
HA-TY19 2:1, 4h	13.82	14,96
HA-TY19 1:1, 4h	55.30	26,76
HA-TY19 1:3, 4h	76.89	27,72

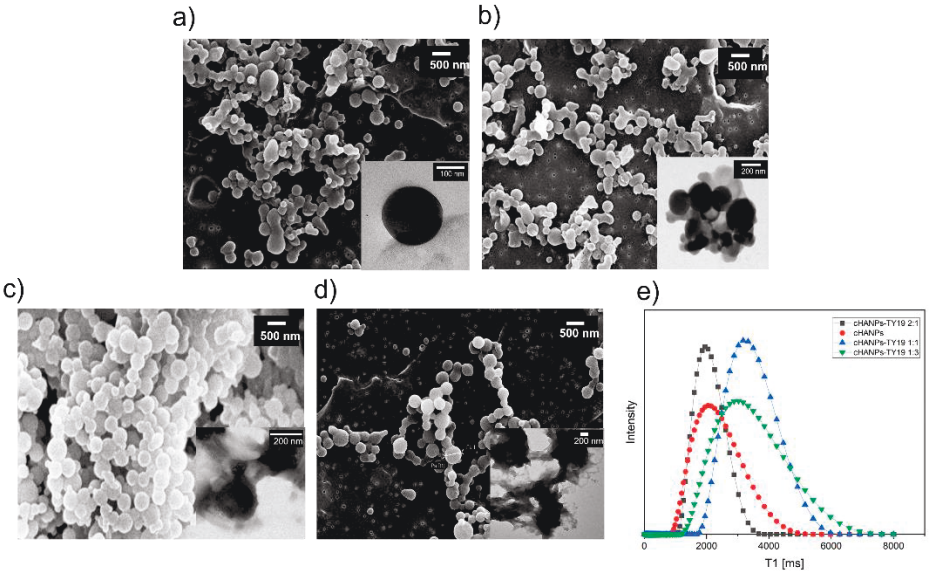

Figure 4.15 – cHANPs-TY19 physical chemical characterization. a) SEM and TEM images of cHANPs; b) SEM and TEM images of cHANPs-TY19 2:1; b) SEM and TEM images of cHANPs-TY19 1:1 b) SEM and TEM images of cHANPs-TY19 1:3 e) Relaxometric properties of cHANPs, cHANPs-TY19 2:1, cHANPs-TY19 1:1 and cHANPs-TY19 1:3 by Minispec Benchtop Relaxometer

After production and characterization, cHANPs-TY19 2:1, 1:1 and 1:3 were incubated with U87 cells for 1h, 2h, 4h and 8h to investigate the impact of different Angiopep-2 surface density on particle uptake. Measurements were performed by flow cytometry and results are presented in Figure 4.16. Quantification of fluorescent intensity (FI) revealed that a significant increase in fluorescence over time could be detected both for cHANPs and cHANPs-TY19 2:1. Additionally, cHANPs-TY19 2:1 revealed a higher uptake than bare cHANPs at any time point, that increases linearly with time, suggesting a potential involvement of Angiopep-2 and of an active mechanism in particle uptake. Differently no trend in both cHANPs-TY19 1:1 and 1:3 could be detected, suggesting that the higher fluorescent intensity measured in different time points could be attributed to the free dye that was released from particles as a consequence of their poor stability, potentially worsened in the biological environment.

By comparing results obtained for cHANPs-TY19 2:1 with results previously showed for ANG-cHANPs in Figure 4.9, a modulation in the amount of internalized particles up to 8h could be detected. As a result, we can conclude that the modulation of Angiopep-2 surface density allowed to successfully modulate the particle internalization by U87.

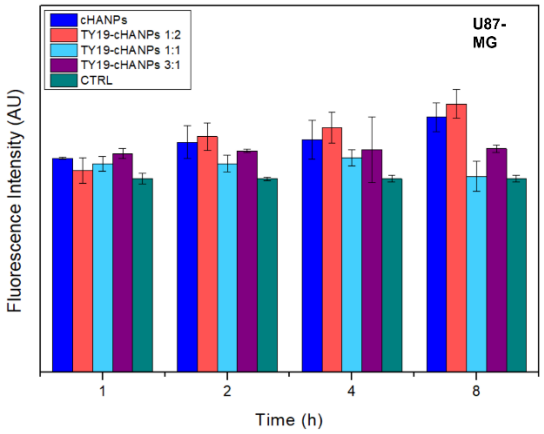

Figure 4.16 – Quantification of the uptake of cHANPs, cHANPs-TY19 2:1, cHANPs-TY19 1:1 and cHANPs-TY19 1:3 by flow cytometry

IV.III.IX. *Glutathione engineering of cHANPs (GLUT-cHANPs) as alternative strategy to study target cell-particle interaction*

Despite being the most promising both for specificity and dual targeting capability, Angiopep-2 and LRP-1 do not constitute the only ligand-receptor system successfully explored in formulations actively targeting the BBB. Glutathione (GSH), a 307 Da tripeptide, has been reported to enhance the transport of active molecules in the CNS crossing both healthy and tumour-disrupted BBB, whose success has been widely demonstrated both in preclinical and clinical settings[55-58]. Although the molecular mechanism(s) as well as the involvement of specific receptors for the improved BBB transport are still unclear, in 2016 Maussang et al., demonstrated that the transport of GSH-liposomes relies on a temperature-, time-, and dose-dependent uptake revealing the involvement of an active targeting mechanism at the BBB *in-vivo*[59]. These observations confirmed the potential of GSH as a shuttle for improved CNS transport of active agents across the BBB. Despite this achievement, no information about the possible role of GSH in improving nanoparticle interaction with the tumour cells is available. To the purpose, the conjugation of GSH on the surface of cHANPs (GLUT-cHANPs) was performed, the nanoparticle morphological stability at conjugation was assessed and the uptake of GLUT-cHANPs by U87 was quantified by flow cytometry and compared to ANG-cHANPs uptake. Co-loaded GLUT-cHANPs are produced by the previously reported procedure. Briefly, post particle production, carboxyl groups of cHANPs are activated by EDC and NHS (10 min of wheel stirring). Then, 50 µg/mL of GSH are let react for 4h and purified by Spin-X Corning Centrifugation. Figure 4.17 a presents a TEM image of GLUT-cHANPs, confirming particle morphological stability and clearly revealing the presence of the bound peptide both on the particle surface and in the inner network as a possible consequence of the peptide diffusion in the polymer network. BCA

measurements confirmed this result with 25.6 µg/mL of peptide bound to cHANPs. After production, uptake by U87 cells is investigated and results were compared to ANG-cHANPs uptake, Figure 4.17b. As clearly revealed, a significantly increased fluorescence could be detected at any time point with respect to the negative control. However, after a significant increase in the first 2h a plateau is reached with 6h characterized by a sharp decreased fluorescence. This trend is instead not present for ANG-cHANPs showing a linear increase in fluorescence over time. Salvati et al.[51,54] reported that the reaching of a plateau in particle internalization in the first hours of contact is sign of fast lysosomal capture of the particles, typical of passive, endocytosis-based internalization mechanisms. For this reason, it can be preliminary concluded that, apparently, GLUT-cHANPs interaction with U87 cells does not occur through a specific, energy dependent mechanism despite further studies depleting cellular ATP should be conducted to confirm this hypothesis.

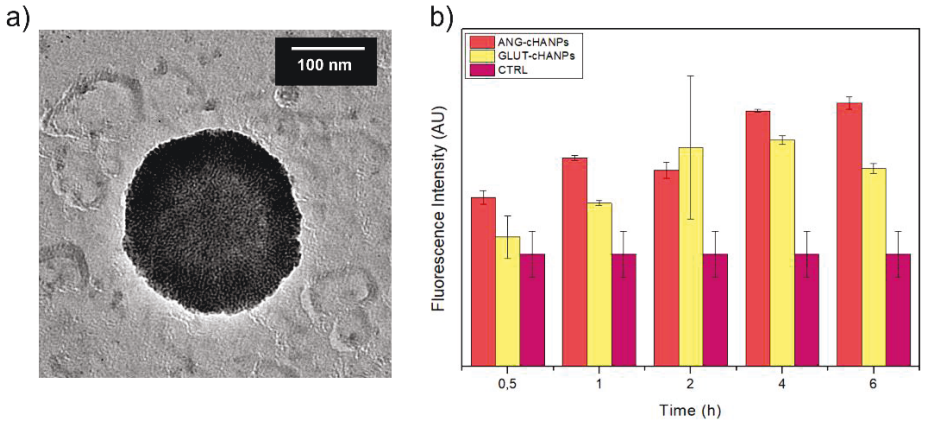

Figure 4.17 – GLUT-cHANPs interaction with U87 cells. a) GLUT-cHANPs morphological characterization by TEM; b) GLUT-cHANPs uptake by U87 and comparison with ANG-cHANPs.

IV.III.X. Preliminary in-vivo testing of cHANPs

The characterization of engineered cHANPs for overcoming the disease-specific biological barriers of Glioblastoma Multiforme with the peptide Angiopep-2 demonstrated the preservation of the synthetic identity of ANG-cHANPs at conjugation. Additionally, the evaluation of ANG-cHANPs biological identity in-vitro demonstrated the specific role of the peptide in improving particle interaction with the biological target excluding a negative impact of protein corona formation on the targeting ability of the vector. In this section, the biodistribution of cHANPs is preliminary investigated as a starting point for the testing of ANG-cHANPs and the

evaluation of tumour accumulation of cHANPs in glioma bearing mice to assess both the feasibility of different routes of administration, and potentiality in particle tumour accumulation. Co-loaded cHANPs were injected via tail vein in three healthy BALB/c mice at a Gd-DTPA concentration of 60 µM. Animals were sacrificed 4h and 8h after injection to study the particle biodistribution by ex-vivo IVIS fluorescence of excised organs. Results in Figure 4.18 show nanoparticle accumulation after 4h and 8h in major organs compared with organ signal of animals injected with free Gd-DTPA as negative control for fluorescence. In details, after 4h a minor accumulation of nanoparticles can be observed in the liver, confirming the stealth properties of HA guaranteeing a long circulation time. No accumulation in other organs is visible. With respect to 8h fluorescence, liver accumulation increases and a partial accumulation in lungs can be observed. As for the previous time point, no accumulation in other organ is visible. As a conclusion, it is possible to confirm the role of drug delivery system in controlling the biodistribution of active agents and the reduction of off-target toxicity. With particular regard to hyaluronic acid, its stealth properties allow to achieve long circulation times.

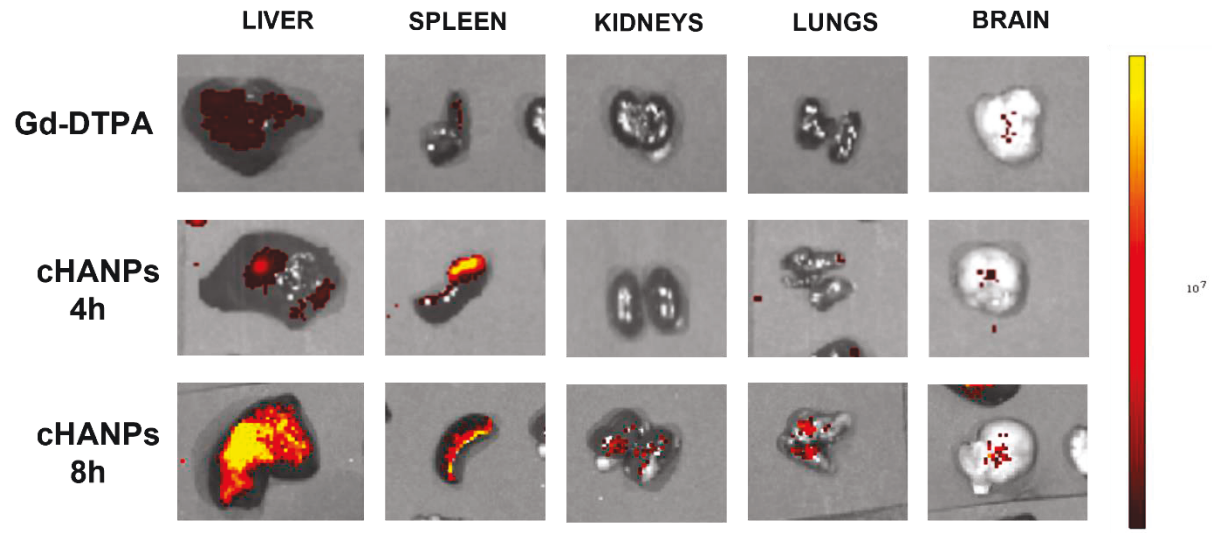

Figure 4.18 – Preliminary in-vivo biodistribution of co-loaded cHANPs in healthy mice. Animals injected with free Gd-DTPA were used as control.

As a second step, cHANPs were tested in glioma bearing mice. Briefly, an orthotopic model of human glioma (U87) was implanted in BALB/c nude mice and an intracranial chamber was surgically implanted to allow on-line, high-resolution optical light access to the tumour. For testing, cHANPs were administered both systemically or retro-orbitally. For systemic administration, cHANPs at a concentration of 100 nM of dye (ATTO488) were injected via tail vein. No significant accumulation inside the tumour could be detected. This can be attributed to the presence of the BBB that hinders the transport of molecules in the CNS and to the highly inefficient passive transport provided by the EPR effect. To test the suitability of a different route

of administration that allows to skip the BBB, retroorbital injection of cHANPs at a concentration of 230 nM of dye was performed. Preliminary observations at 4h from injection in Figure 4.19 reveal the presence of fluorescent spots inside the tumour, confirming that nanoparticle sufficiently accumulated inside the tumour.

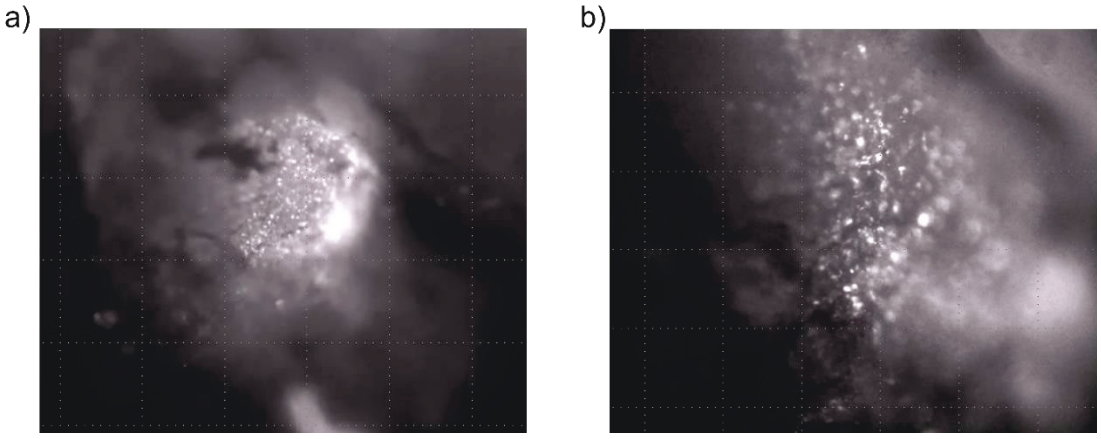

Figure 4.19 - Evaluation of cHANPs accumulation in a human glioma model. a) optical image of the tumour accessed from the intracranial window; b) zoomed optical image of the tumour from the intracranial window.

IV.IV. Conclusions

Nanoformulated hydrogels have shown the unique ability of boosting relaxometric properties of Gd-based contrast agents up to 12-fold through the property of Hydrodenticity[60-62]. Moreover, in the previous chapters we demonstrated that this effect is preserved even when multiple agents are encapsulated and in complex biological environments. This feature makes cHANPs an appealing platform to address the limitations characterizing Glioblastoma Multiforme, an incurable very aggressive malignant brain tumour. The limited ability of active agents in the gold-standard for treatment, diagnosis, and follow-up of GBM in effectively overcoming disease-specific biological barriers lead to scarce clinical success and poor patient prognosis.

In this framework, Thera-cHANPs co-encapsulating CPT-11 as an alternative treatment to the poorly effective Temozolomide and Gd-DTPA with improved relaxometric properties have been specifically engineered with the peptide Angiopep-2 (Thera-ANG-cHANPs), that demonstrated 10-fold improved transport at the BBB when compared to free drug administration in clinics, for improved cHANPs transport at the healthy BBB. First, Angiopep-2 interaction with LRP-1 receptors was assessed via molecular docking to understand whether a chemical conjugation might prejudicate the targeting ability of the peptide. Secondly, ANG-cHANPs biological identity was

evaluated in-vitro excluding a negative impact of protein corona formation on the targeting ability of the vector. Indeed, ANG-cHANPs interaction with multiple in-vitro models of glioma moving from standard U87 cells to the patient derived GS-102 cells was assessed and an Angiopep-2 triggered active targeting mechanism responsible for the boosted uptake of ANG-cHANPs in both targets was demonstrated. Furthermore, the impact of different surface ligand density on the regulation of particle uptake was assessed. As a consequence of the improved cell/particle interaction, an increased therapeutic effect of Thera-ANG-cHANPs both with respect to bare Thera-cHANPs and free-drug was demonstrated. As a comparison, cHANPs were engineered with the peptide Glutathione (GSH) which demonstrated improved transport at the BBB in several phase I/II clinical trials[55-59]. Despite the expected advantage in improved BBB transport, a preliminary study in the evaluation of GLUT-cHANPs uptake in U87 cells demonstrated an apparent passive, endocytosis-based uptake mechanism that was not introducing significant improvements with respect to bare cHANPs.

Finally, preliminary in-vivo studies were conducted both in healthy mice and in mice bearing an orthotopic model of glioma to investigate cHANPs biodistribution, and the feasibility of two different routes of administration, systemic and intraocular. Preliminary results allowed to assess an expected circulation time of 8h and exclude off-target accumulations of bare cHANPs. Additionally, retro-orbitally injected cHANPs showed a significant tumour accumulation. As a perspective, ANG-cHANPs biodistribution has to be investigated as well as the ability of BBB crossing and selective tumour accumulation.

IV.V. References

1 Skalli, O. *et al.* Astrocytoma grade IV (gLioblastoma multiforme) displays 3 subtypes with unique expression profiles of intermediate filament proteins. *Human Pathology* **44**, 2081-2088, doi:10.1016/j.humpath.2013.03.013 (2013).

2 Weller, M., van den Bent, M. & Tonn, J. C. European Association for Neuro-Oncology (EANO) guideline on the diagnosis and treatment of adult astrocytic and oligodendroglial gliomas (vol 18, e315, 2017). *Lancet Oncology* **18**, E642-E642 (2017).

3 van den Bent, M., MacDonald, D., Chang, S., Vogelbaum, M. A. & Wen, P. Y. UPDATED RESPONSE ASSESSMENT CRITERIA FOR HIGH-GRADE GLIOMAS (HGG): REPORT FROM THE RESPONSE ASSESSMENT IN NEURO-ONCOLOGY (RANO) WORKING GROUP. *Neuro-Oncology* **12**, 3-3 (2010).

4 Lee, S. Y. Temozolomide resistance in glioblastoma multiforme. *Genes & Diseases* **3**, 198-210, doi:10.1016/j.gendis.2016.04.007 (2016).

5 Castro, B. A. & Aghi, M. K. Bevacizumab for glioblastoma: current indications, surgical implications, and future directions. *Neurosurgical Focus* **37**, doi:10.3171/2014.9.focus14516 (2014).

6 Sharif, Y. *et al.* Blood Brain Barrier: A Review of Its Anatomy and Physiology in Health and Disease. *Clinical Anatomy* **31**, 812-823, doi:10.1002/ca.23083 (2018).

7 Kim, J., Ahn, S. I. & Kim, Y. Nanotherapeutics engineered to cross the blood-brain barrier for advanced drug delivery to the central nervous system. *Journal of Industrial and Engineering Chemistry* **73**, 8-18, doi:10.1016/j.jiec.2019.01.021 (2019).
8 Oberoi, R. K. *et al.* Strategies to improve delivery of anticancer drugs across the blood-brain barrier to treat glioblastoma. *Neuro-Oncology* **18**, 27-36, doi:10.1093/neuonc/nov164 (2016).
9 Laquintana, V. *et al.* New strategies to deliver anticancer drugs to brain tumors. *Expert Opinion on Drug Delivery* **6**, 1017-1032, doi:10.1517/17425240903167942 (2009).
10 Barar, J., Rafi, M. A., Pourseif, M. M. & Omidi, Y. Blood-brain barrier transport machineries and targeted therapy of brain diseases. *Bioimpacts* **6**, 225-248, doi:10.15171/bi.2016.30 (2016).
11 Wang, H. & Eckel, R. H. What are lipoproteins doing in the brian? *Trends in Endocrinology and Metabolism* **25**, 8-14, doi:10.1016/j.tem.2013.10.003 (2014).
12 Zhao, Y. H., Li, D. D., Zhao, J. J., Song, J. N. & Zhao, Y. L. The role of the low-density lipoprotein receptor-related protein 1 (LRP-1) in regulating blood-brain barrier integrity. *Reviews in the Neurosciences* **27**, 623-634, doi:10.1515/revneuro-2015-0069 (2016).
13 Jain, R. K. & Stylianopoulos, T. Delivering nanomedicine to solid tumors. *Nature Reviews Clinical Oncology* **7**, 653-664, doi:10.1038/nrclinonc.2010.139 (2010).
14 Boucher, Y., Salehi, H., Witwer, B., Harsh, G. R. & Jain, R. K. Interstitial fluid pressure in intracranial tumours in patients and in rodents. *British Journal of Cancer* **75**, 829-836, doi:10.1038/bjc.1997.148 (1997).
15 Jain, K. K. Nanobiotechnology-based strategies for crossing the blood-brain barrier. *Nanomedicine* **7**, 1225-1233, doi:10.2217/nnm.12.86 (2012).
16 Quail, D. F. & Joyce, J. A. The Microenvironmental Landscape of Brain Tumors. *Cancer Cell* **31**, 326-341, doi:10.1016/j.ccell.2017.02.009 (2017).
17 Ulrich, T. A., Pardo, E. M. D. & Kumar, S. The Mechanical Rigidity of the Extracellular Matrix Regulates the Structure, Motility, and Proliferation of Glioma Cells. *Cancer Research* **69**, 4167-4174, doi:10.1158/0008-5472.can-08-4859 (2009).
18 Seano, G. *et al.* Solid stress in brain tumours causes neuronal loss and neurological dysfunction and can be reversed by lithium. *Nature Biomedical Engineering* **3**, 230-+, doi:10.1038/s41551-018-0334-7 (2019).
19 Schiffer, D., Annovazzi, L., Casalone, C., Corona, C. & Mellai, M. Glioblastoma: Microenvironment and Niche Concept. *Cancers* **11**, doi:10.3390/cancers11010005 (2019).
20 Demeule, M. *et al.* Drug transport to the brain: Key roles for the efflux pump P-glycoprotein in the blood-brain barrier. *Vascular Pharmacology* **38**, 339-348, doi:10.1016/s1537-1891(02)00201-x (2002).
21 Seano, G. Targeting the perivascular niche in brain tumors. *Current Opinion in Oncology* **30**, 54-60, doi:10.1097/cco.0000000000000417 (2018).
22 Yang, D. W. Standardized MRI assessment of high-grade glioma response: a review of the essential elements and pitfalls of the RANO criteria. *Neuro-Oncology Practice* **3**, 59-67, doi:10.1093/nop/npv023 (2016).
23 Man, F., Lammers, T. & de Rosales, R. T. M. Imaging Nanomedicine-Based Drug Delivery: a Review of Clinical Studies. *Molecular Imaging and Biology* **20**, 683-695, doi:10.1007/s11307-018-1255-2 (2018).
24 Danhier, F. To exploit the tumor microenvironment: Since the EPR effect fails in the clinic, what is the future of nanomedicine? *Journal of Controlled Release* **244**, 108-121, doi:10.1016/j.jconrel.2016.11.015 (2016).
25 Stylianopoulos, T. & Jain, R. K. Design considerations for nanotherapeutics in oncology. *Nanomedicine-Nanotechnology Biology and Medicine* **11**, 1893-1907, doi:10.1016/j.nano.2015.07.015 (2015).

26 Sarkaria, J. N. *et al.* Is the blood-brain barrier really disrupted in all glioblastomas? A critical assessment of existing clinical data. *Neuro-Oncology* **20**, 184-191, doi:10.1093/neuonc/nox175 (2018).
27 Sonali. Vol. 2 (eds Rahul Pratap Singh Matte Kasi Viswanadh , Poornima Agrawal , Abhishesh Kumar Mehata , Datta Maroti Pawde , & and Madaswamy Sona Muthu Roshan Sonkar) 70-86 (Nanotheranostics, 2018).
28 Taghizadehghalehjoughi, A. *et al.* Effect of metformin/irinotecan-loaded poly-lactic-co-glycolic acid nanoparticles on glioblastoma: in vitro and in vivo studies. *Nanomedicine* **13**, 1595-1606, doi:10.2217/nnm-2017-0386 (2018).
29 Lam, F. C. *et al.* Enhanced efficacy of combined temozolomide and bromodomain inhibitor therapy for gliomas using targeted nanoparticles. *Nature Communications* **9**, doi:10.1038/s41467-018-04315-4 (2018).
30 www.proteinatlas.org.
31 Bu, G. J., Maksymovitch, E. A., Geuze, H. & Schwartz, A. L. SUBCELLULAR-LOCALIZATION AND ENDOCYTIC FUNCTION OF LOW-DENSITY-LIPOPROTEIN RECEPTOR-RELATED PROTEIN IN HUMAN GLIOBLASTOMA CELLS. *Journal of Biological Chemistry* **269**, 29874-29882 (1994).
32 Maletinska, L. *et al.* Human glioblastoma cell lines: Levels of low-density lipoprotein receptor and low-density lipoprotein receptor-related protein. *Cancer Research* **60**, 2300-2303 (2000).
33 Jensen, G. A. *et al.* Binding Site Structure of One LRP-RAP Complex Implications for a Common Ligand-Receptor Binding Motif. *Biological Magnetic Resonance Data Bank*, doi:10.13018/bmr17055 (2010).
34 Liu, B. *et al.* In-silico analysis of ligand-receptor binding patterns of α-MMC, TCS and MAP30 protein to LRP1 receptor. *Journal of Molecular Graphics and Modelling* **98**, 107619, doi:https://doi.org/10.1016/j.jmgm.2020.107619 (2020).
35 Demeule, M. *et al.* Identification and design of peptides as a new drug delivery system for the brain. *Journal of Pharmacology and Experimental Therapeutics* **324**, 1064-1072, doi:10.1124/jpet.107.131318 (2008).
36 Bertrand, Y. *et al.* Transport characteristics of a novel peptide platform for CNS therapeutics. *Journal of Cellular and Molecular Medicine* **14**, 2827-2839, doi:10.1111/j.1582-4934.2009.00930.x (2010).
37 Regina, A. *et al.* Antitumour activity of ANG1005, a conjugate between paclitaxel and the new brain delivery vector Angiopep-2. *British Journal of Pharmacology* **155**, 185-197, doi:10.1038/bjp.2008.260 (2008).
38 Lamiable, A. *et al.* PEP-FOLD3: faster denovo structure prediction for linear peptides in solution and in complex. *Nucleic Acids Research* **44**, W449-W454, doi:10.1093/nar/gkw329 (2016).
39 Lee, D. *et al.* The structure of receptor-associated protein (RAP). *Protein Science* **16**, 1628-1640, doi:10.1110/ps.072865407 (2007).
40 Guttman, M., Prieto, J. H., Handel, T. M., Domaille, P. J. & Komives, E. A. Structure of the Minimal Interface Between ApoE and LRP. *Journal of Molecular Biology* **398**, 306-319, doi:10.1016/j.jmb.2010.03.022 (2010).
41 Pitas Re Fau - Innerarity, T. L., Innerarity Tl Fau - Mahley, R. W. & Mahley, R. W. Cell surface receptor binding of phospholipid . protein complexes containing different ratios of receptor-active and -inactive E apoprotein.
42 Simonovic, M. *et al.* Calcium coordination and pH dependence of the calcium affinity of ligand-binding repeat CR7 from the LRP. Comparison with related domains from the LRP and the LDL receptor.
43 Li, Y., Zheng, X. M., Gong, M. & Zhang, J. N. Delivery of a peptide-drug conjugate targeting the blood brain barrier improved the efficacy of paclitaxel against glioma. *Oncotarget* **7**, 79387-79393, doi:10.18632/oncotarget.12708 (2016).

44 Xin, H. L. *et al.* The brain targeting mechanism of Angiopep-conjugated poly(ethylene glycol)-co-poly(epsilon-caprolactone) nanoparticles. *Biomaterials* **33**, 1673-1681, doi:10.1016/j.biomaterials.2011.11.018 (2012).
45 Li, J. Y. & Mooney, D. J. Designing hydrogels for controlled drug delivery. *Nature Reviews Materials* **1**, doi:10.1038/natrevmats.2016.71 (2016).
46 Pont, L. *et al.* In vitro screening of clinical drugs identifies sensitizers of oncolytic viral therapy in glioblastoma stem-like cells. *Gene Therapy* **22**, 947-959, doi:10.1038/gt.2015.72 (2015).
47 Pont, L. *et al.* The HDAC Inhibitors Scriptaid and LBH589 Combined with the Oncolytic Virus Delta24-RGD Exert Enhanced Anti-Tumor Efficacy in Patient-Derived Glioblastoma Cells. *Plos One* **10**, doi:10.1371/journal.pone.0127058 (2015).
48 Balvers, R. K. *et al.* Serum-free culture success of glial tumors is related to specific molecular profiles and expression of extracellular matrixassociated gene modules. *Neuro-Oncology* **15**, 1684-1695, doi:10.1093/neuonc/not116 (2013).
49 Yu, Q. H., Zhao, L. X., Guo, C. C., Yan, B. & Su, G. X. Regulating Protein Corona Formation and Dynamic Protein Exchange by Controlling Nanoparticle Hydrophobicity. *Frontiers in Bioengineering and Biotechnology* **8**, doi:10.3389/fbioe.2020.00210 (2020).
50 Manzanares, D. & Cena, V. Endocytosis: The Nanoparticle and Submicron Nanocompounds Gateway into the Cell. *Pharmaceutics* **12**, doi:10.3390/pharmaceutics12040371 (2020).
51 Salvati, A. *et al.* Quantitative measurement of nanoparticle uptake by flow cytometry illustrated by an interlaboratory comparison of the uptake of labelled polystyrene nanoparticles. *Nanoimpact* **9**, 42-50, doi:10.1016/j.impact.2017.10.004 (2018).
52 Jochums, A. *et al.* Revelation of Different Nanoparticle-Uptake Behavior in Two Standard Cell Lines NIH/3T3 and A549 by Flow Cytometry and Time-Lapse Imaging. *Toxics* **5**, doi:10.3390/toxics5030015 (2017).
53 Monica, M. Cell and tissue autofluorescence research and diagnostic applications. *Biotechnology Annual Review* **11**, 227 - 256, doi:10.1016/S1387-2656(05)11007-2 (2005).
54 Salvati, A. *et al.* Experimental and theoretical comparison of intracellular import of polymeric nanoparticles and small molecules: toward models of uptake kinetics. *Nanomedicine-Nanotechnology Biology and Medicine* **7**, 818-826, doi:10.1016/j.nano.2011.03.005 (2011).
55 Hu, Y., Gaillard, P. J., de Lange, E. C. M. & Hammarlund-Udenaes, M. Targeted brain delivery of methotrexate by glutathione PEGylated liposomes: How can the formulation make a difference? *European Journal of Pharmaceutics and Biopharmaceutics* **139**, 197-204, doi:10.1016/j.ejpb.2019.04.004 (2019).
56 Rotman, M. *et al.* Enhanced glutathione PEGylated liposomal brain delivery of an anti-amyloid single domain antibody fragment in a mouse model for Alzheimer's disease. *Journal of Controlled Release* **203**, 40-50, doi:10.1016/j.jconrel.2015.02.012 (2015).
57 Gaillard, P. J. *et al.* Pharmacokinetics, Brain Delivery, and Efficacy in Brain Tumor-Bearing Mice of Glutathione Pegylated Liposomal Doxorubicin (2B3-101). *Plos One* **9**, doi:10.1371/journal.pone.0082331 (2014).
58 Kerklaan, B. M. *et al.* PHASE 1/2A STUDY OF GLUTATHIONE PEGYLATED LIPOSOMAL DOXORUBICIN (2B3-101) IN BREAST CANCER PATIENTS WITH BRAIN METASTASES (BCBM) OR RECURRENT HIGH GRADE GLIOMAS (HGG). *Neuro-Oncology* **16**, doi:10.1093/neuonc/nou265.21 (2014).
59 Maussang, D. *et al.* Glutathione conjugation dose-dependently increases brain-specific liposomal drug delivery in vitro and in vivo. *Drug Discovery Today: Technologies* **20**, 59-69, doi:https://doi.org/10.1016/j.ddtec.2016.09.003 (2016).
60 De Sarno, F. *et al.* Water-Mediated Nanostructures for Enhanced MRI: Impact of Water Dynamics on Relaxometric Properties of Gd-DTPA. *Theranostics* **9**, 1809-1824, doi:10.7150/thno.27313 (2019).
61 Russo, M., Ponsiglione, A. M., Forte, E., Netti, P. A. & Torino, E. Hydrodenticity to enhance relaxivity of gadolinium-DTPA within crosslinked hyaluronic acid nanoparticles. *Nanomedicine* **12**, 2199-2210, doi:10.2217/nnm-2017-0098 (2017).

62 Russo, M., Bevilacqua, P., Netti, P. A. & Torino, E. A Microfluidic Platform to design crosslinked Hyaluronic Acid Nanoparticles (cHANPs) for enhanced MRI. *Scientific Reports* **6**, doi:10.1038/srep37906 (2016).

V. Chapter 5 – Clinically-validated pharmacokinetic modelling for the preliminary understanding of nano-bio-interactions

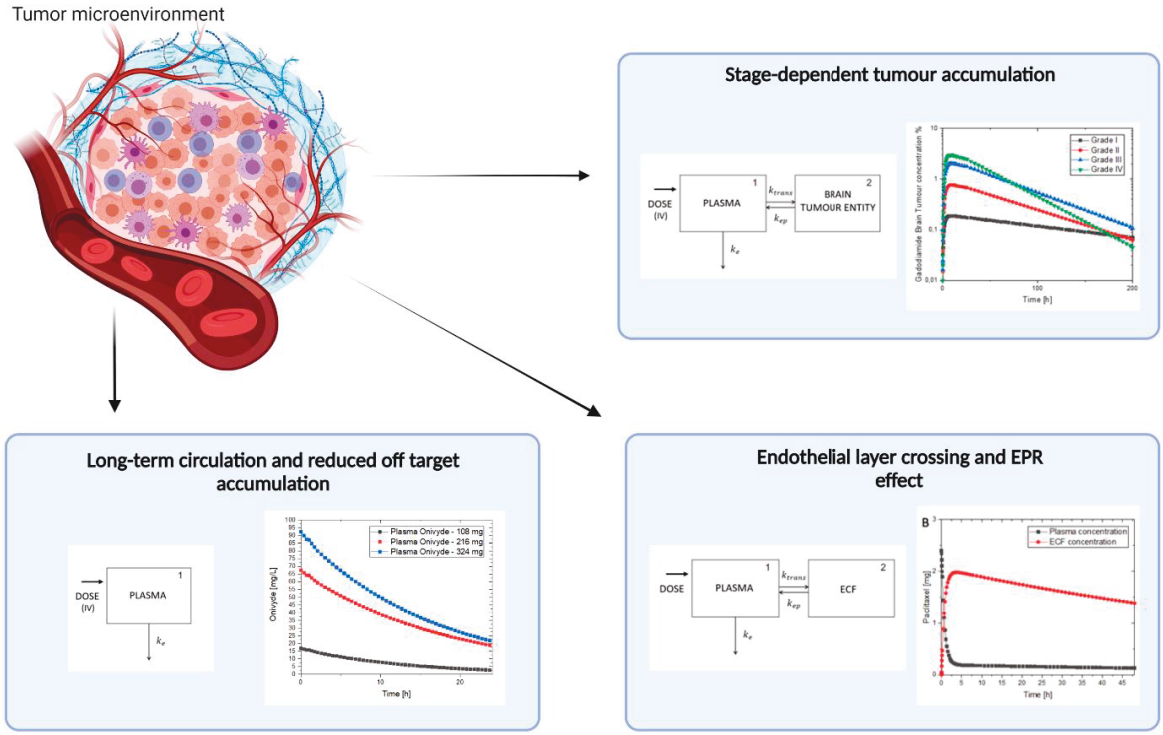

Graphical abstract Chapter 5 – Exploration of the potential of PK modelling for the investigation of nanobiointeractions in solid tumours

V.I. Background

The development of new drugs and formulations heavily relies on animal studies to provide a preliminary framework for the design of human clinical trials. Often time, a drug that works well in animals may be largely ineffective in humans since there is an inappropriate translation of a drug dose and treatment regimen from animal to humans[1]. Another lack is the fact that therapeutic efficacy studies often precede the pharmacokinetic profiling studies and thus doses are chosen from toxicity considerations without knowing drug or active metabolite concentrations in solid tumours. This absence of information on drug accumulation and distribution in tumours limits the understanding not only of drug transport but also of pertinent pharmacokinetic-pharmacodynamic relationships that could aid the drug development process. In consequence to the lack of these detailed pharmacokinetic-pharmacodynamic studies that measure drug disposition and dynamics in tumours, limitations in providing a quantitative framework to translate preclinical pharmacologic data to patients, arise[2]. This deficiency in part is attributed to the absence of a pharmacokinetic

modelling strategy that links preclinical and clinical data. For example, currently available models rely on classical pharmacokinetics, in which the complex multi-organ system which is relevant for drug distribution, accumulation and metabolism are simplified in one- or few-compartment models built on preclinically derived parameters which cannot account for anatomical and pathophysiology of human tumours[3]. Secondly, it depends on limited availability of clinical data and patient- derived parameters whose measurements are difficult to perform. Finally, the lack of detailed understanding of the pathophysiology of many solid tumours, as well as inaccurate tumour classification determine a great inter-patient variability of the acquired data[4].

This poor characterization of the pharmacokinetic-pharmacodynamic relation consequent to the absence of the PK profiling in humans, becomes even more crucial for nanomedicines since, as widely discussed, their effectiveness is strongly influenced by their biodistribution but particularly on their transport properties at the tumour site[5]. Effectiveness of nanomedicine transport at the diseased site strongly depend on the anatomy of the tumour microenvironment (TME), which is inevitably different between human and animal models. It is influenced by the implanted preclinical model, its developmental stage at the time of treatment testing and site of implantation. As an example, Ferretti et al.[6] reported interstitial fluid pressure (IFP) values in tumours originated from the same cell line but implanted in different locations or in different animal species revealing significantly different results. Increased IFP values are responsible for the sharp drop in the pressure gradient between the plasma and the interstitial space and for this reason it contributes significantly to lowering or deleting the convective transvascular transport, thus directly impacting on the ability of nanoformulations of accumulating inside the tumour extracellular space.

To answer the need for a more robust understanding of the human TME for rational design of treatment schedules and dosages, Zhou et al.[3], built a hybrid PK model to describe temozolomide (TMZ) deposition in a human orthotopic model of glioma in rats. They used a forcing function based on human pharmacokinetic parameters (absorption and elimination constants to build the plasma concentration curve over time) and tumour associated data obtained by the orthotopically implanted human model of glioma to have physiologically relevant estimations of the exchange constants between healthy brain, tumour brain and cerebrospinal fluid (CSF). Through this model they demonstrated the importance of using a predicting model in clinical setting because their simulations proved that patient tumour characteristics, due to either different BBB permeability or distinct tumour blood volume, could alter the brain tumour distribution of TMZ which at date, is highly ineffective despite being the standard of care. Thus, they underlined both the necessity of a patient specific treatment and the impossibility of using CSF concentrations of TMZ as surrogate for brain tumour measurements, since changes in the brain tumour accumulation of temozolomide are not reflected in CSF.

Moreover, PK models can also be exploited for improved diagnosis and characterization of solid tumours gaining anatomical information about the tumour mass. Magnetic Resonance Imaging is in the standard of care both for diagnosis and therapy follow-up in many solid tumours. Several MRI-based sequences have been developed to study water tissue diffusion as qualitative indication of tissue cellularity and matrix density. In recent years, Dynamic-Contrast-Enhanced-MRI opened the possibility of "quantifying" the anatomy of the TME by means of a PK-based evaluation of the diffusion of contrast agent molecules across tumour vasculature[7]. When the bolus of contrast agent passes through the capillary bed, it is only temporarily confined to the vascular space. In many tissues, the contrast agent rapidly passes into the extracellular-extravascular space (called v_e, leakage space) at a speed that depends on the permeability and surface of the microvessel, and blood flow. By the analyses of this process, it is possible to estimate a parameter called the transfer rate constant (K_{trans}) representing the physiological phenomenon of transendothelial transport of the contrast agent. Finally, by evaluating the back-diffusion of the CA in the vessel allow to estimate the efflux rate constant (K_{ep})[61]. These parameters provide a quantitative framework describing the anatomy of the tumour and interestingly, allow to discriminate between tumours at different developmental stages[8,9].

In this chapter, exploiting the great predictive potential of PK models, the role that the use of specifically designed drug delivery systems (DDS) has in tailoring active agent bio-interactions in humans or relevant human models is explored. Simulink models are implemented to solve differential equations modelling the PK profile of free and nanoformulated active agents. As a first step, the implemented model was validated through clinical data about accumulation of Temozolomide in patients with high grade gliomas as a standard molecule, with great availability of clinical data. The same model was then implemented to describe the biodistribution and tumour accumulation of different nanoformulated agents highlighting the role of DDS in modulating their pharmacokinetic.

V.II. Experimental Section

The applied PK models were implemented using Simulink (Mathworks, R2021a), a graphical user modeling software package.

V.II.I. Clinical data-based validation of the implemented model

As first step, a three-compartment model was used to model TMZ biodistribution and accumulation in Cerebrospinal fluid (CSF) or brain extracellular fluid (ECF) after oral administration to patients

affected by high grade primary or recurrent gliomas. The first compartment is for the gastrointestinal tract (GI), the second compartment for plasma (PLASMA) and a third single compartment for the tumour entity, as reported by Gallo et al.[10], Figure 5.1

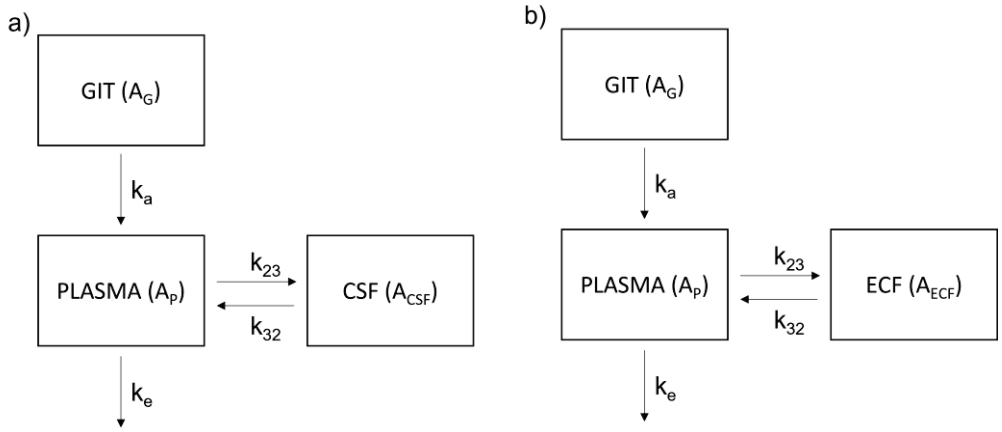

Figure 5.1 – Pharmacokinetic modelling of Temozolomide (TMZ) distribution and tumour accumulation after oral administration: a) in plasma and CSF; b) in plasma and ECF.

Equations were solved for each compartment as it follows:

TMZ accumulation in CSF:

Gastrointestinal tract

$$1)\ \frac{dA_G}{dt} = -k_a A_G$$

Plasma

$$2)\ \frac{dA_P}{dt} = k_{32}A_{CSF} + k_a A_G - k_{23}A_P - k_e A_P$$

Cerebrospinal Fluid

$$3)\ \frac{dA_{CSF}}{dt} = k_{23}A_P - k_{32}A_{CSF}$$

Temozolomide accumulation in ECF:

Gastrointestinal tract

$$1)\ \frac{dA_G}{dt} = -k_a A_G$$

Plasma

$$4)\ \frac{dA_P}{dt} = k_{32}A_{ECF} + k_a A_G - k_{23}A_P - k_e A_P$$

Extracellular Fluid

$$5)\ \frac{dA_{ECF}}{dt} = k_{23}A_P - k_{32}A_{ECF}$$

where A_G, A_P, A_{CSF}, A_{ECF} are the amount in the gastrointestinal tract, plasma, CSF and ECF compartments, respectively; k_a is the absorption rate constant; k_e is the elimination rate constant from the plasma; k_{23} and k_{32} are the transfer rate constants from plasma to CSF and from CSF to plasma in the first case while from plasma to ECF and from ECF to plasma in the second case.

Initial condition for concentration in the GI tract was set equal to the dose, while zero both in plasma and brain compartments.

The equations were implemented in Simulink according to the following scheme, in Figure 5.2:

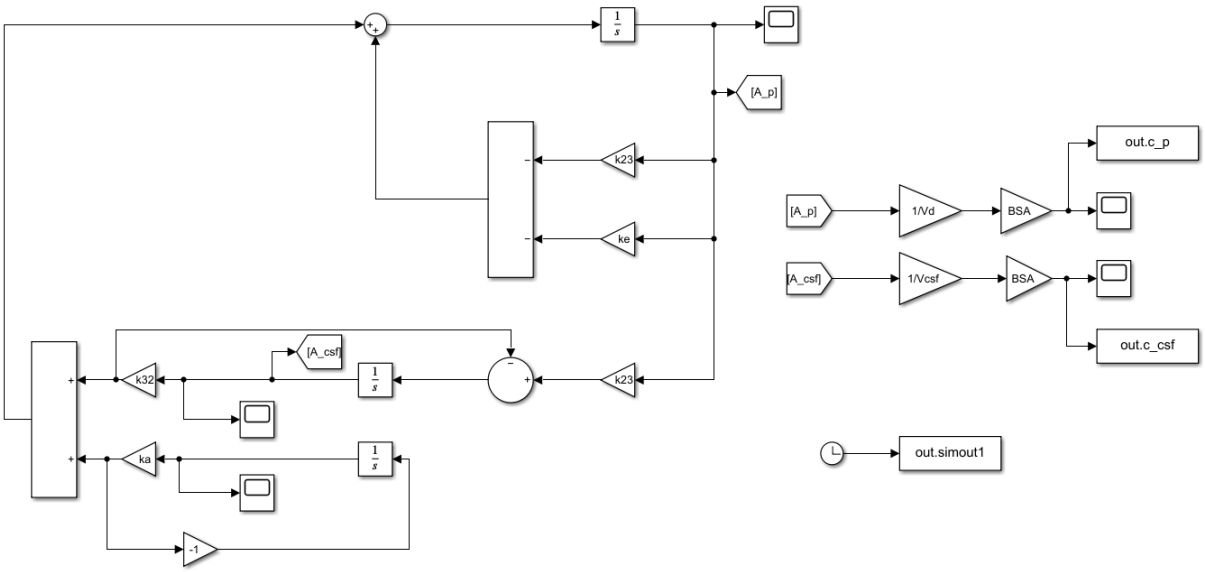

Figure 5.2 - Simulink scheme for TMZ distribution in high grade gliomas

Rate constants as well as relevant volumes for TMZ distribution model in human cerebrospinal fluid are taken from Ostermann et al.[4], and reported in the following Table 2.

Table 2 – PK parameters, rate constants and volumes used for simulation. k_a is the absorption rate constant; k_e is the elimination rate constant from the plasma; k_{23} and k_{32} are the transfer rate constants from plasma to CSF and from CSF to plasma; V_d is the volume of distribution of drug in plasma; V_{CSF} is the volume of CSF; BSA is the body surface area. All values were taken from a study by Ostermann et al.[4]

k_a $[h^{-1}]$	k_e $[h^{-1}]$	k_{23} $[h^{-1}]$	k_{32} $[h^{-1}]$	V_d $[L]$	V_{CSF} $[L]$	DOSE $[mg/m^2/day]$	BSA m^2
5.8	0.330	$7.2\ 10^{-4}$	0.76	30.3	0.4	75	1.8
5.8	0.330	$7.2\ 10^{-4}$	0.76	30.3	0.4	200	1.83

Rate constants as well as relevant volumes for TMZ distribution model in human extracellular fluid are taken from Portnow et al.,[11] and reported in the following Table 3.

Table 3 – Pharmacokinetic parameters for TMZ distribution in human extracellular fluid. k_a is the absorption rate constant; k_e is the elimination rate constant from the plasma, where the average is used; k_{32} is the transfer rate constants from ECF to plasma, where the average is used; k_{23} is the transfer rate constants from plasma to ECF, that is assumed three order of magnitude less with respect to the k_{32} as in the study from Ostermann et al.[4], V_d is the volume of distribution of drug in plasma, calculated as $\frac{DOSE}{k_e * AUC}$; V_{ECF} is the volume of ECF, calculated by considering that the volume of the brain is 1.2L in human and extracellular fluid is 26% of it; AUC is the area under the curve. All data were taken from Portnow at al.[11], if not differently specified.

Patient	$k_a\ [h^{-1}]$	$k_e\ [h^{-1}]$	$k_{23}\ [h^{-1}]$	$k_{32}\ [h^{-1}]$	$V_d\ [L]$	$V_{ECF}\ [L]$	AUC $[\mu g * h/mL]$
1	5.8	0.32	-	0.33	-	-	20.9
2	5.8	0.43	-	0.21	-	-	21.0
3	5.8	0.41	-	0.34	-	-	27.0
4	5.8	0.14	-	0.39	-	-	11.4
5	5.8	0.46	-	-	-	-	7.8
6	5.8	0.42	-	0.4	-	-	9.5
Avg	5.8	0.363	-	0.334	-	-	16.3
Calc	-	-	0.33410^{-3}	-	45.6	0.312	-

V.II.II. Use of nanoparticles for prolonged circulation time and reduced off target effect

CPT-11 or Irinotecan is a camptothecin pro-drug approved by FDA since 1994 for the adjuvant treatment of colon-rectal cancer and its pegylated-liposomal formulation ONYVIDE is approved since 1996 for the treatment of pancreatic adenocarcinoma. A single compartment model was used to compare the distribution process of systemically infused free drug and ONYVIDE with the aim of highlight the role of the drug delivery system in improving the circulation time of the drug, while reducing its off-target distribution in patients diagnosed with solid tumours.

The single equation implemented for the following PK modelling was:

$$\frac{dA_P}{dt} = -k_e A_P$$

Where A_P is the plasma concentration of CPT-11 or ONYVIDE and k_e their elimination constants.

This equation was implemented in Simulink as follows:

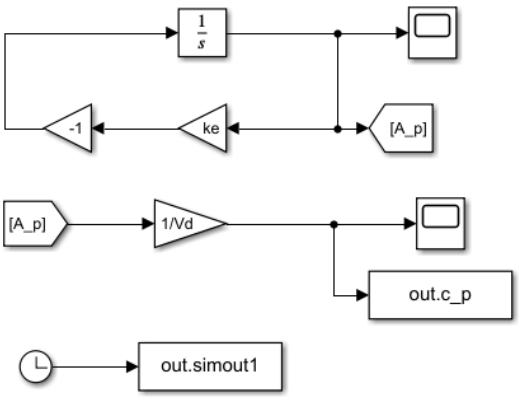

Figure 5.3 – Simulink scheme for PK modelling of CPT-11/ONYVIDE plasma curve.

Initial condition of the concentration was set equal to the total amount of infused drug (dose) as the rate of infusion is much higher than the rate of elimination thus the transitory phase of infusion was neglected. Relevant constants and volumes as well as infusion regimens were taken from two clinical studies by Chabot et al[12]., and Chang et al.[13] and reported in Table 4.

Table 4 - Pharmacokinetic parameters for CPT-11 and ONYVIDE distribution in human plasma of patients affected by solid tumours. k_e is the elimination rate constant from the plasma, V_d is the volume of distribution of drug in plasma; CL is the clearance. All data were taken from Chabot et al[12], and Chang et al.[13].

Compound	V_d	k_e	CL	CELLS	SUBJECTS	DOSE	INJECTION
CTP – 11[12]	152 L/m^2 145 L/m^2 155 L/m^2	0,10 h^{-1} 0,10 h^{-1} 0,08 h^{-1}	15,2 L/m^2h 14,7 L/m^2h 12,0 L/m^2h	Solid tumour	Humans	33-100 mg/m^2 115-350 mg/m^2 400-750 mg/m^2	INFUSION 30 min
ONIVYDE[13]	3,56 L/m^2 1,8 L/m^2 1,97 L/m^2	*0,075* h^{-1} *0,053* h^{-1} *0,060* h^{-1}	*0,269* L/m^2h *0,0591* L/m^2h *0,119* L/m^2h	Solid tumour	Humans	60 mg/m^2 120 mg/m^2 180 mg/m^2	INFUSION 90 min

V.II.III. Stage-dependent active agents tumour accumulation

A two-compartment model was used to model Gadodiamide accumulation in plasma extracellular fluid (ECF) of patients affected by all grade gliomas (Grade I, Grade II, Grade III, Grade IV) to model the systemic bolus injection of the contrast agent.

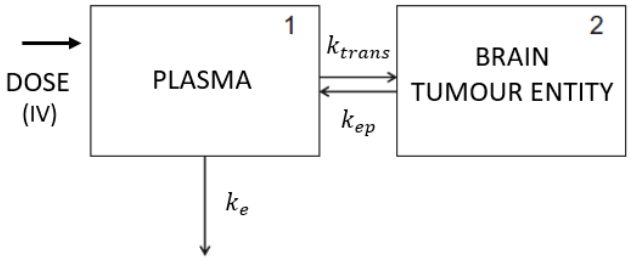

Figure 5.4 - Pharmacokinetic model after intravenous administration of the Gadodiamide for its distribution in the plasma and ECF brain tumour entity.

The correlated mass balance differential equation can be written as it follows:

Plasma

$$6)\ \frac{dA_P}{dt} = k_{ep}A_B - k_{trans}A_P - k_eA_P$$

ECF brain tumour entity

$$7)\ \frac{dA_B}{dt} = -k_{ep}A_B + k_{trans}A_P$$

where A_P, A_B are the amount in the plasma and ECF brain tumour entity compartments, respectively; k_e is the elimination rate constant from the plasma; k_{trans} = k_{12} is the forward transfer rate constant; k_{ep} = k_{21} is the backward transfer rate constant.

To solve the equations the following Simulink® scheme was implemented:

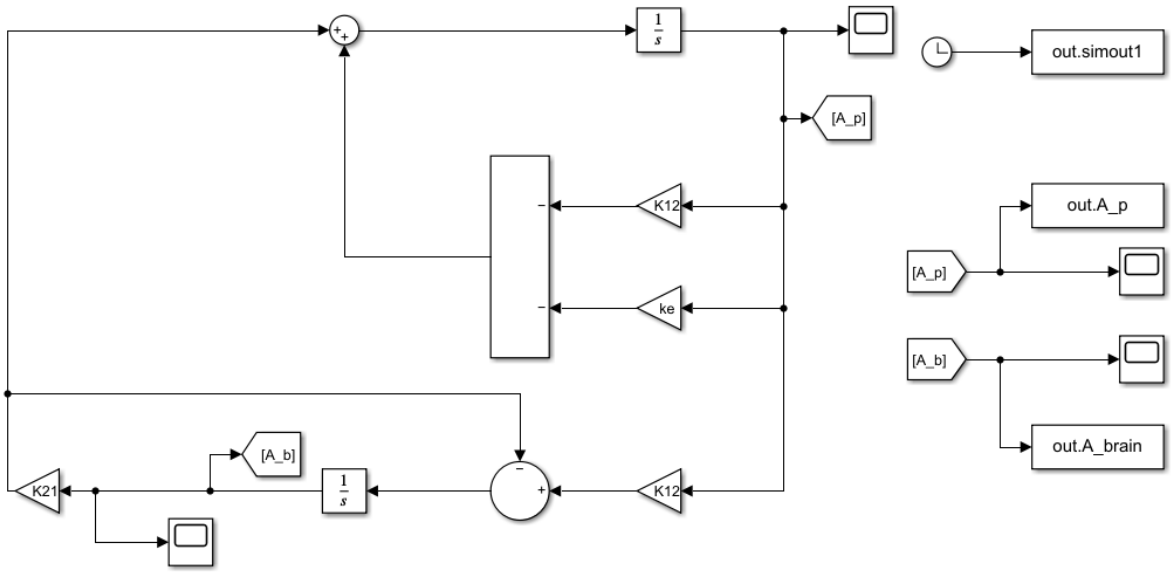

Figure 5.5- – Simulink scheme for PK modelling of Gadodiamide grade-dependent accumulation in brain extracellular fluids of patients

The initial condition of concentration was set equal to the dose for the plasma, and equal to zero in ECF brain tumour compartment.

Relevant transfer rate constants and volumes were taken from a clinical study by Zhao et al[14].

Table 5 – Pharmacokinetic parameters for the Gadodiamide in human case depending on the tumour grade. k_e is the elimination rate constant from the plasma; $k_{trans} = k_{12}$ is the forward transfer rate constant; $k_{ep} = k_{21}$ is the backward transfer rate constant; v_e is the volume of extracellular-extravascular space. All values were taken from Zhao et al.[14]

GRADE	k_{trans} $[h^{-1}]$	k_{ep} $[h^{-1}]$	v_e	k_e $[h^{-1}]$	DOSE [g]
I	$1{,}05 * 10^{-3}$	$5{,}23 * 10^{-3}$	0,251±0,106	1.5	4.192
II	$4{,}52 * 10^{-3}$	0,0137	0,387±0,154	1.5	4.192
III	0,0123	0,0163	0,799±0,204	1.5	4.192
IV	0,019	0,0237	0,817±0,121	1.5	4.192

V.II.IV. Engineering active agents for improved tumour accumulation

A two-compartment model was used to compare the transport properties of ANG1005 (an Angiopep-2 molecule chemically conjugated to three molecules of Paclitaxel) and free Paclitaxel across the BBB of healthy and tumour bearing rats by evaluating their accumulation in plasma extracellular fluid (ECF) upon systemic administration. The comparison of the transport properties of the two systems between healthy and tumour bearing rats is performed.

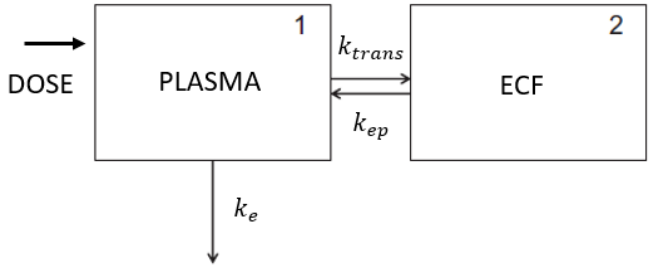

Figure 5.6 - Pharmacokinetic model after intravenous administration of the ANG1005 and Paclitaxel for their distribution in the plasma and ECF.

The correlated mass balance differential equation can be written as it follows:

Plasma

$$8)\ \frac{dA_P}{dt} = k_{ep}A_{CEF} - k_{trans}A_P - k_eA_P$$

ECF brain tumour entity

$$9)\ \frac{dA_{ECF}}{dt} = -k_{ep}A_{ECF} + k_{trans}A_P$$

where A_P, A_{ECF} are the amount in the plasma and ECF compartments, respectively; k_e is the elimination rate constant from the plasma; $k_{trans} = k_{12}$ is the forward transfer rate constant; $k_{ep} = k_{21}$ is the backward transfer rate constant.

To solve the equations the following Simulink® scheme was implemented:

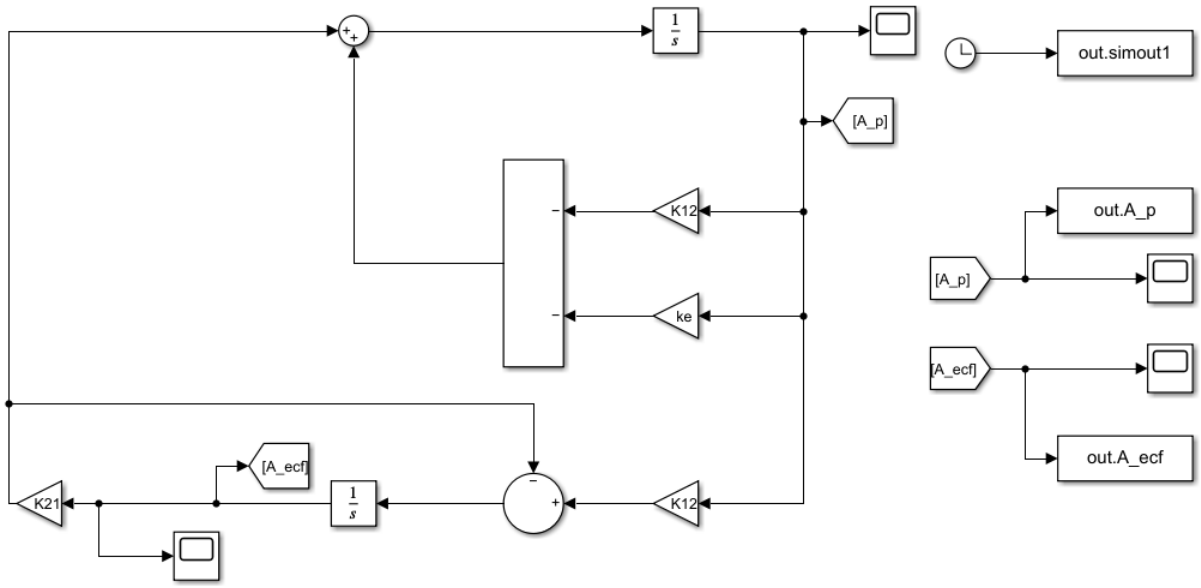

Figure 5.7 - Block representation of the pharmacokinetic model after intravenous administration of the ANG1005 and Paclitaxel for their distribution in the plasma and ECF brain tumour entity.

Table 6 - Pharmacokinetic parameters for the drug delivery system, ANG1005, and the free drug, Paclitaxel, in rat case. Vd is the volume of distribution of drug in plasma; ke is the elimination rate constant from the plasma, for the ANG1005 calculated as CL/Vd while for the Paclitaxel calculated as 0.693/ke; CL is the clearance, the rate at which the active drug is removed from the body; t(1/2) half-life; AUC is the area under the curve of the concentration-time profile; cmax is the maximum concentration plasma.

Compound	V_d	CL	k_{el}	AUC_{PLASMA}	$t_{1/2}$	c_{max}	CELLS	WEIGHT	DOSE	INJECTION
ANG1005[15]	522 mL/m^2	157,8 mL/m^2h	0,302 h^{-1}	379 $\mu g\ h/mL$	-	-	U87	200-250 g	10 mg/kg	BOLUS
Paclitaxel[16]	-	-	0,097 h^{-1}	1275,2 $\mu g\ h/L$	7,12 h	957 $\mu g\ /L$		180-220 g	3 mg/kg	BOLUS

Table 7 - Pharmacokinetic parameters for the drug delivery system, ANG1005, and the free drug, Paclitaxel, in rat case. $k_{trans} = k_{12}$ is the forward transfer rate constant; $k_{ep} = k_{21}$ is the backward transfer rate constant. All parameters were taken from a study by Thomas et al.[17]

Compound	k_{trans}	k_{ep}	Cells	WEIGHT	DOSE	INJECTION
ANG1005[13]	$7{,}3 * 10^{-3}$ $mL/(g * s)$	$9 * 10^{-4}$ $mL/(g * s)$	-	200-250 g	10 mg/kg	INFUSION
ANG1005[13]	$9{,}636 * 10^{-3}$ $mL/(g * s)$	$11{,}88 * 10^{-4}$ $mL/(g * s)$	MDA-MB-231 (Breast Cancer) 4-6 weeks	200-250 g	10 mg/kg	BOLUS
Paclitaxel[13]	$8{,}5 * 10^{-5}$ $mL/(g * s)$	$8{,}5 * 10^{-6}$ $mL/(g * s)$	-	200-250 g	10 mg/kg	INFUSION
Paclitaxel[13]	$32{,}55 * 10^{-5}$ $mL/(g * s)$	$32.55 * 10^{-6}$ $mL/(g * s)$	MDA-MB-231 (Breast Cancer) 4-6 weeks	200-250 g	10 mg/kg	BOLUS

The initial condition of concentration was set equal to the dose for the plasma, and equal to zero in ECF brain tumour compartment. In case of healthy animals, systemic infusion was performed but as reported for ONYVIDE we neglected the transitory phase due to infusion. For tumour bearing rats a systemic bolus injection was performed.

V.III. Results

V.III.I. Clinical data-based validation of the implemented Simulink scheme

To build a PK scheme able to reliably model nanoformulated drug distribution and tumour accumulation in humans, the first step was the validation of the implemented model by clinical data. Temozolomide (TMZ), the standard of care in the treatment of gliomas, was used as a reference molecule for the wide availability of clinical data.

In 2004, Ostermann et al.[4] measured the TMZ concentration in plasma and cerebrospinal fluid (CSF) in a cohort of 35 patients with newly diagnosed or recurrent malignant gliomas belonging to the pilot study and recurrent study, respectively. The gliomas, as reported in Table 5, were either of third or fourth grade. Patients of different gender, age, and heights were involved in the study.

Table 5 – Patient demographics and baseline disease

	***Pilot study*[3]**	***Recurrent study*[3]**
Number of patients	23	12
Age	50 (36-65)	49 (30-79)
Body weight (kg)	72 (46-105)	72 (53-85)
Height (cm)	169 (150-188)	170 (151-181)
BSA (m^2)	1,80	1,83
Gender	15/8 M/F	9/3 M/F
Glioblastoma multiforme (GMB)	23 (100%)	8 (67%)

Anaplastic astrocytoma/ Anaplastic oligoastrocytoma (AA/AOA)	0	4 (33%)

It is important to note that except for the administered dose, higher for recurrent tumours, the parameters are the same both for the pilot study and the recurrent study. As reported in the dedicated method section, a three-compartment model was used to describe TMZ distribution and accumulation in Simulink. The concentration-time curves for the plasma and the CSF are reported in Figure 5.8 for both doses. Results show an increase in concentration due to the absorption phase, with the peak reached in 1.5h followed by and an exponential decay due to distribution and elimination phases. Coherently, the concentrations ranged from 0.10 to 13.99 $\mu g/mL$ in the plasma and from 0.16 to 1.93 $\mu g/mL$ in the CSF, in accordance to Ostermann et al.[4] findings.

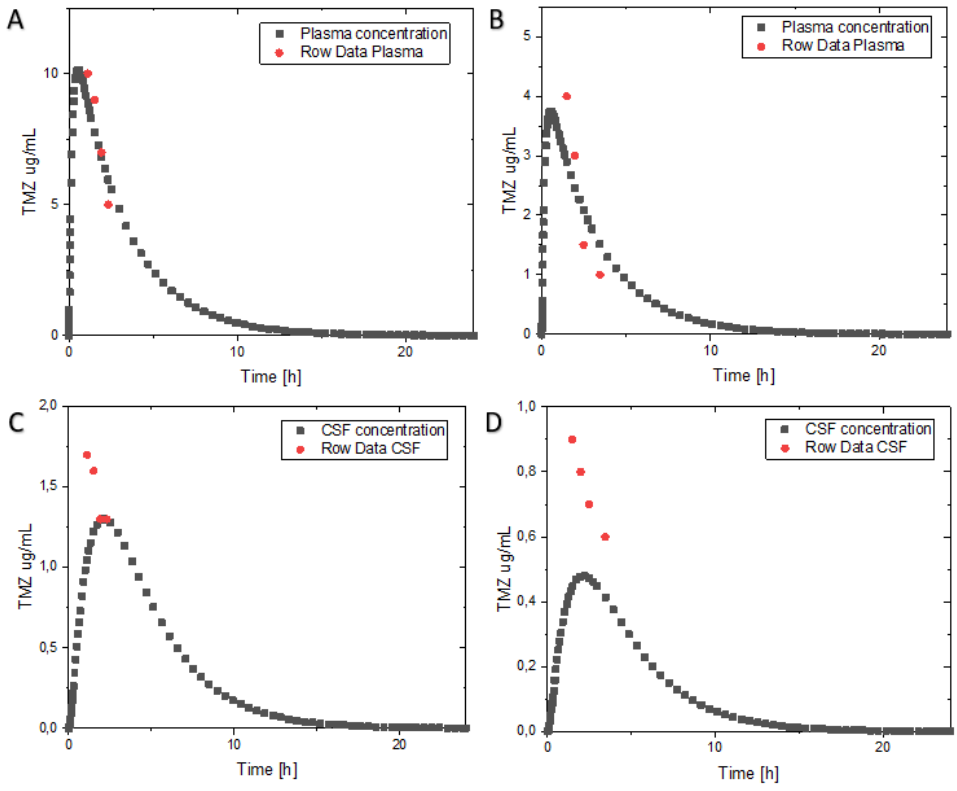

Figure 5.8 – Pharmacokinetic profile of TMZ after oral administration vs Row Data: A) in plasma at a Low dose = 75 $mg/m^2/day$; B) in plasma at High dose = 200 $mg/m^2/day$; C) in CSF at a Low dose = 75 $mg/m^2/day$; D) in CSF at a High dose = 200 $mg/m^2/day$.

The R^2 was calculated as a measure of the quality of the model in fitting experimental data. In plasma, an optimum correlation was found with R^2 equal to 0.9616 and 0.9323 for the low dose and high dose respectively. In the case of CSF, the correlation was suboptimum with R^2 equal to 0.8027. This difference can be explained by the reduced size of the experimental set of data points for CSF

concentration (n=47) which is much reduced with respect to the plasma data set (n =227). The same uncertainty was found by the authors which found a poor correlation between the data acquired from different patients highlighting how both the transfer rate constant k_{23} as well as the absorption rate from gastrointestinal tract were subjected to significant inter-patient differences. Due to the poor correlation found in the CSF a further investigation of the TMZ distribution in high grade human gliomas was analysed.

A second case study by Portnow et al.[11], was taken into consideration. It reported a study of TMZ deposition in patients with high grade gliomas, by measuring directly extracellular fluid concentrations of the drug. The concentration-time profile for the plasma and the ECF are presented in Figure 5.9. TMZ peak levels are reached very fast in plasma and later in ECF, with a gradual decrease over time. It is worth of notice that despite the standard deviation of measurements in the dataset is high, the R^2 for the concentration curve in the ECF shows ab optimum correlation, being equal to 0.902.

From this result, it is possible to conclude that the validation of the pharmacokinetic model for the TMZ deposition in human high-grade gliomas was achieved, with curves reliably fitting experimental data.

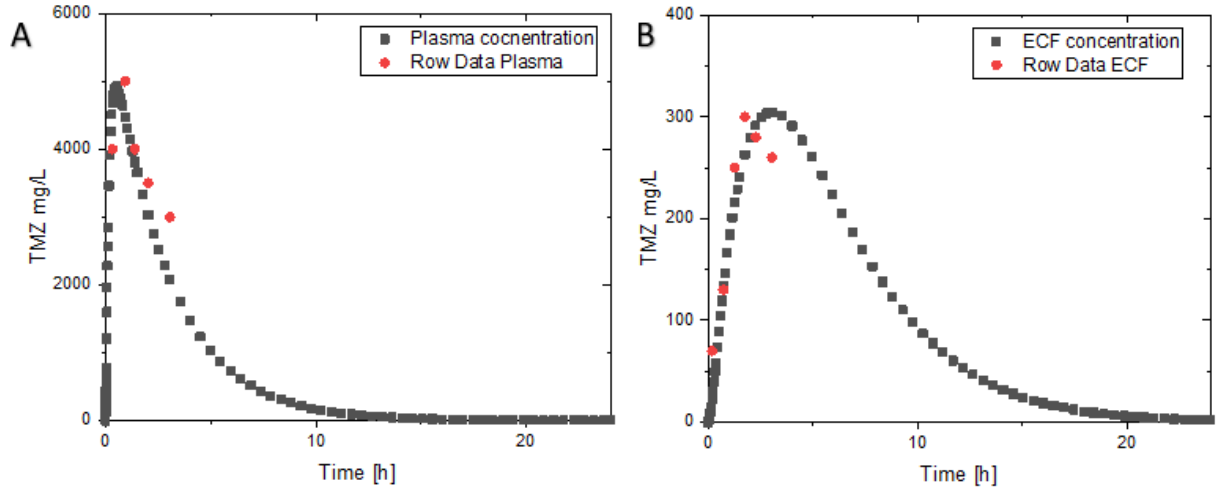

Figure 5.9 – Pharmacokinetic profile of TMZ after oral administration vs Row Data, Dose = 150 $mg/m^2/day$.

V.III.II. Use of nanoparticles for prolonged circulation time and reduced off target effect

The clinically-validated model implemented in Simulink was used to preliminary investigate the role of nanomedicines in improving the circulation and decreasing off-target accumulation of active agents. The camptothecin prodrug Irinotecan (CPT-11) is approved as adjuvant therapy in the treatment of colon-rectal cancer. The poor water solubility of its active metabolite SN-38 and instability occurring at the physiological of pH 7.2, lead to the development of ONIVYDE, a pegylated

liposomal formulation of CPT-11 approved since 1996 for the treatment of the adenocarcinoma of the pancreas. In this section, the critical analysis of clinical data from different phases clinical trials of patient with advanced solid tumours[12,13], is used to highlight the role of the nanoformulations in improving the circulation time of this drug as well as reducing its off-target accumulations impacting directly both on its efficacy and toxicity. Clinical data from separate studies and their relative PK constants were used to model the plasma concentration curve over time as described in the dedicated method section. Results in Figure 5.10 compare the plasma concentration curve for both the free and the nanoformulated CPT-11 clearly revealing the role of the drug delivery system (DDS). First, despite administration of the very same dose, the amount of drug found in plasma over time is much higher for the nanoformulated drug with respect to the free drug. Please note that both administrations occurred by means of systemic infusion. The significantly lower amount of free drug found in plasma revealed that during the time needed for infusing the whole dose, the distribution in peripheral compartment was a competing mechanism. This hypothesis is confirmed by the very high measured volume of distribution ($152\ L/m^2$). This effect could be observed only for ONYVIDE administered at a lower dose, which indeed showed a much higher volume of distribution if compared to the other two administration dosages ($3.52\ L/m^2$). Despite this, the nanoformulated drug has a much longer circulation time and at ay concentration a two-orders of magnitude lower volume of distribution with respect to the free drug. As a conclusion, the nanoformulation ONYVIDE is both prolonging drug circulation time, potentially improving its ability of accumulating in the tumour, as well as reducing the off-target distribution of the drug.

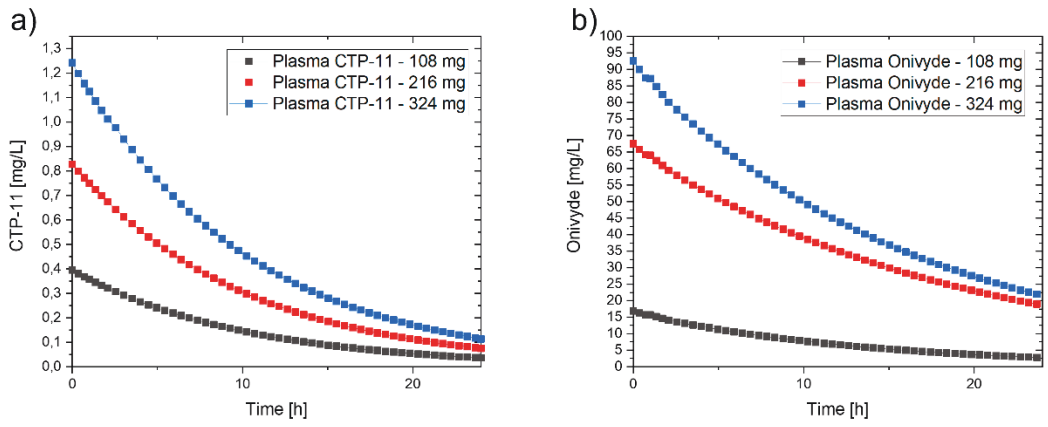

Figure 5.10 - Plasma concentration-time curve of free and nanoformulated CPT-11 at three different doses, 60, 120, 180 mg/m^2. a) Plasma curve of free CPT-11; b) Plasma curve of ONYVIDE (nanoformulated CPT-11).

V.III.III. Stage-dependent active agents tumour accumulation

After the determination of the role of nanoformulated agents in improving active agent interaction with plasma components as well as guaranteeing a selective accumulation in the desired target, this section aims to highlight how, before moving to the study of tumour accumulation of active agents and the prediction of their transport properties at the tumour site, gaining information about the stage of the disease with the consequent changes in TME is crucial. A study by Zhao et al.[14], presented the quantification of tumour-associated parameters (transfer rate constant k_{trans}, extracellular volume v_e, backward transfer rate constant k_{ep}) in patients affected by different grades gliomas by quantitative DCE-MRI. In this study, 80 patients including 20 cases of grade I astrocytoma, 12 cases of grade II astrocytoma, 8 cases of grade II oligodendroglioma, 20 cases of grade III astrocytoma, and 20 cases of grade IV glioblastoma underwent MRI[14]. The values of k_{trans}, k_{ep} and v_e in tumor and peritumor edema were measured and revealed significant differences between low-grade and high-grade gliomas. It is worth noticing that the forward transfer rate constant, k_{trans}, and the backward transfer rate constant, k_{ep} were obtained directly form the images and were grouped according to the glioma grade allowing a differentiation between the different stages.

These parameters were used to model Gadodiamide distribution in tumors and highlighted the consequent grade-related differences in tumor accumulation and clearance. Indeed, we expect that as the grade increases, the impairment of the BBB increases as well as the Blood-Tumor-Brain Barrier, which is characterized by a much higher permeability, a higher amount of CA can penetrate inside the tumor. In addition, since the IFP and the activity of P-efflux pumps increase, a consequent faster clearance of the active agent from the tumor is expected.

As reported in the dedicated method section, contrast agent deposition in the tumor was modeled by a two-compartment model.

The concentration-time profile for the plasma and the ECF of the tumour are presented in Figure 5.11. Plasma and ECF concentrations for each tumour grade are reported as percentage of the injected dose to highlight the influence of the tumour grade on the distribution accumulation of the contrast agent.

Results show that by increasing the tumour grade, the ECF concentration curves dramatically change, Figure 5.11b. The peak concentration increases with tumour grade meaning that the amount of gadolinium that reaches the brain grows. This is representative of the degree of dysfunction and destruction of the BBB that leads to increased contrast agent extravasation. Moreover, the slope of the second portion of the curve increases. This fact is indicative of the re-entry of gadolinium in plasma circulation as well as clearance due to the efflux mechanism at the BBB and the formation of wider fenestrations whose dimension is linked to the grade of the tumour. Those results are consistent with the study conducted by Tofts[18] in 2010 who investigated the role of each DCE-MRI derived parameter has in influencing the overall distribution of the active agent in the brain. He

demonstrated that by fixing the extravascular-extracellular volume v_e, as the incoming flow increases, the initial slope of the curve and the peak increases, as it happens for increasing grades in our simulation, Figure 5.10b. Additionally, he proved that k_{ep} influences the shape of the second part of the curve as it is visible in our results. As a conclusion, applying the PK modelling to describe the transport of contrast agents in different grade gliomas we proved that the anatomical features of the tumour and specifically the characteristics of the tumour microenvironment are crucial in determining the transport properties of active molecules and can be investigated by PK modelling. In the analysed case the very same active agent was administered at the same dose and revealed completely different levels of tumour accumulation and clearance.

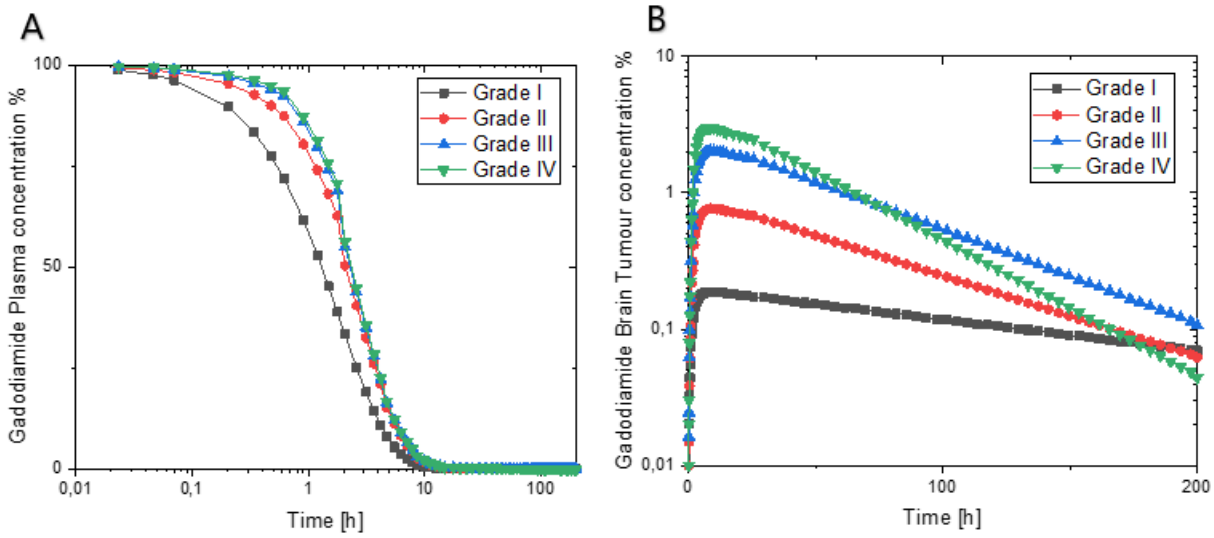

Figure 5.11 – Pharmacokinetic profile of Gadodiamide after intravenous injection: A) in plasma at different tumour grade; B) in ECF at different tumour grade.

V.III.IV. Engineering active agents for improved tumour accumulation

After revealing the importance of the characterization of the patient-specific anatomy of the tumour microenvironment before the treatment scheduling, the impact of nanoformulations in improving drug tumour accumulation was assessed.

In this regard, a two-compartment PK model is applied to reveal the mechanism of glioma deposition of the free drug paclitaxel and compare it with ANG1005, a drug-peptide conjugate, in which paclitaxel is engineered with a molecule of Angiopep-2 to specifically cross the BBB. Despite being in clinical trial, a complete set of clinical data about tumour deposition of ANG1005 is not available. For this reason, a comprehensive PK modelling was performed on a rat model. Brain deposition of the two formulations was compared and evaluated both for healthy and tumour bearing animals to

mimic very early stages of the tumour characterized by a healthy and poorly permeable BBB and a leaky barrier in case of advanced pathology.

To implement the model, different studies were analysed and constants about both whole body biodistribution and tumour accumulation were collected, as reported in the dedicated method section. It is important to highlight that the purpose of this investigation is the understanding of the role of the nanoformulated ANG1005 in improving the tumour accumulation of paclitaxel more than the study of drug biodistribution. For this reason, studies about the intravenous infusion of the formulations were analysed in order to study the molecule brain accumulation when a given, homogeneous plasma concentration in present. For this reason, absolute values in terms of amount of drug accumulated should not be taken into consideration.

The concentration-time plasma and the ECF curves for healthy and tumour bearing animals are presented in Figure 5.12 a and b, respectively. They clearly reveal that in presence of the tumour a higher amount of drug can penetrate inside the brain much faster than in case of healthy animals. Additionally, as from the presence of a leaky BBB a much faster clearance of the drug can be observed.

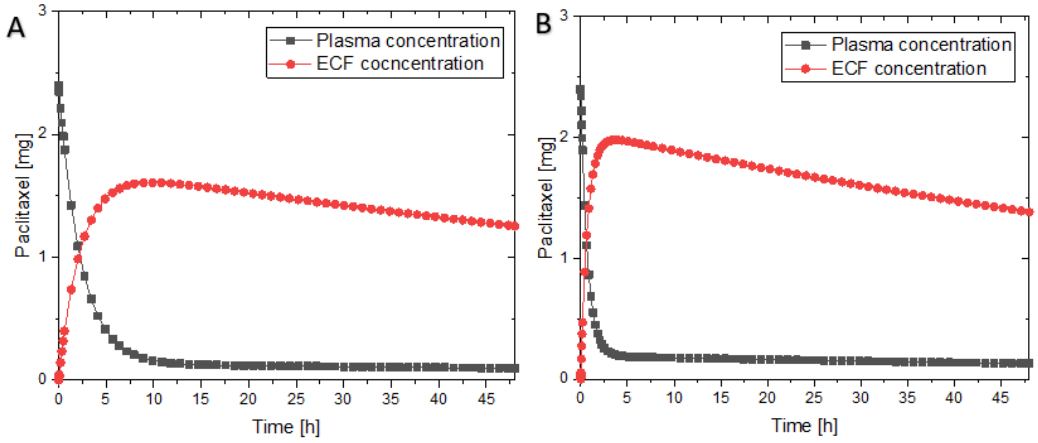

Figure 5.12 – Pharmacokinetic profile of Paclitaxel after intravenous injection in plasma and in ECF: A) healthy subjects; B) subjects with tumour.

The same results were analysed for ANG1005 and presented in Figure 5.13. Strikingly, the amount of ANG1005 that can enter the CNS is independent on the presence of the tumour with very similar results obtain both for health and tumour bearing mice. These results support the experimental and clinical evidence of the improved transport of ANG1005 at the BBB with respect to free paclitaxel. Additionally, they demonstrate how the use of a specific drug delivery system that can specifically interact with disease-related biological barriers can drastically change the effectiveness of a formulation strongly reducing the dependence on stage-related tissue festures.

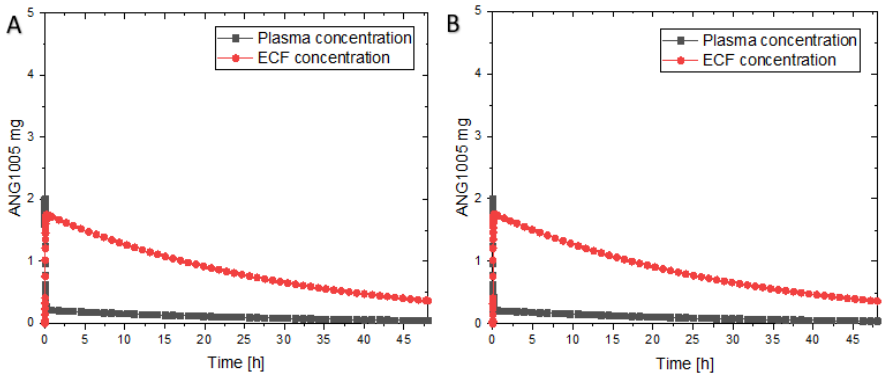

Figure 5.13 – Pharmacokinetic profile of ANG1005 after intravenous injection in plasma and in ECF: A) healthy animals; B) tumour-bearing animals.

V.IV. Conclusions

In this section we explored the potential that pharmacokinetic modelling has in the investigation of the role of drug delivery systems in improving the pharmacokinetic of approved active agents on the basis of clinically relevant data. For modelling, classical PK was preferred to physiologically based models since the validation through clinical data was preferred to the use of more detailed compartments.

The developed models were first validated by fitting through clinical data and then applied for the macroscopic evaluation of different level nano-bio-interactions. First, CPT-11 and its liposomal formulation were compared in terms of circulation time and peripheral tissue distribution demonstrating a strongly reduced off-target accumulation and a prolonged circulation time of the nanoformulated ONYVIDE. Secondly, DCE-MRI derived parameters for different grade gliomas were used to demonstrate the crucial need of deeply characterizing and understanding the stage of the faced pathology during the design of new formulations. Finally, the ability of a drug delivery system of successfully overcome some disease-specific biological barriers was demonstrated by means of the comparison of free Paclitaxel and ANG1005 accumulation in rat brains. Through this model, the effectiveness of ANG10005 in improving the accumulation of the active agent Paclitaxel in the brain was demonstrated in a tumour-independent fashion as a result of the improved transport properties of the formulation guaranteed by the specific interaction of Angiopep-2 with LRP1 receptors overexpressed at the BBB.

As a conclusion, the developed clinically-relevant models can aid in the rational design of drug delivery system as well as in predicting the effectiveness of specific treatment regimens, adjust administered doses and preliminary evaluating toxic effects of nano-formulations.

V.V. Reference

1 Zhou, Q. & Gallo, J. M. The pharmacokinetic/pharmacodynamic pipeline: translating anticancer drug pharmacology to the clinic.

2 Gerlowski Le Fau - Jain, R. K. & Jain, R. K. Physiologically based pharmacokinetic modeling: principles and applications.

3 Zhou, Q. *et al.* Predicting human tumor drug concentrations from a preclinical pharmacokinetic model of temozolomide brain disposition.

4 Ostermann, S. *et al.* Plasma and cerebrospinal fluid population pharmacokinetics of temozolomide in malignant glioma patients.

5 Sykova, E. & Nicholson, C. Diffusion in brain extracellular space. *Physiological Reviews* **88**, 1277-1340, doi:10.1152/physrev.00027.2007 (2008).

6 Ferretti, S., Allegrini, P. R., Becquet, M. M. & McSheehy, P. M. J. Tumor Interstitial Fluid Pressure as an Early-Response Marker for Anticancer Therapeutics. *Neoplasia* **11**, 874-881, doi:10.1593/neo.09554 (2009).

7 Gordon, Y. *et al.* D ynamic contrast-enhanced magnetic resonance imaging: fundamentals and application to the evaluation of the peripheral perfusion. *Cardiovascular Diagnosis and Therapy*, doi:- 10.3978/j.issn.2223-3652.2014.03.01 (2014).

8 Wake, N. *et al.* Accuracy and precision of quantitative DCE-MRI parameters: How should one estimate contrast concentration? *Magnetic Resonance Imaging* **52**, 16-23, doi:10.1016/j.mri.2018.05.007 (2018).

9 Zikou, A. *et al.* Radiation Necrosis, Pseudoprogression, Pseudoresponse, and Tumor Recurrence: Imaging Challenges for the Evaluation of Treated Gliomas. *Contrast Media & Molecular Imaging*, doi:10.1155/2018/6828396 (2018).

10 Gallo, J. M. *et al.* Pharmacokinetic model-predicted anticancer drug concentrations in human tumors.

11 Portnow, J. *et al.* The Neuropharmacokinetics of Temozolomide in Patients with Resectable Brain Tumors: Potential Implications for the Current Approach to Chemoradiation. *Clinical Cancer Research* **15**, 7092-7098, doi:10.1158/1078-0432.ccr-09-1349 (2009).

12 Chabot, G. G. *et al.* Population pharmacokinetics and pharmacodynamics of irinotecan (CPT-11) and active metabolite SN-38 during phase I trials.

13 Chang, T. C. *et al.* Phase I study of nanoliposomal irinotecan (PEP02) in advanced solid tumor patients. *Cancer Chemotherapy and Pharmacology* **75**, 579-586, doi:10.1007/s00280-014-2671-x (2015).

14 Zhao, M. *et al.* Quantitative analysis of permeability for glioma grading using dynamic contrast-enhanced magnetic resonance imaging. *Oncology Letters* **14**, 5418-5426, doi:10.3892/ol.2017.6895 (2017).

15 Gabathuler, R., Castaigne, J.-P., Goodfellow, G., Demeule, M. & Lawrence, B.

16 Li, J. *et al.* Pharmacokinetic profile of paclitaxel in the plasma, lung, and diaphragm following intravenous or intrapleural administration in rats. *Thoracic Cancer* **6**, 43-48, doi:10.1111/1759-7714.12139 (2015).

17 Thomas, F. C. *et al.* Uptake of ANG1005, a novel paclitaxel derivative, through the blood-brain barrier into brain and experimental brain metastases of breast cancer.

18 Tofts, P. (MAGNETOM Flash · 3/2010 · www.siemens.com/magnetom-world, 2010).

VI. Conclusions and Discussion

Nanomedicine holds great potential in improving the effectiveness of traditional medicine for several pathologies and over years demonstrated to have a huge impact on patient quality of life. An example from the contemporary pandemic era is the recently approved anti-Covid-19 vaccine COMIRNATY[1] that is based on the transport of RNA molecules in lipid nanoparticles. This nanomedicine-based strategy allowed to overcome limitations proper of nucleic acid transport, stability and degradation in human body and is successfully limiting the spreading of Covid-19 virus in the population of the entire globe.

Despite this incredible achievement however, there are still pathologies such as solid tumours which cannot fully benefit from the potentialities of nanomedicine as demonstrated by the very poor number of nanomedicine-based formulations that succeed to be translated in the clinical treatment of cancer.

Many decades of research led to the development of sophisticated, smart and stimuli responsive nanoformulations that demonstrated incredible technological capabilities, multimodal imaging properties and theranostic capacities with promising in-vitro and preclinical results paving the way to the early diagnosis, effective therapy, and improved follow up of many different solid tumours. However, the majority of nanomedicines still fail in determining improved outcomes in patients as well as reducing off-target effects. The main reason underlying these inabilities is the poor understanding of the impact that nanoparticle structural characteristics, and thus their synthetic identity, has on the fate of the nanoformulation in the biological environment and specifically on the transport in the tumour microenvironment. When in human body, a unique set of nano-bio-interactions for each specific nanoparticle design arise, aiding to the definition of a carrier biological identity which is ultimately responsible for the in-vivo fate as well as the in-vivo effectiveness of the formulation regardless diagnostic or therapeutic potential of the delivered agents. In 1907 the *magic bullet* theory by Paul Ehrlich for the first time conceptualized the idea of drugs that go straight to their intended cell-structural targets. In Ehrlich's theory, the idea of a *targeted therapy* came from the discovery of dyes that demonstrated a high affinity for specific cellular and subcellular compartments, and for this reason had a strong molecular basis. Over years, Ehrlich's theory and the more general concept of targeted therapy in cancer underwent an evolutionary path and for the last 20 years a paradigm shift led scientists to understand that the targeting ability of a formulation and thus its specific interaction with the target is not solely dependent on the molecule itself but possibly more on its transport to the target site. In the scientific community has raised the awareness about the relevance of themes such as protein corona formation in blood circulation, nanoparticle tissue diffusion and mechanisms of cellular uptake as phenomena equally impacting the targeting ability of a formulation as well as its affinity for the molecular target does. However, despite the huge efforts toward this direction, the current knowledge regarding nano-bio-interactions is still in an embryonal stage because of the use of standard and poorly reliable

probes for the investigation of macroscopic and molecular nano-bio-interactions as well as poorly relevant models of the biological environment.
In this framework, in my thesis I explored the field of theranostics developing a library of clinically relevant probes based on the use of materials that are FDA approved or in clinical trials. The development of these theranostic vectors allowed to highlight mechanisms proper of nanomaterials interaction with the biological environment and for this reason I used them to investigate nano-bio-interactions at different levels, from the molecular to the cellular and tissue level.

In first part of the thesis, a highly controllable, scalable and versatile microfluidic Hydrodynamic Flow Focusing (HFF) was used to implement a nanoprecipitation process exploited to produce a library of hydrogel-based nanoparticles with different synthetic identities. Feasibility studies were conducted for each system to study the impact of process parameters, polymer molecular weight and active agent encapsulation on the thermodynamic processes governing particle production as well as the impact of the co-encapsulation of hydrophilic or hydrophobic compounds on the well-known property of structured hydrogels, the Hydrodenticity. Herein, we demonstrated that microfluidics offers unique possibilities of tightly controlling the production process of nanoparticles, finely tailoring their properties, allowing to achieve high encapsulation efficiencies, and guaranteeing high uniformity of the final product. The effect of co-encapsulated agents on the hydration degree of the clinically approved contrast agent, Gd-DTPA was assessed to study the modulation of the Hydrodenticity property in presence of hydrophobic compounds such as CPT-11, a camptothecin prodrug approved for the treatment of many solid tumours, in the design of multimodal or theranostic crosslinked hyaluronic acid nanoparticles (cHANPs, Thera-cHANPs). Furthermore, the microfluidic processing of a high molecular weight HA was successfully implemented and the MW impact on the encapsulation efficiency of multiple agents, the Hydrodenticity property as well as particle stability was assessed. Additionally, a one-step crosslinking and PEGylation of the nanoparticle was achieved through a Michael addition reaction with a molecule-by-molecule control of the reactive functional groups allowing to achieve a strongly improved efficiency of the reaction with respect to its batch implementation. The use of a four arms PEG-VS with four-times higher number of functional groups was explored to modulate the crosslinking density of the particle and tune the Hydrodenticity property. The co-encapsulation of multiple agents allowed to confer multimodal imaging to the probe.
Overall, these results demonstrated the successful production of a well-controlled and deeply characterized library of nanoparticles made of FDA approved materials and with different synthetic identities and functionalities by means of microfluidics, a technology that is already widely recognized as “disruptive” in the field of translational medicine for the offered fine control over product features, uniformity of the product and scalability.

As a second step, the connection between the synthetic identity of the developed nanoparticles and their biological identity was assessed. cHANPs and PEG-cHANPs stability in differently composed biological sera was studied both in terms of surface properties and morphology. Through a comparison with the hydrophobic, commercially available polystyrene NPs the specific role of the surface hydrophilicity provided by the hydrogel network and the tailoring of the superficial stealth properties by means of surface conjugation with a custom PEGylated zwitterionic compound (Zwit-cHANPs) was studied. We proved that besides the well-known stealth properties of PEG, HA is also able to modulate protein absorption on the particle surface preserving both particle morphology and surface properties. Additionally, we successfully demonstrated in-vitro that both cHANPs and PEG-cHANPs escape the capture by circulating macrophages up to 6h of contact while preserving a significant uptake by U87, as a model of target cells. This allowed us to prove that the use of a coprecipitated matrix of HA and PEG in PEG-cHANPs permitted to successfully modulate the PEG dilemma effect, referring to the steric hindrance that the hydrated layer formed on the particle surface produces, reducing the uptake by target cells. Despite this promising result, literature is providing additional evidence of the negative impact that PEGylation has on the in-vivo fate of nanoparticles. Clinical data are contradicting the claim of PEG non immunogenicity with anti-PEG antibodies detected in the plasma of many subjects injected with PEG-containing formulations. This phenomenon works against the prolonged circulation offered by PEG for the reduced capture by RES macrophages because of the Accelerated Body Clearance (ABC) due to the immune response. For this reason, we concluded that the use of alternative highly hydrophilic, hydrogel forming polymers, such as HA, can successfully substitute the PEG in guaranteeing long circulation time, reduced protein corona formation with consequent reduced capture by circulating macrophages while preserving a significant uptake by target cells. Regarding this latter feature, multiple aspects could be further investigated to improve the level of comprehension of particle uptake mechanism and kinetic. Indeed, additionally to the evaluation of the successful particle uptake, the mechanism of particle internalization could be assessed. Francia et al.[2], recently demonstrated that protein corona can affect the uptake mechanism in a cell-dependent fashion, thus a comparison between the different investigated systems might be beneficial to understand the nanoparticle-specific protein corona impact on cellular uptake. Additionally, the intracellular fate of Zwit-cHANPs as a pH responsive system, can be investigated since they might play a role in the nanoparticle lysosomal escape and cytosol delivery of active agents.

The next level of nano-bio-interaction investigation was the nanoparticle interaction with complex three-dimensional tissues able to in-vitro or ex-vivo recapitulate the in-vivo properties of complex human tissues. In-vitro developed liver microtissue precursors (µTP), able to recapitulate fundamental properties of the liver tissue were used as a reliable testing platform to evaluate nano-bio-interactions at the tissue level. cHANPs penetration in µTP was preliminary assessed over time and compared to the

tissue penetration of two different nanoparticle systems, exosomes and hybrid lipid-polymer nanoparticles. Results revealed cHANPs as the fastest penetrating system, with the distribution of the particles over the whole thickness of the tissue completed in only 24h. In this regard, the possible involvement of CD44 receptors overexpressed by hepatocytes in the specific recognition of HA was hypothesized. Despite spherical shape, similar size and slightly negative surface charge, the same penetration behaviour could not be observed for the other two drug delivery systems which required at least 48h to start significantly penetrating the tissue. Additionally, exosomes appeared to specifically accumulate in particular domains of the tissue while both cHANPs and hybrid lipid-polymer particles were distributing in the whole cell cytosol. These preliminary observations allowed to demonstrate that the macroscopic size, shape, and charge characteristics that are usually taken into consideration for the prediction of particle diffusion in tissues represent a strongly reductive set of properties to reliably evaluate the transport properties of nanoparticles in such complex three-dimensional tissues. In a second separate study, cHANPs ability of preserving structural properties as well as improved imaging capabilities due to the Hydrodenticity property, were assessed in a complex ex-vivo human tissue, the atherosclerotic plaque (AP). The high heterogeneity characterizing both cells and tissue components made of lipidic domains, fibrotic, thrombotic and calcified regions, makes the AP a suitable platform to test the stability of cHANPs in complex biological environments. Ex-vivo MRI in a clinical 1.5T instrument revealed that upon injection in the tissue, both cHANPs and Ab36-cHANPs, nanoparticles specifically engineered to interact with the macrophages of the AP, preserved their property of Hydrodenticity guaranteeing a much higher contrast enhancement than the free contrast agent at the same concentration. This result demonstrated that cHANPs are able to preserve their structural properties also in complex and clinically relevant biological environments.

The acquired knowledge about different level nano-bio-interactions was applied to a case study pathology with the aim of providing a disease-inspired approach for the rational design of nanoparticles. Glioblastoma Multiforme (GBM), the most aggressive malignant brain tumour, was chosen as a case study pathology since the late diagnosis, the ineffective therapy and the inaccurate follow-up causing very poor patient prognosis, derive from the inability of the active agents in the gold standard for diagnosis and treatment in successfully overcome disease-specific biological barriers. With the purpose of addressing these limitations, theranostic cHANPs (Thera-cHANPs) co-encapsulating Gd-DTPA with improved MR imaging capabilities through the property of Hydrodenticity and Irinotecan (CPT-11) as a recently repurposed drug to overcome the tumour resistance proper of the poorly effective Temozolomide, were produced in microfluidics. To allow nanoparticle selective crossing of the healthy BBB which has been proven to characterize at least the 80% of the total tumour mass, the physiological routes of transport at the BBB were screened and LRP-1 mediated transcytosis through the synthetic peptide Angiopep-2 (TY-19) was found as the most promising for our 100 nm hydrophilic and negatively

charged Thera-cHANPs. Angiopep-2 has been shown to be successful in boosting both the BBB crossing of active agents up to 10-folds and the selective uptake by glioma cells, bearing a dual-targeting ability. Molecular docking simulations of LRP-1 with the peptide Angiopep-2 were performed to assess whether the chemical bonding of the peptide to nanoparticle surface might prejudicate its targeting ability. Being almost all the residues of Angiopep-2 involved in LRP-1 bonding, we concluded that chemical crosslinking of Angiopep-2 to Thera-cHANPs should have not negatively impacted receptor ligand interaction. Indeed, Angioepep-2 engineered Thera-cHANPs (Thera-ANG-cHANPs) demonstrated boosted cellular uptake both by the standard human glioma U87 cell line and patient derived stem-cells like glioma cells (GS-102). Additionally, the uptake mechanism of ANG-cHANPs by U87 cells was further investigated by depletion of energy-dependent uptake mechanisms and a competition assay in excess of free Angiopep-2 demonstrating both the direct involvement of Angiopep-2 in the uptake and the energy dependence of this mechanism, confirming the literature evidence of Angiopep-2 mediated internalization by a receptor mediated transcytosis. As a consequence of the improved and more efficient transport of theranostic nanoparticles inside the cells, Thera-ANG-cHANPs demonstrated an increased therapeutic capability with respect to the free drug causing the reduction of cell viability to 60% in only 24h of incubation. To investigate the role of superficial ligand density in the modulation of particle uptake by cells, the peptide Angiopep-2 was pre-conjugated to the backbone of HA prior to particle production in different molar ratios and a feasibility study of the microfluidic production of TY19-cHANPs was performed. After investigating nanoparticle morphology, mean size, surface exposed peptide and relaxometric properties, quantifying TY19-cHANPs uptake by U87 cells we demonstrated that the modulation of superficial amount of peptide can be used to successfully modulate the uptake of particles within the target cells. Indeed, TY19-cHANPs showed increased cellular uptake with respect to bare cHANPs but a reduced internalization with respect to ANG-cHANPs. In this regard, other variables could be investigated to further characterize the uptake mechanism of ANG-cHANPs. As an example, the dose of particles and their arrival at the cell membrane was demonstrated to affect the particle uptake kinetic. Very recently, Rees et al.[3], demonstrated how NP dose can affect the number of endosomes formed at a single cell level without however impacting the number of NPs per endosome. Additionally, the intracellular fate of the particles could be investigated, with specific reference to the involvement of both transcytosis and endocytosis mechanisms depending on the kind of cell investigated (e.g. healthy endothelia cell, glioma tumour cell). As a comparison, cHANPs surface was conjugated with the tripeptide Glutathione which has been proved to bear improved transport capacities at the BBB in several clinical trials. GLUT-cHANPs uptake by U87 cells as a model of human glioma was assessed and results demonstrated that despite the presence of the peptide, no significant improvement in particle uptake with respect to bare particles could be observed. This result revealed that biological barrier evaluation in particle rational design cannot be performed singularly, with each design choice drastically impacting the

overall effectiveness of the formulation. In conclusion, this comprehensive study revealed how, even facing a single pathology at a specific stage and selecting the active agents as well as materials to be used for particle design, a plethora of possibilities in the final composition of the vector is available, each one of them differently impacting on the final biological identity and thus on the in-vivo effectiveness of the formulation. Preliminary in-vivo data about cHANPs biodistribution in healthy mice and tumour accumulation in mice with an orthotopic model of human glioma were performed. Preliminary results allowed to assess a long circulation time of 8h and exclude off-target accumulation of bare cHANPs, confirming the stealth properties of the formulation. Additionally, retro-orbitally injected cHANPs skipping the BBB, showed a significant tumour accumulation. On the contrary, systemically injected cHANPs failed to sufficiently accumulate inside the tumour revealing the limitation of the enhanced permeability and retention (EPR) effect in brain tumours. Sindhwani et al.[4], recently questioned the effective role of EPR effect in guaranteeing preferential accumulation of nanoparticles at the tumour site in solid tumours. By analysing the vasculature of differently originated tumours (u87 gliomas, 4T1 breast cancers and PDX breast cancer), they showed the very low frequency of abnormal and enlarged interendothelial gaps occurrence, measured as less than 3 gaps/mm of vasculature. This allowed to demonstrate the high inefficiency of EPR effect in determining sufficient particle accumulation at the tumour site. Indeed, EPR effect has revealed successful for ultrasmall nanoparticles (diameters < 10nm) which might benefit for interendothelial and intermembrane transports which however is a mechanism far from being selective. Additionally, a diffusion-based transport can determine a sufficient accumulation as well as a simultaneously fast clearance from the tumour. For this reason, it is possible to conclude that formulations relying on EPR effect for specific tumour accumulations have a strongly reduced potential of being successful in clinics, especially in the case of brain tumours.

The last part of the thesis regarded the exploration of the role that pharmacokinetic modelling can have in the evaluation of nano-bio-interactions in clinical settings. Specific compartments as well as single molecular mechanisms are difficult to isolate and observe in human body. For this reason, exploiting the predictive potential of pharmacokinetic models can be enormously useful to understand the impact of different nanoparticle designs as well as the role of different administration doses and regimens on the therapeutic window of nanoparticles as a consequence of their biodistribution and toxicity. The MATLAB tool Simulink was used to implement a PK model describing the deposition of Temozolomide (TMZ) in high grade gliomas. TMZ was chosen for the wide availability of clinical data that allowed us to validate the model with reliable clinical data sets. The clinically validated PK model was then implemented to describe the role of the pegylated liposomal formulation ONYVIDE, FDA approved for the treatment of the adenocarcinoma of pancreas, in increasing the circulation time while reducing off target toxicity of the pro-drug irinotecan. A second model was used to describe the deposition of the contrast agent

Gadodiamide in different grade gliomas, revealing the tremendous impact that the stage of the disease has on the final accumulation of the active agent in the tumour mass. This result allowed us to highlight the unneglectable importance of the disease characterization prior to nanoparticle design. Finally, the role of Angiopep-2 in boosting the uptake of Paclitaxel across the BBB of healthy rats and in improving the tumour accumulation of the same agent in glioma bearing rats was assessed.

As an overall conclusion, in the era of precision medicine it appears clear that to considerably impact on clinical translation of nanomedicine, the scientific community should re-think the way it currently approaches nanomedicine rational design. In the last decades scientists put a strong effort in developing new technologies to confer specific properties and functionalities to nanocarriers, based on the macroscopic impact that these features might have on particle biodistribution, toxicity and metabolism. On the other side, however, there is a still emerging knowledge regarding the biology and the pathophysiology of many diseases and the related biological barriers which are currently increasing awareness about the relevance of nanoparticle biological identity and consequently generating questions about the most up to date rational choices for nanomedicine design.

Despite bearing a great potential to be a life changing technology for many diseases, too many grey areas still exist in the understanding of nanomedicines interaction with the human body and this thesis work presented an effort in this sense. It started with the investigation of the relevance of each single design choice, contributing to define nanoparticle synthetic identity, on single level nano-bio-interaction for the definition of hydrogel-based nanoparticle biological identity as a clinically relevant model of NPs. The acquired knowledge was applied to a case study pathology, Glioblastoma Multiforme (GBM), to propose a methodology for the rational design of a theranostic nanovector with boosted imaging and therapeutic capacities to address the most urgent needs related to the pathology. Indeed, the nanovector was designed to tackle and overcome disease-specific biological barriers moving from endothelial lining of the BBB to drug resistance in GBM. In the design process many questions about the underlying molecular mechanisms of specific nano-bio-interactions relevant for this pathology were answered and many others left open, with the final aim of showing how the integration of multiple tools moving from the bioinformatics, to transport phenomena, cell biology and pharmacokinetic modelling are impactful in producing increased understanding, opening new questions and thus generating increased awareness in the rational design of clinically relevant formulations.

VI.I. Reference

1 Vergnes, J. N. Safety and Efficacy of the BNT162b2 mRNA Covid-19 Vaccine. *New England Journal of Medicine* **384**, 1577-1577 (2021).

2 Francia, V. *et al.* Corona Composition Can Affect the Mechanisms Cells Use to Internalize Nanoparticles. *Acs Nano* **13**, 11107-11121, doi:10.1021/acsnano.9b03824 (2019).

3 Rees, P., Wills, J. W., Brown, M. R., Barnes, C. M. & Summers, H. D. The origin of heterogeneous nanoparticle uptake by cells. *Nature Communications* **10**, doi:10.1038/s41467-019-10112-4 (2019).

4 Sindhwani, S. *et al.* The entry of nanoparticles into solid tumours. *Nature Materials*, doi:10.1038/s41563-019-0566-2.

VII. List of publications

- *Radiolabeled PET/MRI Nanoparticles for Tumor Imaging* – Forte E, Fiorenza D, Torino E, Costagliola di Polidoro A, Cavaliere C, Netti PA, Salvatore M, Aiello M. Journal of Clinical Medicine 2019 Dec 9; 9(1):89. DOI:10.3390/jcm9010089.

- *A Microfluidic Platform to design Multimodal PEG - crosslinked Hyaluronic Acid Nanoparticles (PEG-cHANPs) for diagnostic applications* – Tammaro O*, Costagliola di Polidoro A*, Romano E, Netti PA, Torino E. Scientific Reports 2020 Apr 7; 10(1):6028. DOI: 10.1038/s41598-020-63234-x. *equally contributing authors

- *Theranostic Design of Angiopep-2 Conjugated Hyaluronic Acid Nanoparticles (Thera-ANG-cHANPs) for Dual Targeting and Boosted Imaging of Glioma Cells.* Costagliola di Polidoro A, Zambito G, Haeck J, Mezzanotte L, Lamfers M, Netti PA, Torino E. Cancers (Basel). 2021 Jan 28;13(3):503. doi: 10.3390/cancers13030503.

- *Targeting Nanostrategies for Imaging of Atherosclerosis.* Costagliola di Polidoro A, Grassia A, De Sarno F, Bevilacqua P, Mollo V, Romano E, Di Taranto MD, Fortunato G, Bracale UM, Tramontano L, Diomaiuti TC, Torino E. Contrast Media Mol Imaging. 2021 Mar 31; 2021:6664471. doi: 10.1155/2021/6664471.
- *Characterization of Angiopep—2/LRP1 ligand receptor energetic interaction via Molecular Docking* – Costagliola di Polidoro A, Cafarchio A, Vecchione D, Torino E - Under preparation

VIII. PhD schools and programs

PhD Schools

• "Nanomedicine: Science and applications" – University of Oxford, Department of Continuing Education (18/03/2019 – 22/03/2019)

Link: https://www.conted.ox.ac.uk/courses/nanomedicine-science-and-applications

Topic: A course to provide an exhaustive overview of the emerging discipline of nanomedicine. It focuses on the impact that nanotechnology has in the advance of medicine and healthcare including its role in delivery of therapy, tissue engineering and biosensing/diagnosis techniques, and discusses how to progress this area to meet future needs.

- "Digitalization tools for the chemical and process industries - GRICU" (11, 12 , 18, 19/03/2021)

  Link: https://indico.chem.polimi.it/event/27/

Topic: This virtual school is organized by GRICU to provide Ph.D. students in Chemical Engineering an introduction to methods and tools for digitalization, data analytics and advanced process control. The school is open also to M.Sc. students in Chemical Engineering and to young professionals.
Conventional lectures, assignments and specific case-studies will be available to participants. A final round-table with company professionals from different fields will conclude the school.

- "Biofabrication: an integrated bioengineering approach for the automated fabrication of biological structure for clinical and research applications" (13-16/09/2021)

  Link: https://www.grupponazionalebioingegneria.it/it/xl-scuola-annuale-di-bioingegneria-programma/

Topic: Biofabrication is the automated robotic layer-by-layer additive fabrication of 3D tissue and organ constructs, from tissue spheroids, or bioinks, including cell suspensions and cellularised hydrogels, following a digital model. The school provides a complete exploration of the potentialities of biofabrication technologies through the contribution of scientists with complementary expertise, including expert bioengineers in biomaterial design, rapid prototypying technologies, robotics, bioinformatics, computational modelling, bioimaging, nanotechnologies, biosensors, etc. The XL Annual GNB School aims at providing Ph.D students with interdisciplinary knowledge and hand-on-training from experts belonging to the Italian bioengineering community, as well as international scientists and industrial leaders.

PhD Programs:

• Awarded Grant to join Starship Innovation Program (03/2019 – 11/2019)

Link: https://www.starship.eithealth.eu/

Topic: An eight-month long program to involve students in industry-driven health innovation. The Stanford Biodesign methodology is applied in order to develop a need-pushed technology, working together with innovators in and outside the companies in highly skilled multidisciplinary teams.

IX. Staying at international research institute

Department of Radiology and Nuclear Medicine, Erasmus Medical Centre – Rotterdam, The Netherlands. (21/01/2020 – 13/03/2020)

Activity Plan: The scheduled period to be spent at the Erasmus Medical Centre of Rotterdam was of three months (21/01/2020-20/04/2020). However, because of the Sars-COV-2 pandemic I had to come back earlier in 13/03/2020.

The activity plan was defined on the basis of the expertise that Laura Mezzanotte research group has on the development of models of human tumors in mice, and on the presence of a dedicated facility for drug repurposing in Glioblastoma Multiforme, tested on primary cells directly extracted by patients. The plan included:

In-vitro testing of the developed NPs on patient derived cells and understanding on the interaction with and the internalization mechanisms by patient derived human Glioma cells;

In-vivo testing of nanoparticles in healthy mice, to study nanoparticle biodistribution, evaluate nanoparticle pharmacokinetics, validate nanoparticle stability in a relevant environment and evaluate the suitability of the tool for precision imaging in-vivo;

In-vivo testing of nanoparticles in tumor bearing mice, to study nanoparticle biodistribution in presence of the tumor, evaluate nanoparticle pharmacokinetics and assess the diagnostic and therapeutic potential of the formulations.

X. Communications to Congresses and Conferences

Participation to "Applied Nanotechnology and Nanoscience International Conference 2021" held online from 24.03.21 to 26.03.21 with an oral presentation about "*Theranostic Design of Angiopep-2 Conjugated Hyaluronic Acid Nanoparticles (Thera-ANG-cHANPs) for Dual Targeting and Boosted Imaging of Glioma Cells*".

XI. Other Activities

Appointment as expert of the subject in "diagnostic devices and drug delivery" (26/10/2020 – 31/10/2021)